博士論文

X-ray Study of Ground-Based Plasmas with TES Microcalorimeters

Tokyo Metropolitan University
Department of Physics
Keisuke Shinozaki
東京都立大学 理学研究科
宇宙物理実験研究室
篠崎 慶亮

Abstract

A superconductive transition edge sensor (TES) calorimeter is for the first time applied for the diagnostics of the reversed-field pinch plasma produced in the toroidal pinch experiment RX (TPE-RX), and the instrumental system are fully described. The first result from the soft X-ray spectroscopy in 0.2–3 keV with an energy resolution $\sim$ 50 eV are also presented. The TES calorimeter is made of a thin bilayer film of titanium and gold with a transition temperature of 151 mK and its best energy resolution at our laboratory is 6.4 eV, while it was significantly degraded by about a factor of eight during the plasma operation. The TES microcalorimeter was installed in a portable adiabatic demagnetization refrigerator (ADR), which is originally designed for a rocket experiment. The detector box is carefully designed to shield the strong magnetic field produced by the ADR and TPE-RX. The ADR was directly connected to TPE-RX with a vacuum duct in the sideway configuration, and cooled down to 125 mK stabilized with an accuracy of 10 μK r.m.s. using an improved proportional, integral, and derivative control (PID) method. Thin aluminized Toray Lumirror or Parylene-N films were used for the IR to UV blocking filters of the incident X-ray window to allow soft X-rays coming into the detector with good efficiency. TPE-RX was operated with the plasma current of $I_{\rm p} = 220$ kA, and the waveforms of the TES output for every plasma shot lasting $\sim$ 80 ms were obtained with a digital oscilloscope. The waveforms were analyzed with the optimal filtering method, and X-ray signals were extracted. A total of 3472 counts of X-ray signals were detected for 210 plasma shots during the flat-top phase of $t = 35$–70 ms. Combined with the data measured with a lithium drifted silicon detector in 1.3–8 keV range, spectral features are investigated using a spectral fitting package XSPEC. The obtained spectrum is well explained by thermal plasma emission, although an impurity iron-L line emissions at variously ionized states are dominant around 0.7–1.2 keV. At least three different temperature components ranging $T = 350$–900 eV are required to account for the spectral shape, while the average temperature is consistent with the ruby laser Thomson scattering measurement.

Contents

List of Figures

List of Tables

Chapter 1

Introduction

1.1 X-ray spectroscopy in astrophysics

Astrophysics is the branch of astronomy and physics concerned with the study of the origin and the evolution of celestial objects, with the assistance of physicl laws. In the 20th century, we have learned that our univerce is not steady at all, but that it originated from the so-called "Big Bang" about fifteen billion years ago, and continues to evolve to create the present complex hierarchical structures. However, many fundamental questions still remain: when and how were stars born, galaxies formed, and large structures like clusters of galaxies created? Where is the universe going from now on? High resolution X-ray imaging spectroscopy is one of the key technologies for answering these questions. In this introductory chapter, I briefly describe some astrophysical questions which could be answered by spatially-resolved X-ray spectroscopy, and then summarize the required performance of an X-ray spectrometer with imaging capability to achieve this.

1.1.1 Studying the evolving Universe with X-rays

Stars, like human beings, have life cycles. Protostars are created by gravitational collapse of the interstellar medium. THey grow into main sequence stars once nucleosynthesis begins inside. After exhausting their fuel, some of them release their outer layers into interstellar space and die quietly, while others result in supernova explosions where most of their bulk is blown off. Stellar material which contains heavy elements * is required into the interstellar medium (ISM), while compact objects such as black holes, neutron stars, and white dwarfs are sometimes left behind. A galaxy is a group of $10^6 - -10^{12}$ stars, where individual stars repeat their cycles independently. In the long term, however, there is an outflow of the galactic medium into intergalactic space, or a "galactic wind", which contains heavy elements produced inside the stars. A cluster of galaxies is a group of several hundreds to several thousands of galaxies. Clusters of galaxies are the largest bound systems in the universe, with a scale of several tens of million parsecs. The gravitational potential of a cluster of galaxies is formed by dark matter, which is not visible by electromagnetic waves, and each galaxy is trapped in this potetial. Moreover, the intracluster space is filled with a large amount of hot gas ($10^6 - -10^8$ K). This intracluster medium (ICM) also contains heavy elements, which means that there must be aa significant contribution from the galactic wind. Clusters of galaxies are not steady, either. They grow through gravitational install and merger of smaller clusters. In this way, the hierarchical structures in our universe evolve in close connection with one another.

*In this chapter, "heavy elements" or "metals" mean the elements heavier than helium.

Remarkable progress in observational technologies in recent years realized large ground-based telescopes with 8-10 m mirrors such as the Subaru Telescope, and space telescopes free from the effects of the Earth's atmosphere. In the radio band, space VLBI (very long baseline interferometry) is working using the HALCA satellite, which achieves extremely high angular resolution. Owing to these new technologies, we will obtain answers to questions about th evolution of the universe. The situation is the same in the X-ray band. Two new powerful X-ray observatories have been just put in orbit: Chandra by NASA in 1999 and XMM-Newton by ESA in 2000. Chandra accomplishes angular resolution better than "1", while XMM-Newton attains a very large effective area in the 0.1–10 keV band. In 2005, the fifth Japanese X-ray astronomy sattellite Suzaku, which is the the successor to the ASCA satellite and a resurgent mission of ASTRO-E, is launched.

X-ray emission is produced by synchrotron radiation and inverse-Compton scattering by relativistic electrons, thermal bremsstrahlung and blackbody radiation from hot matter. Thus, this is the best electromagnetic wave band for exploring high energy phenomena in the universe. In addition there exist K lines and K absorption edges of abundant heavy elements such as Carbon, Nitrogen, Oxygen, Neon, Magnesium, Silicon, Sulfur, Argon, Calcium, and Iron, in the 0.1–10 keV band. This means that X-ray spectroscopy is an ideal tool for detecting and examing the abundances and physical conditions of hot plasma and warm gas. The energy shift and the line width of these emission lines also offer information on dynamical motions of the hot gas. These features make high resolution X-ray spectroscopy a key to revealing the evolving universe. In particular, spatially-resolved spectroscopy is principal for catching the moment of evoltion. In the following sections, I give three examples to show how X-ray imaging spectroscopy works.

Recycling of matter

Elements heavier than hydrogen and helium are nucleosynthesized in stars, and are distributed by supernova explosions, stellar winds, etc.. The ejecta of supernovae or stellar winds collide with the interstellar matter (ISM), and are shock-heated up to $10^6 - 10^7$ K. Thus, supernova remnants are bright X-ray emitters, and with spatially-resolved X-ray spectroscopic observations, we can look at the scene of diffusion of the heavy elements produced inside stars into interstellar space. Spatially-resolved X-ray spectroscopic observations are now beginning to display how ejecta expand, and how the metals produced in stars are distributed into interstellar space. In future missions, more advanced imaging spectrometers are needed to determine the metal abundances and to measure the velocity of each knot of ejecta. These will also provide feedback to theoretical models of stellar evolution and nucleosynthesis.

Mass outflow from galaxies

A part of the ISM flows out of galaxies into intergalaxctic space. This outflow is especially prominent in starburst galaxies, where explosive starformation occurs. In these galaxies, kinetic energy from many type-II supernova and/or stellar winds is partially converted into galactic wind. In fact, bipolar outflows with a scale of 10 kpc are often observed in edge-on local starburst galaxies. This superwind is a very important phenomenon for understanding the chemical evolution od the universe, because it transports a large volume of mass which contains metals produced by stars, and enormous energy into the intergalactic medium (IGM) or ICM. Thus, it is very important to quantify the total mass, metal abundances, and energy of the matter transported by galactic winds. However, een the basic physical properties of local superwinds are uncertain, and spatially-resolved high resolution X-ray spectroscopic obsrvations are strongly desired.

Evolution of clusters of galaxies

Clusters of galaxies are the largest bound systems in the present universe. It is thought that they ae evolving through collision and merger. Observations so far indicate no changes in temperature, metal abundances, and X-ray luminosities in z <1.0. (e.g., Matsumoto et al. 2000), while one exotic cluster was found at $z = 1.0$ (Hattorri et al. 1997). Thus, observations of farther clusters ($z > 1.0$) to compare the physical parameters with loal ones are essencial for revealing their evolution.

Another important method for studying cluster formation and evolution is to observe how the clusters of galaxies collide and merge in detail. Spatially-resolved X-ray spectroscopy of the hot plasma in merging clusters is the direct way to achieve this, because the Doppler shift and broadening of the emission lines offer information on the global motion of the hot plasma. Fro example, the relative velocities of the colliding and merging clusters are estimated to 300-2000 km/s. For the He-like Fe Kα line at 6.7 keV, a 300 km/s velocity corresponds to an energy shift 6.7 eV. This number is well within the target of the X-ray spectrometers of the next generation.

During a merger, a significant fraction of the enormous ($10^{63} - 10^{64}$ erg) kinetic energy of the colliding subclusters dissipates through shock heating. This process is also important as a location of the acceleration of cosmic rays and as an energy source for the "missing warm baryons" which are expected to exist in large quantities in the local IGM. Chandra observations detected sharp shock-like surfacce brightness edges in the on-going merger Abell 2142 (markevitch et al. 2000) and Abell 3667 (Vikhlinin et al.2000). Across these edges, there exist gas density discontinuities of a factor of two to four, and temperature gaps of a factor of two. However, the pressure is continuous across the edges, and the denser side of the edge has a lower temperature. These facts indicate that these edges are not shock fronts, and the authors here suggested that they delicate the dense subcluster cores that have survived a merger and ram pressure stripping by the surronding shock-heated gas. More detailed spatially-resolved spetroscopic observations will reveal the motions of the gas on both sides of the edges, as well as more accurate temperature and pressure profiles, to help our understanding of the physical processes of cluster evolution.

1.2 Development of Transition Edge Sensor — TES type Microcalorimeter

Recently, a transition edge sensor (hereafter TES) was proposed as an extremely sensitive thermometer for X-ray microcalorimeters [12]. The TES calorimeter is a detector which measures energy of an incident X-ray photon as a temperature rise using the sharp transition edge of superconductors. TES calorimeters bring us a significant improvement in the response time due to a strong electro-thermal feedback [13]. To realize its maximum performance, the detector must be cooled below $\sim$ 100 mK in order to suppress phonon noise and to reduce the heat capacity of the detector. The energy resolution of 2.4 eV for Mn-K$_\alpha$ (5.9 keV) has been achieved in the world [34]. We are now developing a TES calorimeter array for future Japanese X-ray astronomy missions [15, 22, 24]. To date, an energy resolution of $\sim$ 6 eV in the energy range of $\lesssim$ 10 keV has been achieved with a single pixel device in our laboratory [14, 32]. We have also developed a portable adiabatic demagnetization refrigerator (hereafter ADR) system for ground experiments, which is based on the system originally designed for a rocket experiment [20]. Temperature stability of $\lesssim$ 10 μK and a holding time of $\sim$ 24 h at 125 mK are demonstrated so far [28, 10, 11].

As the background of the detector development, high resolution X-ray spectroscopy with a non-dispersive instrument is strongly desired in the X-ray astronomy field because wavelength-dispersive instruments with Bragg crystals or gratings have generally low throughputs and are not usable with extended celestial objects, such as supernova remnants, clusters of galaxies, etc. The single-photon microcalorimeter is one of the best candidates which realizes a spectral resolution comparable to dispersive instruments. The first results are reported for the rocket experiment [20], and the XRS instrument [16] onboard Japanese X-ray astronomy satellite, *Suzaku*, had realized $E/\Delta E \sim 1000$ at 6 keV in space, although the XRS could not observe any celestial objects due to a malfunction of a refrigerator. The primary goal of our future mission, *DIOS* (Diffuse Intergalactic Oxygen Surveyor [15]) is to measure redshifts and intensities of $\mathrm{O_{VII}}$ (561–665 eV) and $\mathrm{O_{VIII}}$ (653 eV) emission lines from warm-hot intergalactic medium (WHIM) in the temperature range of 10^{5-7} K. Numerical simulations [6, 8], suggest that 30–50% of total baryons at the present universe (redshift $z \lesssim 0.3$) take the form of the WHIM, and measuring those lines enables us to map the mass distribution of the neighboring universe. Our theoretical studies [39, 38] have proven that a microcalorimeter array with energy resolution better than FWHM = 5 eV can resolve oxygen lines with different redshifts. We are developing such an instrument, and need a test bench on ground to measure X-ray emission from thermal plasma with similar temperature.

1.3 X-ray spectroscopy of thermonuclear fusion plasma

This thesis presents the first result of a new collaboration between the research fields of space astrophysics and fusion plasmas. X-ray spectra from a deuterium plasma including emission lines produced by impurities in a large reverse field pinch (RFP) device, the toroidal pinch experiment, TPE-RX [36, 35], are investigated with a TES calorimeter for the first time. TPE-RX is one of the three largest RFP machines in the world with a major radius $R = 1.72$ m and a minor radius $a = 0.45$ m. The primary purpose of the present experiment is to resolve characteristic X-ray lines of impurities (e.g., O, Cr, Fe, Mo) in the 0.2–8 keV band, based on the high resolution spectra. Such diagnostics is important to determine key plasma parameters for a controlled fusion, such as electron density, temperature and impurity contents. The typical plasma temperature of TPE-RX is ~ 600 eV, which is similar to that of the WHIM. They are merits of the ground experiment that parameters are tunable and that there are established methods of probing the plasma condition. On the other hand, the magnetic environment and the mechanical vibration is much severer at the vicinity of the fusion plasma device than those in space, which can be towards establishing the stable operation of the detector system including the refrigerator. Such diagnostics is also important to determine key plasma parameters for a controlled fusion, such as electron density, temperature and impurity contents.

Such a measurement is only possible by a detector which simultaneously offers a good energy resolution ($\lesssim 10$ eV) and a wide energy band (0.2–8 keV). There are some Ultraviolet or soft X-ray measurements of Si(Li) spectrometer or wavelength dispersive devices, e.g. grating spectrometer, which provide radiated power loss, electron temperature and the time behavior of the emission line of impurities in the RFP plasma [5, 3]. Ogawa [26] obtained the soft-X-ray spectrum which includes high-energy tail and some impurity lines with a Si(Li) detector. Carraro [4] measured the ultra soft X-ray spectrum of RFP plasma by an XUV extreme grazing incidence spectrometer to assess the level of impurity content. In this case, the obtained spectrum absolutely includes a lot of emission lines of impurities, so that it is also useful to measure the soft X-ray emission with good energy resolution in wide energy band to investigate the behavior of low–high ionized emission lines, and to discover a line free spectral region and high energy tail for an analysis of electron temperature or e.g. no-thermal bremsstrahlung. Therefore TES calorimeters are expected to be a very effective tool.

1.4 Aim of the present thesis

This paper describes as follows. In Sec. 2, we explain principles of TES calorimeters, the detector used in this measurements, and TPE-RX. In particular, the construction of the refirgerator used in this measurement are presented. In Sec. 3, we explain the experimental setup, controlled plasma parameter, and the actual condition of the TES calorimeters as well as the operating cycles. In Sec. 4, we constructed the signal extraction method from the detected waveforms after optimal filtering. We also shows the analysis of detected waveforms in various conditions, which implies the main cause of the degradation of the detector performances in this chapter. In Sec. 5, results of the spectral fitting analysis for obtained spectra including that of SiLi detector in hard energy band are presented. The overall results are discussed in Sec. 6. The conclusion is in Sec. 7. A brief report on the result has been given in the proceedings of the 14th International Toki Conference (ITC-14) [27], and the 11th international workshop on Low Temperature Detectors (LTD-11) [29]. Further details of the spectral analysis, including the March 2005 data, and the result of fusion plasma diagnostics have been reported in (Shinozaki et al. 2006).

Chapter 2

Instrument Description

The devices of the measurement are mainly separated to 3 components, detector, refrigerator, and the plasma experiment. Our main purpose is to measure the X-ray signal from TPE-RX during a plasma generation by using the new spectrometer, TES calorimeter which is operated by the portable refrigerator, the ADR system.

In this chapter, I introduce main devices in the measurement, TES calorimeter (Sec. 2.1), the ADR system (Sec. 2.2) and TPE-RX (Sec. 2.5), with other technical details — temperature control of the detector box (Sec. 2.3) and X-ray window (Sec. 2.4).

2.1 TES calorimeter

The TES calorimeter is being developed in our group to have a high resolution spectroscopy in X-ray astrophysics. In this section, the basic principle, structure, and actual performance of the detector in our labo which used in the plasma experiment are briefly described. Though we used only single pixel TES calorimeter, we have to actualize a multi-pixel calorimeter device as well as a useful refrigerator which provide a best performance for the calorimeter in a future, when effective area, availability, and an importance of thermal bath for the device are considered.

2.1.1 The basic principle

An X-ray calorimeter is a thermal detector which measures the energy of an incident X-ray photon as a temperature rise. A very high spectral energy resolution can be achieved by operating the detector at very low temperature 0.1K. An important thing is that grating spectrometers, which also have more than 1000 spectral resolution power in X-ray energy band, are not suitable for extended sources, and calorimeters can be made for a larger effective area than gratings.

As shown in Figure 2.1, an X-ray calorimeter consists of an absorber for high detective efficiency of X-ray, a thermal link, and heat sink(heat bath). An incident X-ray photon is photo-absorbed by the absorber. Its energy is converted into heat, and slightly warms up the calorimeter pixel. This temperature rise is given by

$$\Delta T = \frac{E}{C} \tag{2.1}$$

where E is the incident energy and C is the heat capacity of the calorimeter pixel. Using a thermistor, this temperature rise is sensed as a resistance change. The calorimeter pixel has a weak coupling with a heat sink, so that temperature slowly goes back to the initial operating point. This is expressed as

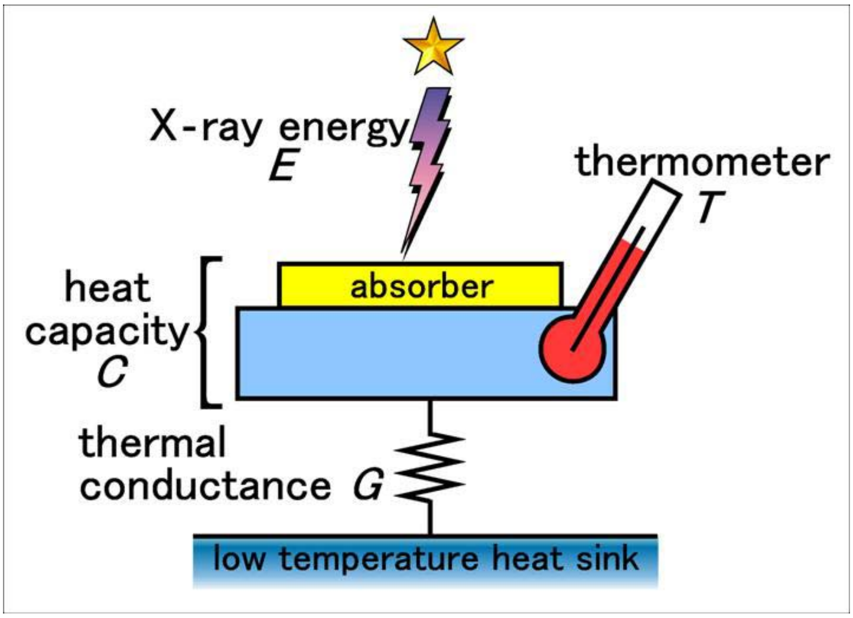

Figure 2.1: Schematic view of an X-ray microcalorimeter. The calorimeter consists of an absorber and a thermometer which have a heat capacity C, and are connected to a heat sink with a thermal conductance G of the thermal link.

$$C\frac{d\Delta T}{dt} = -G\Delta T \tag{2.2}$$

where G is the thermal conductance of the thermal link. Thus, the temparature rise decays exponentially, with a time constant is

$$\tau = \frac{C}{G} \tag{2.3}$$

The energy resolution is limited by thermodynamic fluctuation in the detector. The number of phonons in the calorimeter pixel is $N \sim CT/k_{\mathrm{B}}T = C/k_{\mathrm{B}}$. Thus, the thermodynamic fluctuation is given by

$$\Delta E \sim \sqrt{N}k_{\mathrm{B}}T = \sqrt{k_{\mathrm{B}}T^2C} \tag{2.4}$$

Fundamental energy resolution limit can be written as

$$\Delta E_{\mathrm{FWHM}} \sim 2.35\,\xi\sqrt{k_{\mathrm{B}}T^2C} \tag{2.5}$$

where ξ is a parameter which depends on the thermometer sensitivity and the operating condition. Considering the temperature dependence of C, the energy resolution strongly depends on the temperature, and by operating at extremely low temperature (≤ 0.1 K), very high energy resolution can be achieved.

Using a thermistor, the temperature rise is sensed as a dynamical change of a resistance. The thermometer sensitivity α is define by

$$\alpha \equiv \frac{d\ln R}{d\ln T} = \frac{T}{R}\frac{dR}{dT} \tag{2.6}$$

where the T is temperature, and R is the resistance at the operating point of the thermometer.

One approach to improve the energy resolution of the X-ray calorimeter is to increase the thermometer sensitivity α. Conventional semiconductor thermometers, like the one used in XRS of ASTRO-E, achieves $|\alpha| \leq 6$. To have a higher sensitivity, using the sharp transition between normal and superconducting state as a thermometer is available. In this thesis, we adopted a superconducting device as a calorimeter.

2.1.2 Transition edge sensor and superconducting calorimeter

A Transition Edge Sensor — TES is a thermometer which uses the sharp transition between normal and superconducting state to sense the temperature. This transition occurs typically within a few mK, and the sensitivity parameter α defined by Eq. 2.6 can be as large as 1000. Thus, superconducting calorimeters potentially can improve the intrinsic energy resolution by more than a order of magnitude, comparing with a conventional semiconductive calorimeter. This means that the superconducting calorimeters have more margin for selecting absorbers.

In superconducting calorimeters, the operating temperature is fixed by the transition temperature of the TES. This sounds like a limitation for operating superconducting calorimeters. However, by using a bilayer thin-film, the transition temperature can be adjusted to the appropriate temperature. In a bilayer thin-film, Cooper pairs permeate the normal conductor, and the transition temperature is lowered, depending on the thickness ratio (proximity effect). Thus, by changing the thickness ratio, the transition temperature can be controlled. We use the thin bilayer film of titanium and gold.

Despite of its sensitivity, current-biased superconducting calorimeters have not widely used so far, because TESs suffer from limitations due to film non-uniformly, transition nonlinearity, and dynamical range. Recently, a particle detector based on a voltage-biased superconducting film that maintains itself in the transition region through the use of strong negative electrothermal feedback (ETF) has been described ([12, 13, 18]). This feedback produces a self-biasing effect that causes the temperature of the film to remain within its transition region. It also reduces the thermal time constant of the sensor.

2.1.3 Electrothermal feedback (ETF)

By operating a TES in a constant voltage-bias circuit, strong negative feedback can be achieved. If there is a heat input and the the temperature rises, the resistance of TES increases rapidly. Due to the constant voltage bias, the current decreases, and the Joule power also decreases. Therefore, in a constant voltage bias, negative feedback which holds the power (or temperature) constant works. In practice, it can be achieved using a shunt resistor in parallel, whose resistance is much smaller than the operating resistance of the TES, as shown in Fig. 2.2.

In the steady state at the operating temperature T_0, the Joule power $P_{\mathrm{b}} \equiv V_{\mathrm{b}}^2/R_0$ balances the heat flow from the calorimeter pixel to the heat sink,

$$P_{\mathrm{b}} = \frac{G_0}{n}(T_0^n - T_s^n) \tag{2.7}$$

where V_{b} is the bias voltage, G_0 is a constant which satisfy $G = G_0 T^{n-1}$, R_0 is thee resistance of the TES at the operating point, and T_{s} is the temperature of the heat sink. For a small temperature change $\Delta T \equiv T - T_0$,

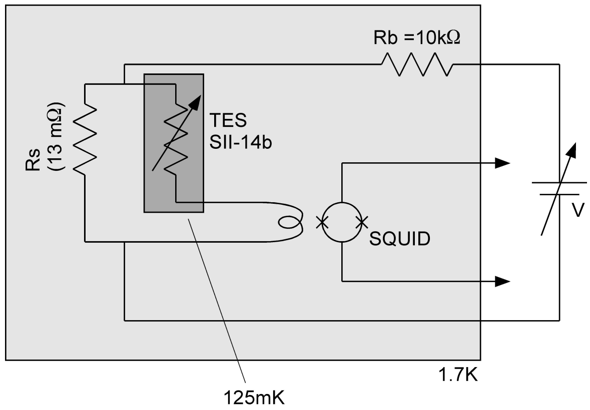

Figure 2.2: Electric circuitry around the TES calorimeter. TES calorimeter is operated at 125 mK, and 420-series SQUID array (SSA) is kept at 1.7 K.

$$C\frac{dT}{dt} \sim \frac{V_{\mathrm{b}}^2}{R(T_0)} - K(T^n - T_{\mathrm{s}}^n) \tag{2.8}$$

In the first order approximation, Eq. 2.8 becomes

$$C\frac{dT}{dt} = -\frac{V_{\mathrm{b}}^2}{R(T)^2}\Delta R - nKT^{n-1}\delta T = \frac{P_{\mathrm{b}}\alpha}{T}\Delta T - G\Delta T \tag{2.9}$$

its solution is

$$\Delta T = \Delta T_0 \exp\left(-\frac{t}{\tau_{\mathrm{eff}}}\right), \qquad \tau_{\mathrm{eff}} \equiv \frac{C/G}{1+\frac{P_{\mathrm{b}}\alpha}{GT}} \tag{2.10}$$

in this case, τ_{eff} is called the effective time constant. If the temperature of the heat sink is much lower than the operating temperature ($T_{\mathrm{s}}^n \ll T^n$),

$$\tau_{\mathrm{eff}} = \frac{\tau_0}{1+\frac{\alpha}{n}} \sim \frac{n}{\alpha}\tau_0 \tag{2.11}$$

In the second equation $\alpha/n \gg 1$ is asssumed. Thus, by strong negative ETF, the response time of the detector is significantly shortened. This is one of the great advantages of the voltage-biased superconducting calorimeter. The signal can be sensed as a current change

$$\Delta I = \frac{V_{\mathrm{b}}}{R(T_0+\Delta T)} - \frac{V_{\mathrm{b}}}{R(T_0)} \sim -\frac{\Delta R}{R}I \sim \alpha\frac{E}{CT}I \tag{2.12}$$

2.1.4 Optimal filter and energy resolution limit

X-ray microcalorimeter have very small fundamental energy fluctuation and potentially can achieve good energy resolution. However, an actual pulse shape is affected by the noise, and a simple pulse peak is not a good estimate of the pulse height. Instead, by applying an optical filter described below, errrors can be minimized [31].

Assume that $D(t)$ is a measured pulse, and that the pulse spectrum $D(f)$ can be written in the frequency domain as

$$D(f) = A \times M(f) + N(f) \tag{2.13}$$

where $M(f)$ and $N(f)$ are the model pulse spectrum and noise spectrum, respectively, and A is the amplitude. The best estimate of the pulse amplitude A is the one which minimizes the difference between an actual pulse and an estimated pulse in least square sense. If we define the difference as

$$\chi^2 \equiv \int \frac{|D(f) - A \times M(f)|^2}{|N(f)|^2} \tag{2.14}$$

the best estimate of A is obtained by minimizing χ^2

$$A = \frac{\int_{-\infty}^{\infty} \frac{DM^* + D^*M}{2|N|^2} df}{\int_{-\infty}^{\infty} \frac{|M|^2}{|N|^2} df} \tag{2.15}$$

$D(f)$ and $M(f)$ are the Fourier transforms of real functions, so that they satisfy $D(-f) = D(f)^*$ and $M(-f) = M(f)^*$. Therefore,

$$\int_{-\infty}^{\infty} \frac{D(f)M(f)^*}{2|N|^2} df = -\int_{\infty}^{-\infty} \frac{D(-f)M(-f)^*}{2|N|^2} df = -\int_{-\infty}^{\infty} \frac{M(f)D(f)^*}{2|N|^2} df = \tag{2.16}$$

and the estimate od A becomes

$$A = \frac{\int_{-\infty}^{\infty} \frac{DM^*}{|N|^2} df}{-\int_{-\infty}^{\infty} \frac{|M|^2}{|N|^2} df} = \frac{\int_{-\infty}^{\infty} \frac{D}{M} |\frac{M}{N}|^2 df}{\int_{-\infty}^{\infty} |\frac{M}{N}|^2 df} \tag{2.17}$$

This says that A is an expectation $D(f)/M(f)$, calculated for each frequency and weighted with the square of the signal to noise ratio at that frequency $|M(f)/N(f)|^2$. Eq. 2.15 can be written as,

$$A = \frac{\int_{-\infty}^{\infty} D(t)\mathcal{F}^{-1} \frac{M(f)}{|N(f)|^2} dt}{\int_{-\infty}^{\infty} \frac{|M|^2}{|N|^2} df} \tag{2.18}$$

where $\mathcal{F}$ represents the inverse Fourier transform, and

$$T(t) \equiv \mathcal{F}^{-1} \left(\frac{M(f)}{|N(f)|^2} \right) \tag{2.19}$$

is the optimal filter template. Thus, the optimal pulse amplitude can be calculated as

$$H = N \Sigma D_i(t) T_i(t) \tag{2.20}$$

where N is a normarization, and $D_i(t), T_i(t)$ are the digitized pulse data and the template, respectively. In practice, $M(f)$ can be obtained by averaging pulses for monochromatic X-rays.

The fundamental energy resolution limit attainable by the optimal filter can be shown

$$\Delta E_{\mathrm{rms}} = \left(\int_0^\infty \frac{4df}{\mathrm{NEP}^2(f)} \right)^{-\frac{1}{2}} \tag{2.21}$$

where NEP(f) is the noise equivalent power [25] and can be written as

$$\mathrm{NEP}(f)^2 = 4k_{\mathrm{B}}TP_{\mathrm{b}} \left(\frac{1+(2\pi f)^2\tau^2}{\mathcal{L}^2} + \frac{\alpha\Gamma}{\mathcal{L}} \right) \tag{2.22}$$

where $\mathcal{L}$ is a loop gain, and $\Gamma = \left(\int_{T_{\mathrm{s}}}^{T} \left(\frac{tk(t)}{Tk(T)} \right)^2 dt / \int_{T_{\mathrm{s}}}^{T} \left(\frac{k(t)}{k(T)} \right) dt \right)$. Substituting Eq. 2.22 into Eq. 2.21, the fundamental energy resolution limit is

$$\Delta E_{\mathrm{rms}} = \left(\int_0^\infty \frac{4df}{4k_{\mathrm{B}}TP_{\mathrm{b}}\{\frac{1+(2\pi f)^2\tau_0^2}{\mathcal{L}_0^2} + \alpha\Gamma/\mathcal{L}_0\}} \right)^{-\frac{1}{2}} \tag{2.23}$$

$$= \sqrt{4k_{\mathrm{B}}TP_{\mathrm{b}}\tau_0\sqrt{1+\alpha\Gamma\mathcal{L}_0}/\mathcal{L}_0^2}$$

$$= \sqrt{4k_{\mathrm{B}}T^2C\sqrt{1+\alpha\Gamma\mathcal{L}_0}/(\alpha\mathcal{L}_0^2)}$$

Introducing the ξ parameter, which is defined as

$$\xi \equiv \sqrt{\frac{1}{\alpha\mathcal{L}_0\sqrt{1+\alpha\mathcal{L}_0\Gamma}}} \tag{2.24}$$

the intrinsic energy resolution (FWHM) becomes

$$\Delta E_{\mathrm{FWHM}} = 2,35\xi\sqrt{k_{\mathrm{B}}T^2C} \tag{2.25}$$

If $T_{\mathrm{s}} \ll T$, the $\Gamma \sim 1/2$, $P_{\mathrm{b}} \sim GT/n$, $\mathcal{L}_0 \sim \alpha/n$, and $\xi \sim\leq 2\sqrt{\sqrt{n/2}/\alpha}$. Thus, for large α, the intrinsic energy resolution is improved in inverse proportion to $\sqrt{\alpha}$. For example, ξ can be lower than 0.1 for $\alpha \sim 1000$.

2.1.5 General response of the TES calorimeter

According to a general feedback theory, the electrothermal feedback described above can be recognized as a closed loop. Besides, the TES calorimeter is actually operated by a pseudo-constant voltage bias with an electric circuit shown in Fig. 2.2.

For estimating the energy resolution limit, we first have to evaluate the noise. There are many sources of noise: radiation, temperature fluctuation of the heat sink — detector box, background magnetic field, $1/f$ noise, rf noise, etc .. In these noise sources, Johnson noise and phonon noise are the most fundamental, in a sense that we cannot avoid them so long as to use superconducting microcalorimeters, and limit the energy resolution in princple. A readout noise, the noise of a preamplifier also plays an important role.

In addition, the large hysteresis of a magnetic field is generated around the refrigerator and it pulls out the induction current in the electric lines of the detector during a plasma generation of TPE-RX. A mechanical vibration also runs through the port section to the refrigerator. It is important to analyze, reduce these noise effect to the TES calorimeter response, and optimize the signal reduction as well as to command the portable ADR system not in the best condition.

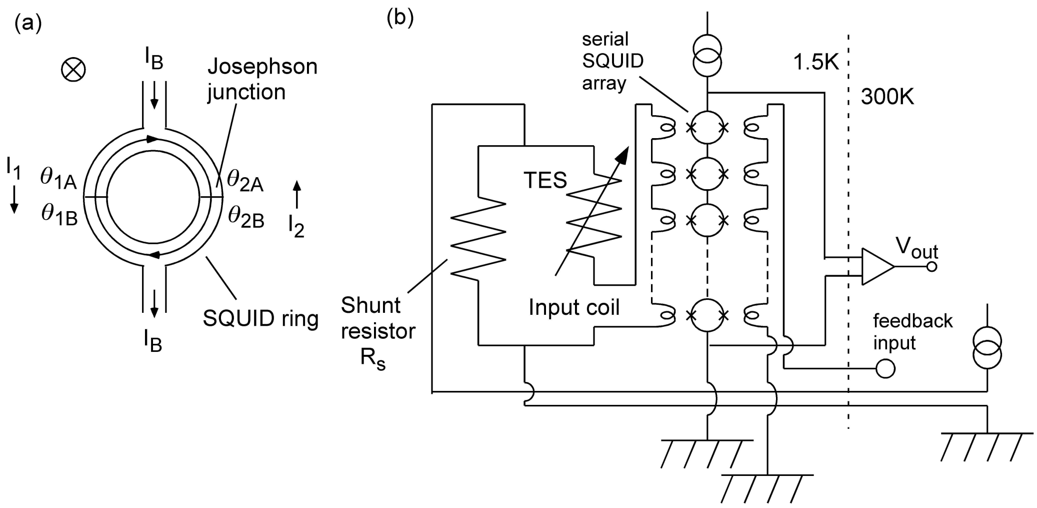

Figure 2.3: Schematic view of a Josephson junctions and the calorimeter readout with a SQUID ammeter.

2.1.6 Readout device — SQUID

For sensing a current change at the TES, a low impedance ammeter is required, and a SQUID ammeter is the best solution. A SQUID (superconducting quantum interference device) is a sensor making use of the Josephson effect of a superconducting Josephson junctions ring. SQUID can be installed near the TES calormeter at low temperature ($\leq$ 4.2 K), which means that it's very useful to use the device for read out of the signal of the TES without an extra heat load and noise. Fig. 2.3(a) shows a shematic view of a SQUID. There are two Josephson junctions in a SQUID ring, and the phase shifts at thesee junctions are not independent, but their difference is determined by the magnetic flux penetrating the SQUID ring,

$$\theta_2 - \theta_1 = 2\pi\frac{\Phi}{\Phi_0}, \qquad \Phi_0 = h/2e \equiv 2.06 \times 10^{-15}\ \mathrm{Wb} \tag{2.26}$$

where θ_1, θ_2 are the phase shifts at each end of the Josephson junctions, Φ is the magnetic flux penetrating the SQUID, and Φ_0 is the flux quantum. When the Josephson junctions are in the superconducting state, the bias current I_{B} can be written as,

$$I_{\mathrm{B}} = I_0 \cos\left(\pi\frac{\Phi_{\mathrm{exp}}}{\Phi_0}\right) sin\left(\theta_1 - \pi\frac{\Phi_{\mathrm{exp}}}{\Phi_0}\right) \tag{2.27}$$

where I_0 is the critical current for each Josephson junction, $\Phi_{\mathrm{exp}} \equiv \Phi - LJ$, is the external magnetic flux, L and J are the self-inductance of the loop and the loop current, respectively. Therefore, the phase shift changes in accordance with the external magnetic flux, for a given bias current.

By coupling a coil to the SQUID ring, it can be used as a low impedance ammeter with high sensitivity. Fig. 2.3(b) shows a schematic view of the calorimeter readout with a SQUID ammeter.

The SQUID noise consists of the Johnson noise coming from a SQUID shunt resistor, and the shot noise of tunnel junction. The spectrum is almost white below the cut-off frequency of the SQUID readout circuit, and the noise equivalent current is typically a few pA/$\sqrt{\mathrm{Hz}}$.

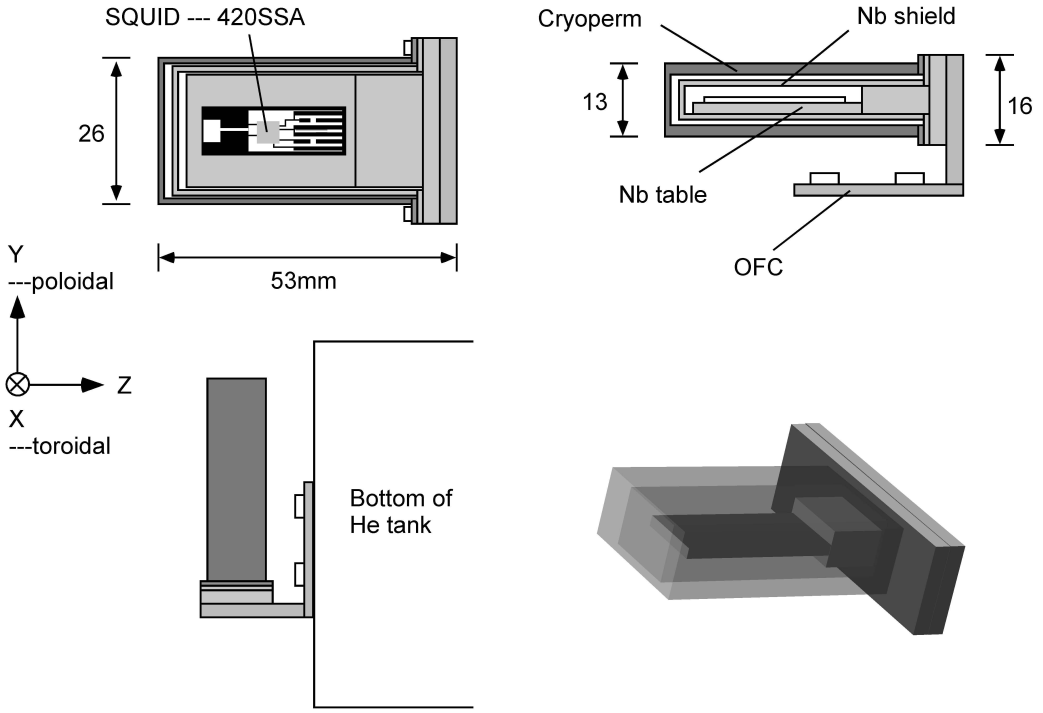

Figure 2.4: The design of the magnetic shield for the SQUID.

We used a commercial 420-series SQUID array (SSA) fabricated by SIINT, to carry out the signal readout of the TES calorimeter. The self-inductance of the SSA input-coil is 190 nH, and the readout noise is about 25 pA $\mathrm{Hz}^{-1/2}$ in our laboratory at TMU. 420-SSA is a SQUID amplifer, which is a series dc-SQUID array plus a series input-coil array. The array consists of 420 SQUIDs. By operating these SQUIDs in phase, the output voltage is amplified. An advantage of a SQUID amplifier is that signals are amplified at the cryogenic temperature, and the readout noise can be suppressed. Also, the impedance of a SQUID amplifier is larger than a single SQUID by a factor of several tens to several hundreds. Thus, it is easier to match the following circuit. Besides, wider bandwidth ($\sim$ MHz) is realized, comparing with a standard readout method using a lock-in amplifier.

Because SQUID uses a superconductor material, it's affected by earth magnetism. Especially, 420-SSA has 420 arrays of SQUID, so that output of each bias current I_{B} has different phase if a different magnitude of magnetic field to be trapped for each array is provided (see Eq. 2.27). As a result, the gain of the SSA become to be smaller and larger noise would be occured. We have to introduce a shield around the SSA to prevent the response degradation of the SSA. Fig. 2.4 shows the magnetic shield around the 420-SSA. It consists of Nb (superconductor, $T_{\mathrm{c}} = 9.2$ K, $B_{\mathrm{c}} = 1980$ Gauss) as an inner, and cryoperm as an outer shield. The measured magnetic field around the SQUID shield is described in Sec. 2.2.2.

2.1.7 Detective performance of the TES —SII14b

The device used in the measurement is a bridge-type TES calorimeter fabricated on a silicon wafer at SIINT. In first measurement, SII14b detector was used, which had the best energy rsolution in the measurement of our labo. The TES thermometer is made of a thin bilayer film of titanium (40 nm thick) and gold (110 nm) with a size 0.5 mm$\times$0.5 mm, suspended by a silicon-nitride bridge (1 μm thick and 700 μm wide) as a weak thermal link to the silicon substrate. An X-ray absorber made of gold (0.3 mm$\times$0.3 mm wide, 300 nm thick) is deposited on the TES calorimeter, and a sapphire collimator with 0.2 mm$\,\phi$ /

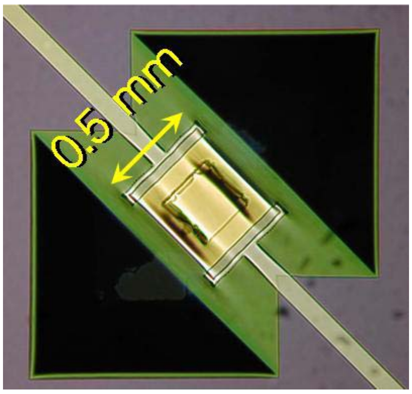

Figure 2.5: Photograph of SII14b, before the sapphire collimator being attached to the detector.

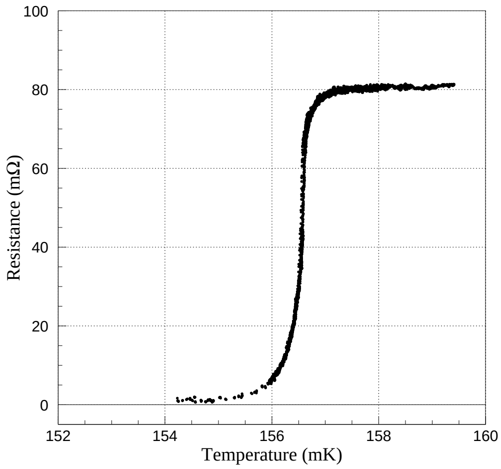

Figure 2.6: Relation between resistance and temperature of the TES, which was obtained by changing the temperature of the detector box, and constant current 1 μA.

300 μm thick is attached in front of the absorber. The expected quantum efficiency of the TES calorimeter itself is indicated by the dot-dashed line in Fig. 2.22. The transition temperature of the TES is $T_c = 156$ mK and the normal-state resistance is $R_n = 80$ mΩ, as shown in Fig. 2.6. Detailed design, fabrication and analysis of its best performance are described in [14, 32, 23].

The current responsivity of the TES I_{sq} is (as shown in Fig. 2.2),

$$I_{sq} = \frac{R_s}{R_{TES} + R_s + R_p} I_b \tag{2.28}$$

where R_{TES}, R_s is the TES and shunt resistance respectively, and I_b is the bias current of the power supply in room temperature. R_p is the parasitic resistance, which is usually caused by a deterioration of electric contacts of superconducting NbTi wiring. Fig. 2.7(a) shows the relation between the current through the TES I_{sq} and the TES voltage V_{tes} measured by using the dilution refrigerator in our labo.

The operating point dependence of the pulse height PH of the 5.9 keV X-ray signal, noise level at 4 kHz, and the Joule power calcurated from the IV curve are shown in Fig. 2.7(b)–(d) respectively. Joule power $P = RI^2$ is balanced with heat flow to the sink. Assuming that the thermal conductance $G \equiv \partial P/\partial T$ is represented as $G = G_0 T^{n-1}$, the relation between the Joule power and the temperature can be written as Eq. 2.7. G_0 and n are constants. From Eq. 2.7, $G = 0.91 \pm 0.15$ nW K^{-1} at 151 mK is obtained.

The best energy resolution obtained with this calorimeter is $\Delta E = 6.6 \pm 0.4$ eV at $E = 5.9$ keV and $\Delta E = 6.4 {\pm} 0.3$ eV at $E = 1.5$ keV respectively, in the measurement of the dilution refrigerator in our labo. By using the portable ADR system, $\Delta E = 8.6 \pm 0.3$ eV at $E = 1.5$ keV were obtained. However it was significantly degraded during the plasma measurements as described in § 3.5. The details of the installation to the ADR system are described in § 3.2.

2.1.8 Detective performance of SII-110

In second measurement, SII110 was used to test the duration against the magnetic field. SII110 has the thin Al sheet at the backside of the detector, which is superconducting

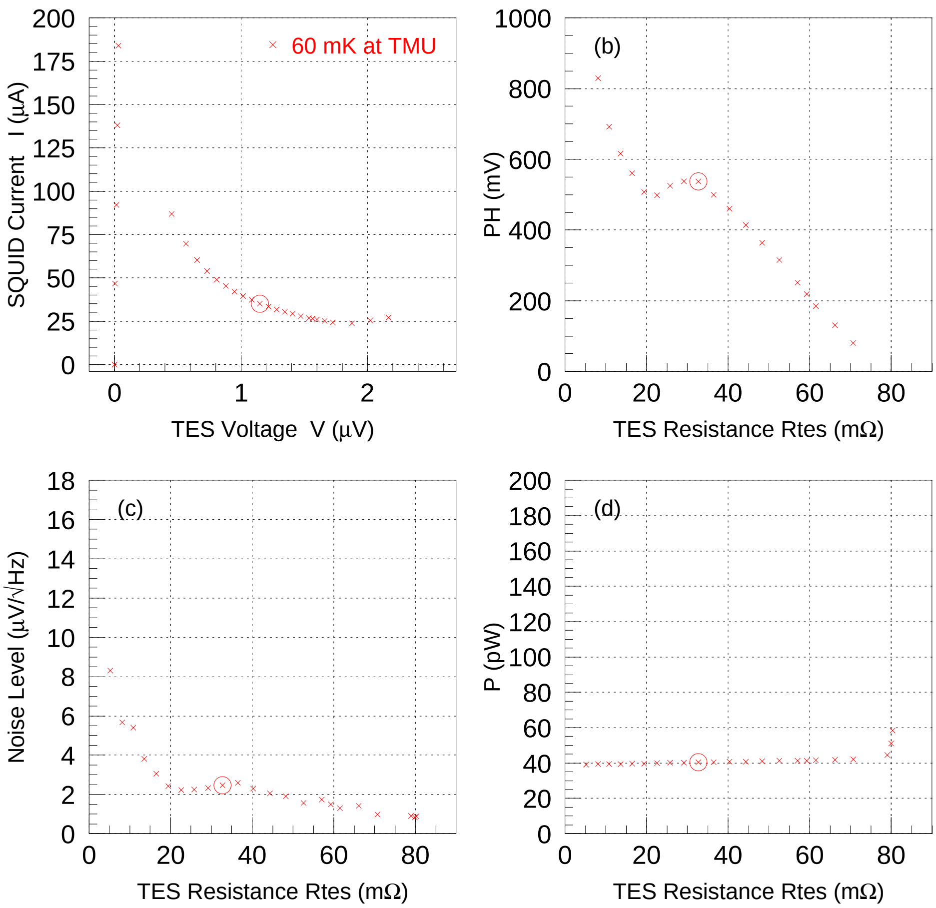

Figure 2.7: (a) Relation between TES current I_{sq} and TES voltage I_{tes} (IV curve). (b) Operating point dependences of the pulse height PH (mV). (c) Operating point dependences of noise level at 4 kHz. (d) Operating point dependences of Joule power calcurated from the IV curve. The results were meausured by using the dilution refrigerator at TMU. Red open circles represents the operating point at which the best energy resolution was obtained.

state at 1.3 K. So that a large hysteresis of a magnetic field during the plasma generation is assumed to be governed in comparison with that for SII14b.

SII110 is also made of a thin bilayer film of titanium (40 nm thick) and gold (70 nm), and a X-ray absorber made of gold (500 nm thick) is also deposited on the TES. A sapphire collimator is 300 μm thick and 200 μm $\times$ 200 μm wide. The transition temperature of the TES is $T_{\mathrm{c}} = 152$ mK and the normal-state resistance is $R_{\mathrm{n}} = 150$ mΩ, as shown in Fig. 2.10. The best energy resolution is $\Delta E = 18.8 \pm 2.9$ eV at $E = 6.4$ keV by using the portable ADR system.

2.2 Cryostat — portable ADR system

The TES calorimeter is needed to cool down to 0.1 K for its high spectral resolution in principle. There are a lot of requiring capability about the system, extreme low temerature, high temperature stability, hold time and so on. Then, we have to introduce an electromagnetic shield around the detector and an X-ray window from room temperature to 0.1 K, while strong thermal connection between a cold bath and a detector stage must be made. Furthermore, the refrigerator which can be operated in the microgravity

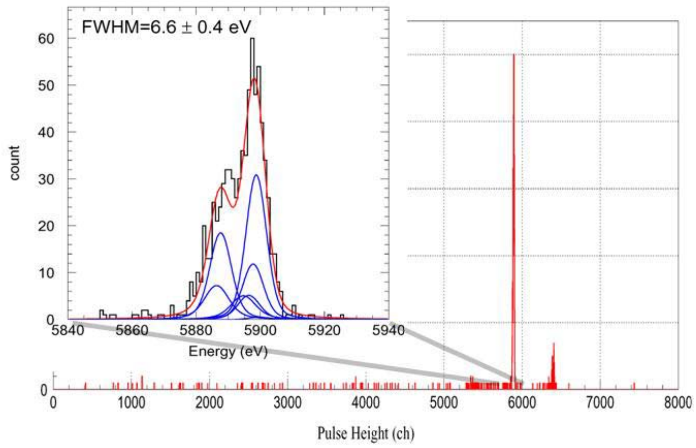

Figure 2.8: Energy spectrum of X-ray signals around 5.9 keV Mn Kα line. It's the measurement by using the dilution refrigerator.

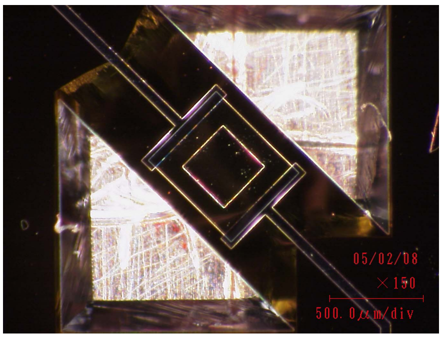

Figure 2.9: Phtograph of SII110, before the sapphire collimator being attached to the detector. There is an Al at the backside of the substrate.

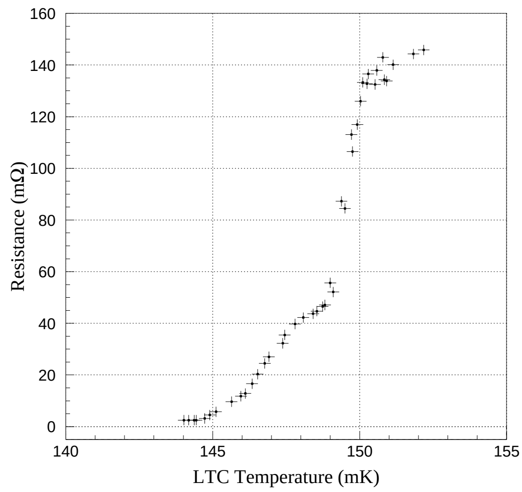

Figure 2.10: Relation between resistance and temperature of the TES, which was obtained by changing the temperature of the detector box, and constant voltage 150 mV.

environment in space, must be used for the detector in an X-ray astrophysical satellite.

In our laboratory, the portable ADR system has been developed for ground experiments, which is based on the system originally designed for the quantum calorimeter sounding rocket experiment by the University of Wisconsin and NASA in USA. An ADR is an almost unique and ideal solution, since it is all solid, and properly works on zero-g condition in contrast to the dilution refrigerator commonly used in the ground experiment. We can learn many important things about the physical property of the TES calorimeter when the detector is mounted on an ADR, in particular about shielding of the magnetic field which is thought to be the most serious noise souce for the detector.

2.2.1 Dewar assembly

Figure 2.12 represents the cross-section of the ADR dewar. The weight is $\sim$ 40 kg and the height is $\sim$ 50 cm. The refrigerator is very compact compared with normal cryogenic

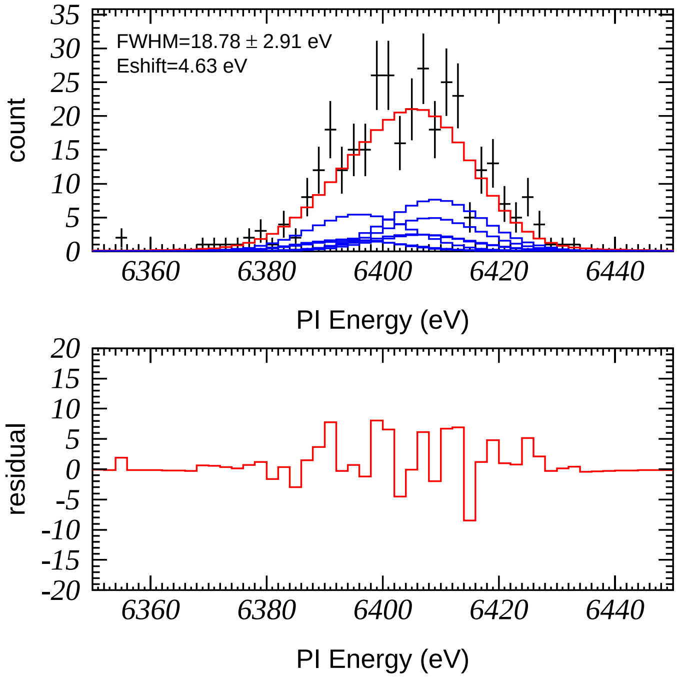

Figure 2.11: Energy spectrum of X-ray signals around 6.4 keV Fe Kα line, We used the X-ray generator, OXFORD sereis-5000 in this measurement.

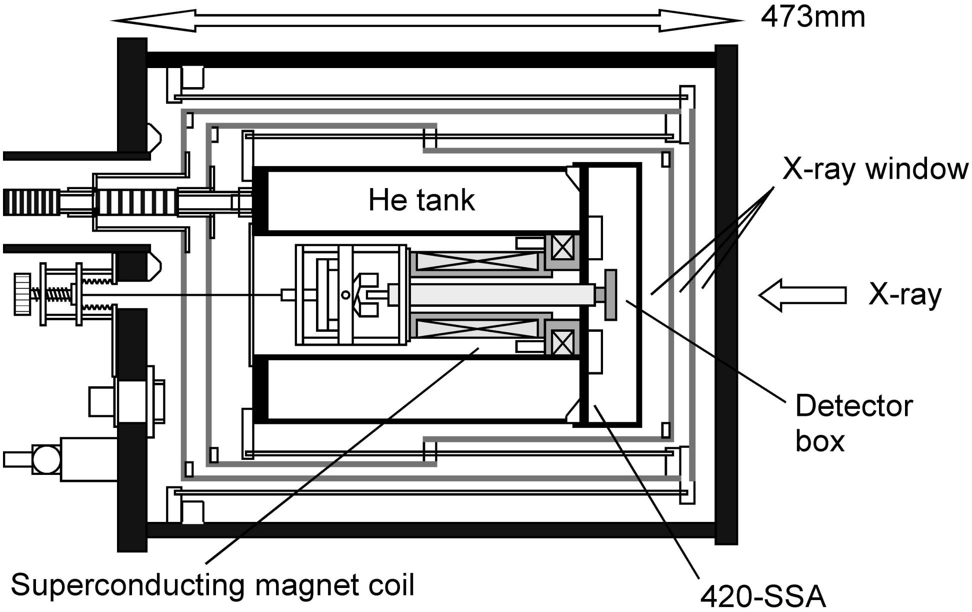

Figure 2.12: The cross-section of the portable ADR used in this experiment. The TES calorimeter is mounted on the detector box and an incident X-ray window is placed in front of the TES calorimeter. This figure shows the sideway operating configuration.

systems having the similar cooling performance. The outer-shell vacuum jacket is made of stainless-steel and two reentrant glass-fiber epoxy resin cylinders sustain the 7.2 ℓ annular liquid He tank for thermal insulation.

For compactness, there is no liquid N_2 dewar, but instead a vapor cooling system is installed to the single L-He transfer/pumping line which is connected to the radiation shields [30], which is shown in Fig. 2.13. More than 90 % of the heat load from room temperature to He tank can be escaped to the evaporated He gas through the line. Our

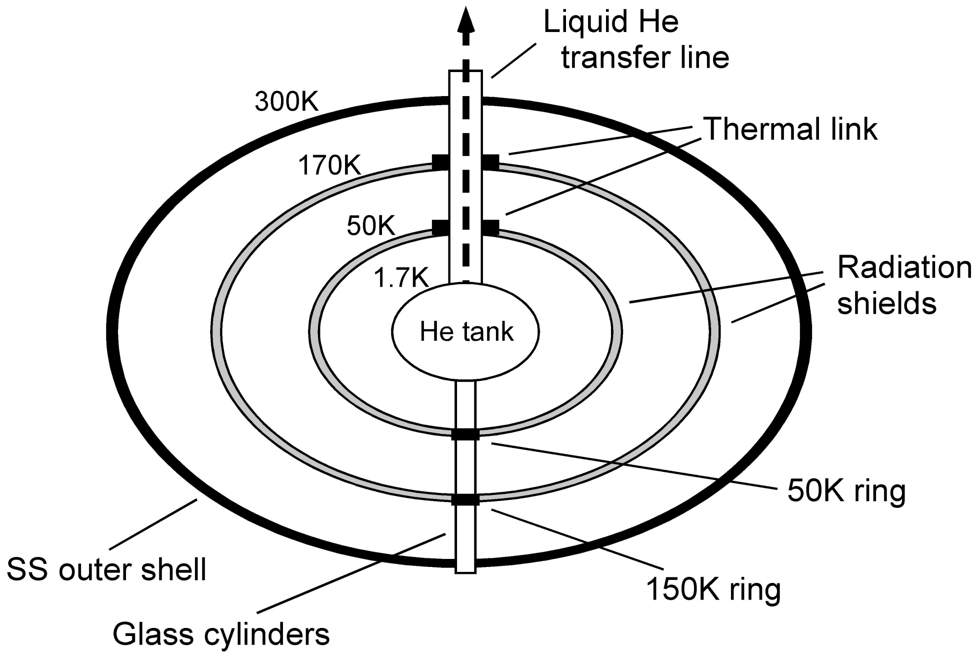

Figure 2.13: Thermal description of the ADR dewar. 2 Al radiation shields are connected to the L-He transfer line. The glass-fiber cylinders are also connected through the radiation shields.

cryostat is slightly different from that of McCammon et al. [20] in the inner Al radiation shield. We added the shield in the front part of the dewar between the outer and the pumped L-He temperature shield. The temperatures of the outer and inner shields are about 150 K and 50 K, respectively, while the pumped L-He bath has a temperature of 1.7 K.

Recently, we reconstructed the L-He transfer line and succeeded to have the twice longer hold time of liquid He, which is one of most important problems in this plasma measurement.

One of the key features of this cryostat is that it can operate in both vertical and sideway configurations. In the sideway configuration, the cooling efficiency, temperature fluctuation of the detector box, holding time at 100 mK, and the basic operation of the X-ray detector are almost the same at the normal vertical configuration. Since the usable volume of the L-He tank is smaller in the sideway configuration, the holding time of the pumped L-He is about 14 hours, compared to the 24 hours in the vertical configuration. We can transfer L-He in both configurations, and the L-He consumptions are about 9 ℓ in the sideway and about 7 ℓ in the vertical configuration, respectively.

2.2.2 Cooling cycle and the construction of the dewar center

theory of paramagnetic material

Adiabatic Demagnetizatiion is a cooling method by using a physical property of a paramagnetic material in low temperature. Typically, a 3d-group transition metals or rare earth elements which has unpaired electrons in the outer shell are utilized as the magnetic material of ADRs. The total angular momentum quantum number J of the localized spin is expressed with a sum of spin angular momentum S and orbital angular momentum L (LS-coupling). In the applied magnetic field of B at the temperature of T, the magnetization $M(T, B)$ for the N spin system is represented by a Brillouin function as

$$M(T,B) = Ng\mu_{\mathrm{B}}J\left\{\frac{2J+1}{2J}\coth\left(\frac{2J+1}{2J}x\right) - \frac{1}{2J}\coth\left(\frac{x}{2J}\right)\right\}, \tag{2.29}$$

in which $x \equiv g\mu_{\mathrm{B}}BJ/k_{\mathrm{B}}T$, g is the Landé factor, μ_{B} is the Bohr magneton, and k_{B} is the Boltzmann constant. Then the magnetic entropy, $S(T,B)$, is,

$$S(T,B) = Nk_{\mathrm{B}}\ln(2J+1) + \int_0^B \left(\frac{\partial M}{\partial T}\right)_{B'} \mathrm{d}B'. \tag{2.30}$$

In fact, B is the magnetic field which contributes to the spin, and is represented by the superposition of the internal spin b and the external field B_0, as

$$B = \sqrt{b^2 + B_0^2}. \tag{2.31}$$

When the thermal energy is dominant, namely $x \ll 1$,

$$M(T,B) = \frac{CB}{\mu_0 T}, \qquad C = \frac{N\mu_0 g^2\mu_{\mathrm{B}}^2 J\,(J+1)}{3k_B}. \tag{2.32}$$

The former equation in Eq. (2.32) is known as the Curie's law, and C is the Curie constant. As a result, the Eq. (2.30) of the entropy is reduced to

$$S(B,T) = Nk_B\ln(2J+1) - \frac{CB^2}{2\mu_0 T^2}. \tag{2.33}$$

We must pay attention to the condition that $x \ll 1$. This means that the thermal energy, $k_{\mathrm{B}}T$, is much higher than the magnetic energy, $g\mu_{\mathrm{B}}BJ$. When magnetic field is degreased adiabatically, B/T must stay constant with $S =$ constant. We thus obtain

$$B_{\mathrm{High}}/T_{\mathrm{High}} = B_{\mathrm{Low}}/T_{\mathrm{Low}} \tag{2.34}$$

From the relation $T_{\mathrm{Low}} < T_{\mathrm{High}}$, low temperature is generated by using a paramagnetic material as a cooling medium. With Eq. 2.33, the heat capacity at constant field is given by

$$C_{\mathrm{B}} = \frac{CB^2}{\mu_0 T^2} \tag{2.35}$$

C_{B} becomes very high value, while lattice heat capacity originating from phonons $C_{\mathrm{L}}(T)$ ($\propto T^3$), and electoric heat capacity originating from conduction electrons $C_{\mathrm{e}}(T)$ ($\propto T$) become lower values in low temperature, so that it's useful to refrigerate any components with paramagnetic materials at < 1 K.

cooling cycle

When the cooling cycle of an ADR is considered, it's simple to explain the adiabatic demagnetization with the temperature — entropy diagram of the paramagnetic material, which is shown in Fig. 2.14. We assume that by means of suitable precooling, for instance by pumping on a bath of liquid helium, point X, at an initial temperature T_{H} and zero magnetic field, is reached. The material is then magnetized isothermally, in contact with the He bath, to $B_0 = B_{\mathrm{H}}$, along the path X $\rightarrow$ Y. The change in the heat content of the material during isothermal magnetization from X to Y at $T = T_{\mathrm{H}}$ is $\Delta Q = T_{\mathrm{H}}\Delta S$. For paramagnetic materials, $\Delta Q(T = T_{\mathrm{H}}) < 0$. The emergent energy is absorbed by the He

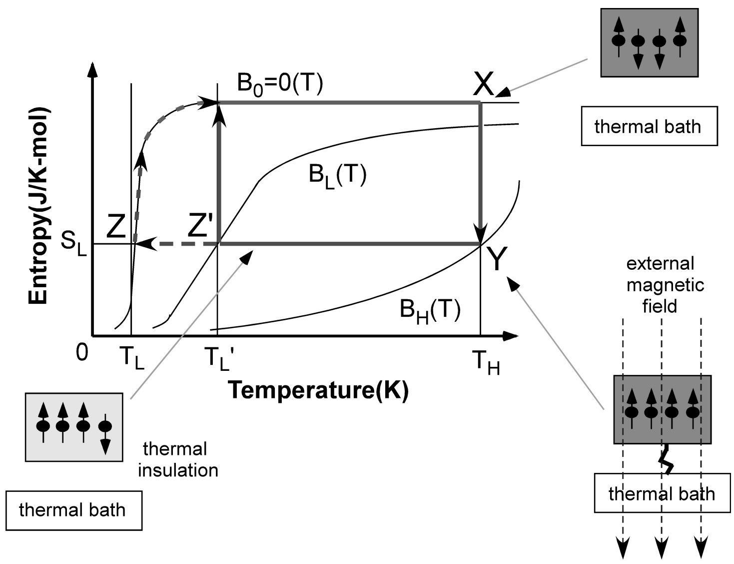

Figure 2.14: Cooling cycle of an ADR on the temperature — entropy diagram. The condition of localized spin in each state are also shown. Thick solid line represents the physical cycle during the adiabatic demagnetization. Thin solid line shows the entropy behavior under a certain constant magnetic field.

bath. Then during adiabatic demagnetization from Y to Z ($B_0 = 0$) the entropy stays constant. The arrival temperature $T_{\rm L}$ is

$$T_{\rm L} = \frac{T_{\rm H}}{\sqrt{b^2 + B_{\rm H}^2}} \times b \tag{2.36}$$

$T_{\rm L}$ after demagnetization depends on $B_0 = B_{\rm H}$ and b. We selected ferric ammonium alum — FAA ($b = 0.05\ T$) as the paramagnetic salt, so that $T_{\rm L} \sim 30$ mK is predicted.

Owing to the external heat leak the system then begins to warm up along the $B_0 = 0$ curve. When the arrival temperature must be kept constant, adiabatic demagnetization can be stopped at Z', and control the B_0 to keep the temperature $T_{\rm L'}$.

assembly of the center in the ADR

Fig. 2.15 shows the center of the ADR, the required components for adiabatic demagnetization which is mounted in the central hole of the He tank. The salt pill, in which a 87 g ferric ammonium alum [$FeNH_4(SO_4)_2 \cdot 12H_2O$] as a magnetic material is filled, is installed to the center. The FAA crystal however has become slightly deteriorated, the internal field, b, in our FAA salt is somewhat larger than that of of a complete FAA crystal. The salt pill is suspended by six Kevlar supports. The superconducting solenoid coil is around the salt pill, and it has a thermal link to the pumped He tank at 1.7 K. The maximum magnetic field is 2.85 T at the magnet current of 5.5 A.

There is a bucking coil in the solenoid coil to cancel the magnetic field at the detector box. We measured the loss of the magnetic field around the detector box and at the bottom of the He tank, on which the SQUID array was mounted, during the cooling time. The results are shown in Fig. 2.16. In this measurement, we used the hole detector which could detect the field more than 30 Gauss, so that it caused to have an offset in the results (left in Fig. 2.16). During the cooling cycle, the maximum field at the bottom of He tank is ~ 700 Gauss, we have to shield the SQUID array with μ-metal cryoperm and superconducting Nb box, to cancel it.

Actually, there are also the cryoperm around the detector box, and superconducting Al/Pb shields are installed around the TES calorimeter (in Sec. 3.2). The magnetic

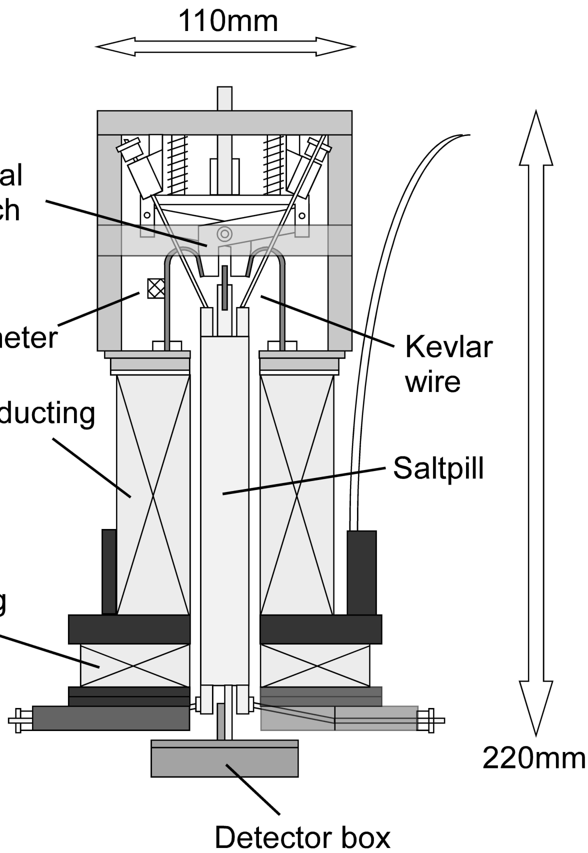

Figure 2.15: The assembly of the center in the portable ADR. The supeconducting magnet, the bucking coil, the mechanical heat switch are installed around the salt pill in which the FAA is sealed. The detector box on which the TES calorimeter is mounted is directly connected to the salt pill.

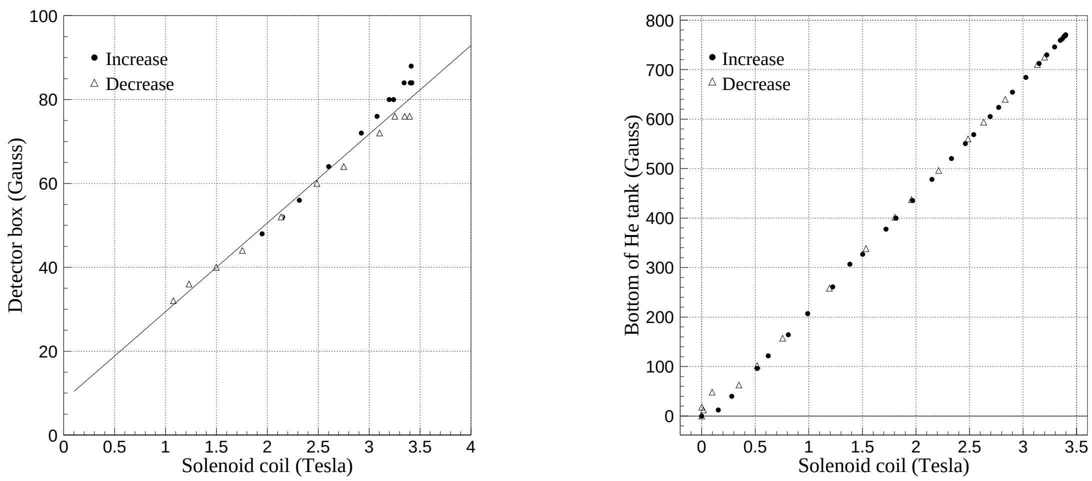

Figure 2.16: The experimental result of the loss of the magnetic field around the detector box (left) and at the bottom of the He tank (right). In left panel it has an offset of y-axis in this result, which is caused by the uncertainty of the hole detector. Solid line shows the fitting result.

field requied to keep at 100 mK is $\sim$ 1000 Gauss, we assume that less than 0.1 Gauss is generated around the TES calorimeter at 100 mK, Though the RuO_2 thermometer, which we use to measure the temperature of the detector box (in Sec. 3.2), is little affected by the magnetic field, we assume that the effect is negligible.

The mechanical heat switch (on: > 18 mW/K) is above the top of the salt pill. The Kevler support is connected between the heat switch and the actuator at the outside of the dewar, and it works by pulling the support with the actuator during the cooling cycle. We used copper springs to the assembly around the salt pill, not to magnetize, which causes the noise of the TES.

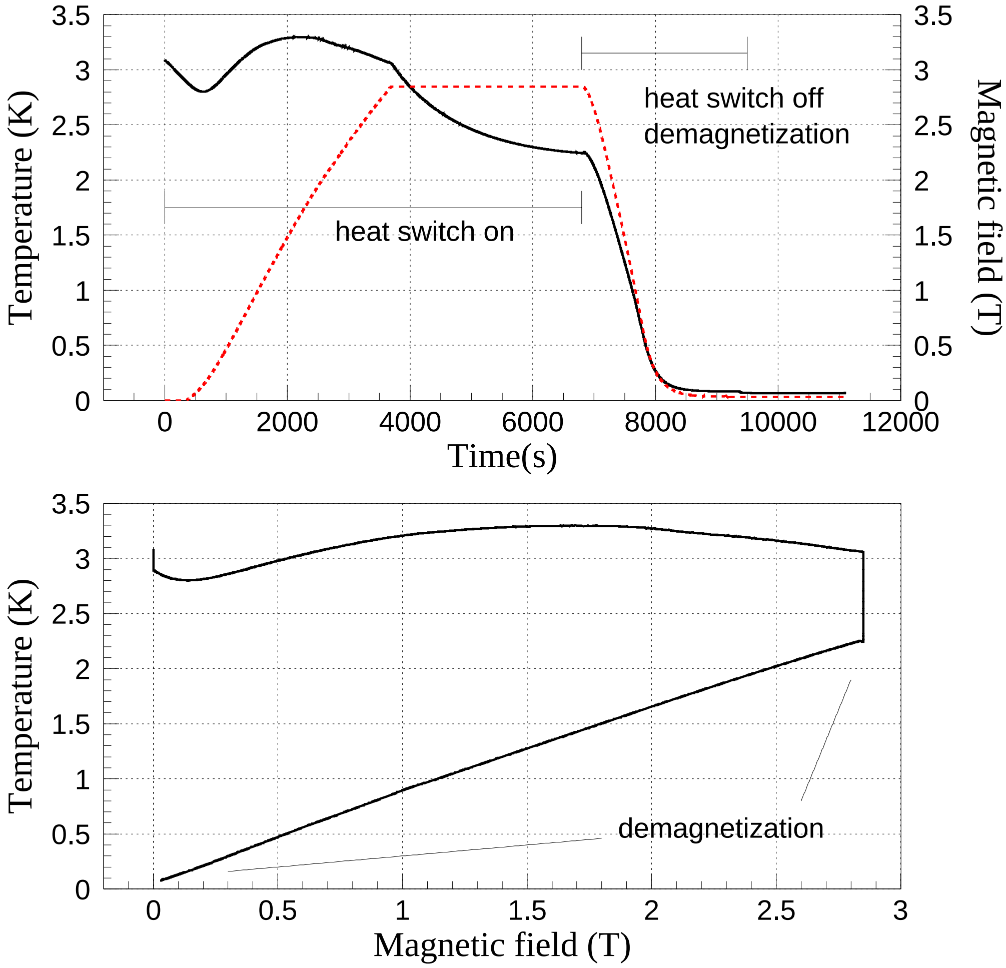

Figure 2.17: Top : Typical curve of the temperature of the detector box (black solid lines) and the magnetic field of the superconducting coil (red dotted) during the thermodynamic cycle of the ADR. Bottom : Relation between the temperature of the detector box and the magnetic field during the cooling cycle.

Table. 2.1 shows the cooling performance of the ADR. Typical curve of the temperature of the detector box and the magnetic field of the superconducting coil during the thermodynamic cycle of the ADR are shown in Fig. 2.17. In the adiabatic demagnetization, the magnet coil slightly warms up so that the typical temperature of the salt pill at the beginning of demagnetization is 2.2–2.4 K, somewhat larger than 1.7 K of the He tank.

2.3 Temperature control

It is also a merit of the ADR that the temperature can be controlled quite precisely by controlling the current of superconducting magnet surrounding the salt. On the other hand, when the magnetic spins are completely randomized, i.e., no more heat can be absorbed, a "recharge" of the refrigerator is necessary. The period to the next recharge,

Table 2.1: Cooling performance of the ADR in our labo.

hold time of liquid He (vertical)	20–22 hours
hold time of liquid He (sideway)	14–16 hours
temperature of pumped liquid He tank	1.7 K
paramagnetic material	FAA (0.187 mol)
heat capacity at 100 mK	3.3 J K^{-1} mol^{-1}
heat inflow at 100 mK	0.6–0.8 μW
minimum temperature of the salt pill	65 mK
hold time at 100 mK	12 hours

i.e., temperature controlled time, depends on the heat input to the salt, the temperature to maintain, and the size of the salt.

Usually, PID (Proportional, Integral, and Derivative control) method is used to temperature controls in refrigerators. PID is one kind of basic feedback controls, which controls the required value by operating the power(strongly associated with the value) with three parameters, residuals between set value and measured value, derivative value, and integral power. In our ADR, value means temperature and we used the current of the superconducting magnet as a power. However, because heat capacity of the salt pill is small for compact ADRs, difficulties arises in keeping constant temperature for a long time. Particularly, we found small residual temperature difference between the aimed and measured temperatures, which gradually increased in time when we controlled the temperature of our ADR with the standard PID method. The problem originates in the principle of the standard PID which is naively applied to ADRs, making it critical to keep stable temperature with a small refrigerator. Bernstein et al. [9] have demonstrated quite steady control of the ADR temperature by rejecting thermometry readout noise and optimizing varying parameters which determine dI/dt, although their method assumes the magnet current, I, is sufficiently high. We have succeeded in solving the problem with an improved PID method by adding a new term in the standard PID considering the physical properties of the paramagnetic salt, and use it with our portable ADR system. The improved PID method is considered to be of great advantage especially in the range of small magnet current. In this section, we introduce the means of temeprature control, outline of the improved PID method, and the experimental results with our ADR system are presented.

2.3.1 PID method — theory

With regard to usual refrigeration systems which have a cold bath and an experimental stage equipped with a resistive heater, the temperature, T, of the experimental stage is usually controlled by the heater output, $w(t)$, in dimension of W, making use of the standard PID method. In this case, heat load on the experimental stage, $w_{\rm L}(t)$, and the heat outflow into the cold stage, $w_{\rm out}(t)$, should be balanced with $w(t)$, as

$$\overline{w(t)} + \overline{w_{\rm L}(t)} = \overline{w_{\rm out}(t)}, \tag{2.37}$$

in which $\overline{w(t)}$ represents the time average of $w(t)$. Here, $w_{\rm L}(t)$ is almost constant with a small level of fluctuations, and the $w_{\rm out}(t)$ is determined by the thermal conductivity and the temperature difference between the experimental stage and the cold bath. In the standard PID method, the $w(t)$ is determined with a formula,

$$w(t) = \frac{\mathcal{I}}{\Delta t}\int_{t-\Delta t}^{t} w(t')\,{\rm d}t' - \mathcal{P}\ \{T(t) - T_{\rm aim}\} - \mathcal{D}\,\frac{dT}{dt}(t) \tag{2.38}$$

in which $T_{\rm aim}$ is the aimed temperature to maintain, and $\mathcal{P}$, $\mathcal{I}$, $\mathcal{D}$, Δt are the non-negative constant parameters. The first term with $\mathcal{I} \simeq 1$ represents the constant heater output when perfectly $T = T_{\rm aim}$, and the second or third term indicates the compensational heater output in proportional to the difference or differential of the measured temperature, respectively.

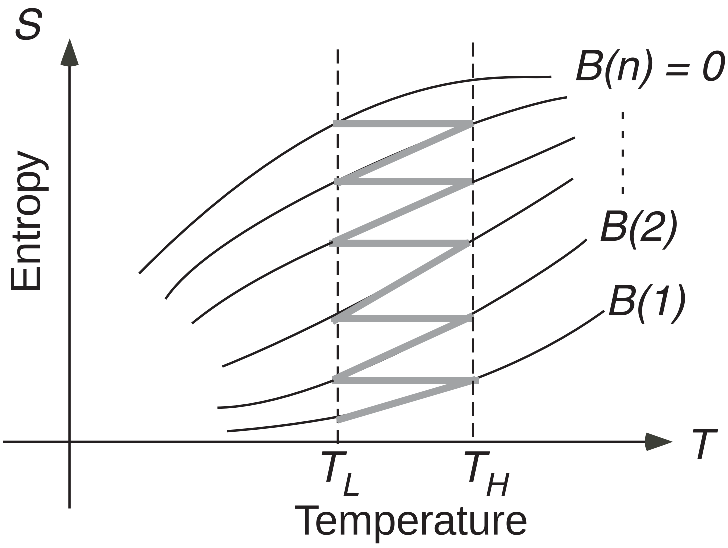

Figure 2.18: A schematic example of the temperature control with ADRs, plotted on the entropy-temperature plane. Each of solid lines indicates the entropy behavior of the paramagnetic salt under a certain constant magnetic field. See text in detail.

On the other hand in the ADR systems, the experimental stage is stiffly connected to the refrigerant salt itself, so that the temperature, T, of the experimental stage is almost equivalent with the temperature of the salt pill. We can control the heat absorption, $w_{\rm a}(t)$ in the salt pill by changing the current, $i(t)$, of the superconducting solenoid magnet. It is also notable that warming and cooling are both capable with ADRs by increasing or decreasing the current, while resistive heaters can do only warming. Figure 2.18 represents a schematic example of the temperature control with ADRs. Each of solid lines indicates the entropy behavior under a certain constant magnetic field, plotted versus temperature. The magnetic field is weaker for upper lines. Under the constant magnetic fields of $B(1)$, the temperature slowly increase due to the heat input $w_{in}(t)$ from the bottom point towards the upper-right direction along the solid line. At some point where the temperature difference is significant, the magnetic field is reduced to $B(2)$ by decreasing the magnet current and the sate of the ADR jumps to the upper solid line. This step occurs in a short time scale through closely adiabatic path, so that the entropy, S, is preserved and the temperature is lowered. Repeating these steps with sufficient minuteness, the temperature of the ADR salt can be controlled quite precisely, usually to the level of the temperature determination accuracy. Ideally, we can control the temperature until the magnet current, $i(t)$, reaches down to zero.

In order to stabilize the ADR temperature, the equation to balance is,

$$\overline{w_{\rm a}(t)} = \overline{w_{\rm in}(t)}, \tag{2.39}$$

while $w_{\rm a}(t)$ is a complicated function of B, T, and other ADR specific parameters, as described in the next subsection. Therefore, the easiest way in incorporating the PID method to ADRs is to replace $w(t)$ in Eq. (2.38) with $i(t)$. There is a similarity between $w(t)$ and $i(t)$ that increasing (or decreasing) the value corresponds to raising (or lowering) the temperature. One difference is, however, that $i(t)$ must be decreased gradually to zero, in long-range time scale. In order to taking into account this effect, we have introduced another term, $F(t)$, into Eq. (2.38) as,

$$i(t) = \frac{\mathcal{I}}{\Delta t} \int_{t-\Delta t}^{t} i(t')\,\mathrm{d}t' - \mathcal{P}\,\{T(t) - T_{\mathrm{aim}}\} - \mathcal{D}\,\frac{dT}{dt}(t) + F(t). \tag{2.40}$$

Throughout this thesis, we call the temperature control method based on this equation with $F(t) \neq 0$ as an improved PID method, and the method with $F(t) = 0$ as the standard PID method. Considering the fact that the first term roughly equal to $\dfrac{i(t) + i(t-\Delta t)}{2}$ when $\mathcal{I} = 1$, the $F(t)$ should follow

$$F(t) \simeq \frac{i(t) - i(t-\Delta t)}{2} \simeq \left(\frac{\Delta t}{2}\right) \frac{di}{dt}(t), \tag{2.41}$$

ignoring the second and third term. Because the $i(t)$ gradually decreases, $F(t)$ is always negative. This value is usually small compared with the fluctuation of the actual setting of $i(t)$, hence it is not realistic to determine $F(t)$ at each time by numerically differentiating $i(t)$. To specify the functional form of $F(t)$, there needs a help of the theory on magnetism.

2.3.2 heat balance during temperature control

Again, the theory of paramagnetic material must be considered to describe the physical property of ADR during the temperature control with Eq. 2.40. To make it simple, the heat inflow, w_{in}, is assumed to be constant. The thermal energy due to w_{in} during the time δt is $w_{\mathrm{in}}\delta t$. This energy input must be balanced with the heat absorption in the salt pill, $w_{\mathrm{a}} = T\delta S$. Here we put $B_0 = c_1\, i$, and using Eqs. (2.31) and (2.33), then we derive

$$w_{\mathrm{in}}\delta t = w_{\mathrm{a}}\delta t = T\delta S = -\frac{c_1^2 C}{\mu_0 T}\, i\,\delta i, \tag{2.42}$$

in which the internal field, b, is cancelled out. Therefore,

$$\frac{di}{dt}(t) = -\frac{\mu_0\, w_{\mathrm{in}}\, T}{c_1^2\, C}\,\frac{1}{i(t)} = -\frac{\mathcal{A}^2}{2}\,\frac{1}{i(t)}, \tag{2.43}$$

in which $\mathcal{A} \equiv \sqrt{2\,\mu_0\, w_{\mathrm{in}}\, T/(c_1^2\, C)}$. Combining Eqs. (2.40), (2.41), and (2.43), formula of the improved PID method can be written as,

$$i(t) = \frac{\mathcal{I}}{\Delta t} \int_{t-\Delta t}^{t} i(t')\,\mathrm{d}t' - \mathcal{P}\,\{T(t) - T_{\mathrm{aim}}\} - \mathcal{D}\,\frac{dT}{dt}(t) - \frac{\mathcal{A}^2\,\Delta t}{4\,i(t)}. \tag{2.44}$$

2.3.3 Actual setup

The experimental setup and several parameters of the refrigerator are shown in Fig. 3.2 and Table 2.1. The details are described in Sec. 3.2. We stabilize the temperature of the experimental stage — detector box by controlling the current of the superconducting solenoid magnet ($c_1 = 0.518$ T A^{-1}) according to Eq. 2.44. The temperature was monitored with the RuO_2 (Ruthenium-Oxide) thermometer attached on the detector box. The thermometer resistance was measured using the temperature monitor, Cryo-con Model 62, with the four wire connection, and the filter time constant was set to 8 sec. The inherent noise of the thermometer bridge is measured as rms $= 5.0\ \mu$K with a constant resistor placed at 100 μK in the ADR. The self-heating of the thermometer is less than 1 pW, which is much smaller than the heat inflow (Table 2.1), and the temperature difference between the thermometer and the detector box is negligible. The magnet current

Table 2.2: The PID parameters for the experiment.

$\mathcal{P}$	=	114 mA K^{-1}
$\mathcal{I}$	=	1.0
$\mathcal{D}$	=	5500 mA K^{-1} sec
$\mathcal{A}$	=	0.544 mA sec$^{-1/2}$
$i_{\rm off}$	=	2.5 mA
Δt	=	1.0 sec

was controlled by the current controller, Keithley 2400, with the finest resolution of 5 μA. Both the temperature monitor and the current controller were connected to a laptop computer (PC) with GPIB bus, which conducted the temperature control according to the PID calculations.

The operation of the temperature control is done in the 1 sec cycle, although the thermal time constant between the detector box and the salt pill is less than 1 sec. Namely, the temperature acquisition, calculation, and setting of the new magnet current are done at every 1 sec. In order to calculate the next magnet current, $i(t+\Delta t)$, there need the temperature, $T(t)$, the temperature differentiation, $\frac{dT}{dt}(t)$, and the magnet current, $i(t)$, in Eq. (2.44). These values tend to be affected by noises in actual situations, we therefore average these values in the previous 60, 15, and 15 samples, respectively.

The heat capacity of the other components attached to the salt pill is quit smaller than that of FAA at the lowest temperature. Because the hold time of the pumped liquid ^{4}He is $\sim$ 24 hour, which is sufficiently longer than the temperature controlled time of the cold part at 100 mK in the single ADR cycle, the heat inflow to the cold part can be regarded to constant (0.6–0.8 μW at 100 mK, shown in Table. 2.1).

2.3.4 Actual performance of temperature control

Typical temperature control results with the standard PID and the improved PID method are shown in Fig. 2.19. In these experiments, the parameters for the improved PID method are summarized in Table 2.2, in which we add a small offset, $i_{\rm off} = 2.5$ mA, to the magnet current, $i(t) \equiv \tilde{i}(t) + i_{\rm off}$, to avoid the divergence of the term $\frac{\mathcal{A}^2\,\Delta t}{4\,i(t)}$ to infinity when $i(t) \to 0$. Here, $\tilde{i}(t)$ is the actual current set by the current controller. After $\sim$10 ks when the magnet current becomes lower than $\sim$30 mA, the difference between the two is noticeable. In the improved PID method (Fig. 2.19 (a)), it keeps constant temperature at 100 mK, while the temperature begins to rise in the standard PID method (Fig. 2.19 (b)). The mean temperature of the improved PID is well consistent with the aimed temperature of 100 mK, while it is significantly shifted by $\sim$20 μK with the the standard PID (Fig. 2.19 (d)). The temperature dispersion in the whole time range is by about 1.5 times smaller for the improved PID with rms = 11.0 μK. In addition, the magnet current for the improved PID ramps down to zero slower than that for the standard PID (Fig. 2.19 (c)). It might be suggested that the eddy-current heating were reduced due to smoother temperature control. The two experiments were conducted in the same day without warming up the cryostat, it is unlikely that the parasitic heat leak had changed between the two. We have cooled our ADR system more than 100 times since 2002, and the reproducibility of the ramping time was typically $\sim$10%. In this aspect, however, the difference is not significant.

The temperature dispersion in a shorter time scale between 2000–4000 sec is derived

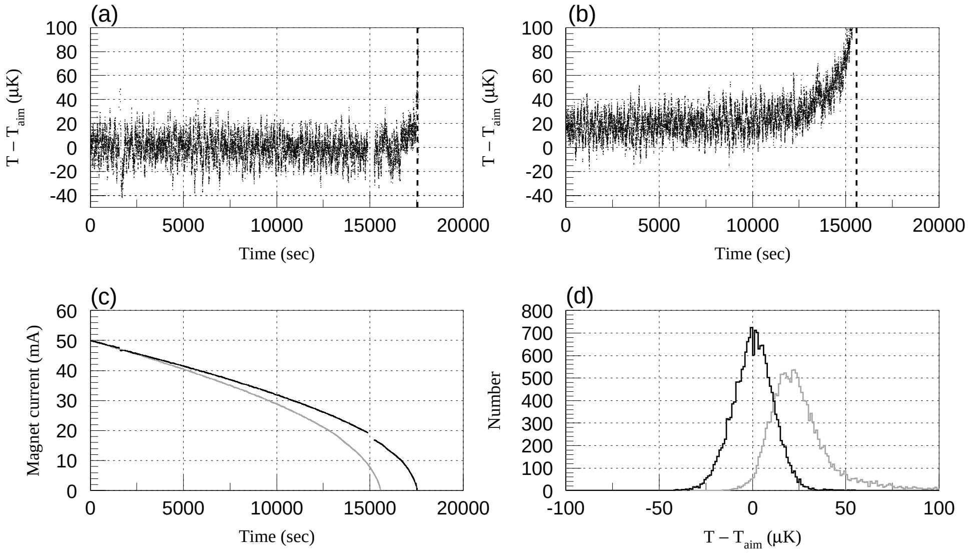

Figure 2.19: Typical results of the temperature control experiments with the aimed temperature of $T_{\rm aim} = 100$ mK to maintain. (a) The measured temperature residual, $T - T_{\rm aim}$, in unit of μK plotted versus time in second with the improved PID method. (b) Similar to (a) with the standard PID method. (c) The magnet current, $\tilde{i}(t)$, in unit of mA plotted versus time in second. The solid black line represents the magnet current with the improved PID, and the gray line is that with the standard PID. (d) Histograms of the residual temperature at each second for both methods in the whole time range plotted in (a) and (b). Regarding to the improved PID (black), mean of the temperature residual is 0.3 μK and rms is 11.0 μK. For the standard PID (gray), mean is 25.1 μK and rms is 16.3 μK.

to be rms $=$ 9.4 μK for the improved PID and rms $=$ 9.9 μK for the standard PID. Both of which is close to but slightly above the inherent noise of the thermometer bridge. It is indicated that the temperature stability is almost the same in both method in the shorter time scale. These results mean that we can extend the period to keep constant temperature by $\sim 30\%$ with high temperature accuracy of ~ 10 μK rms. The improved PID method is supposed to be of great advantage especially in the range under 30 mA ($\lesssim 150$ Gauss), which is comparable to the internal field of the FAA.

By solving Eq. (2.43), dependence of the magnet current on time is derived as

$$i(t) = \tilde{i}(t) + i_{\rm off} = \mathcal{A}\sqrt{t_0 - t}\,, \tag{2.45}$$

in which t_0 is the integral constant, and $\tilde{i}(t)$ is the actual current set by the current controller. We have determined the values of $\mathcal{A}$, t_0 and $i_{\rm off}$ in Table 2.2 by fitting the previously obtained curve of the magnet current like Fig. 2.19(c). The existence of $i_{\rm off}$ means that the internal magnetic field, b, should be considered in the low current situation. There also need a caution that the assumption of $x \ll 1$ for Eq. (2.32) is beginning to break in such situation.

It is also capable to calculate the predicted value of $\mathcal{A}$ using the theoretical values for our FAA salt. It is derived that $\mathcal{A} = 0.234$–0.270 mA sec$^{-1/2}$, which is similar to the experimental result. The difference between the predicted value and the experimental result is supposed to be within the uncertainties of the included values, approximation in the theory of magnetism, and the magnetic hysteresis of the FAA salt. Finally, we can predict the maximum control time, $t_{\max}$, by solving Eq. (2.45) as,

$$t_{\max} = \frac{\left\{\tilde{i}(t) + i_{\mathrm{off}}\right\}^2 - i_{\mathrm{off}}^2}{\mathcal{A}^2}, \tag{2.46}$$

assuming $\tilde{i}(t + t_{\max}) = 0$.

2.3.5 Temperature dispersion in various temperature

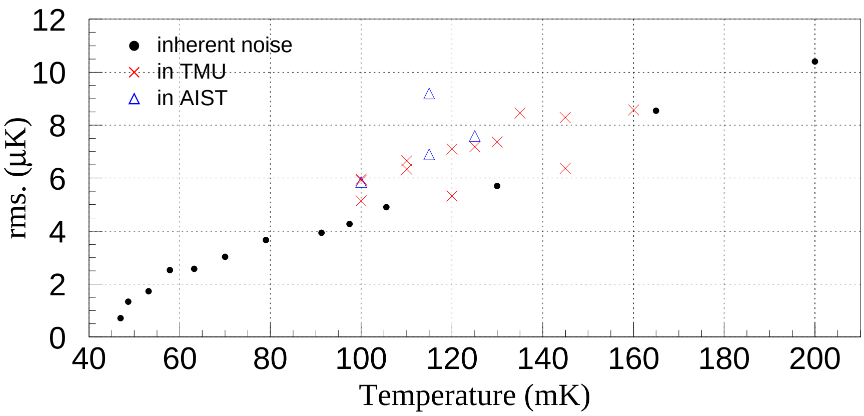

Figure 2.20: Temperature dispersion in various temperature. Filled circles represent the expected inherent noise of the thermometer bridge, and red crosses represent the measured dispersion in unit of μK. Blue triangles represent results in AIST.

Measured temperature dispersions during the control in various temperature are shown in Fig. 2.20. We used the controlled time of more than 1,500 sec for each result to calculate the dispersions. We overplot the inherent noise of the thermometer bridge expected by measuring constant resistors. We suggest that the temperature dispersions of the system are mostly achieved to the controlled limit for the inherent noise of the thermometer bridge, and the constant parameters $\mathcal{P}$, $\mathcal{I}$, $\mathcal{D}$, Δt are mostly optimized to avoid oscillating.

2.4 IR-UV blocking filters for X-ray window

High X-ray throughput below 1 keV is strongly required in X-ray astronomy mission as well as for the soft X-ray measurement of ground based plasma. IR to UV blocking filters are indispensable for refrigerators of such a space mission, hence material and design of the filters determine overall X-ray detection efficiency. In this section, the X-ray window introduced to the ADR system is presented.

2.4.1 Choice of filters and setup

An X-ray window of the cryostat has to attenuate thermal radiation from the room temperature to the cold plate which degrades the detector performance, and at the same time it needs to give enough X-ray transmission. To observe the soft X-rays down to the 500 eV range with good efficiency, we employed five 37 nm aluminum filters in series, each of which was supported on a 540 nm Toray Lumirror ($C_{10}H_8O_4$) substrate. As indicated in Fig. 2.21, these filters are placed on the 150 K, 50 K, and 3 K($\times$2) shields,

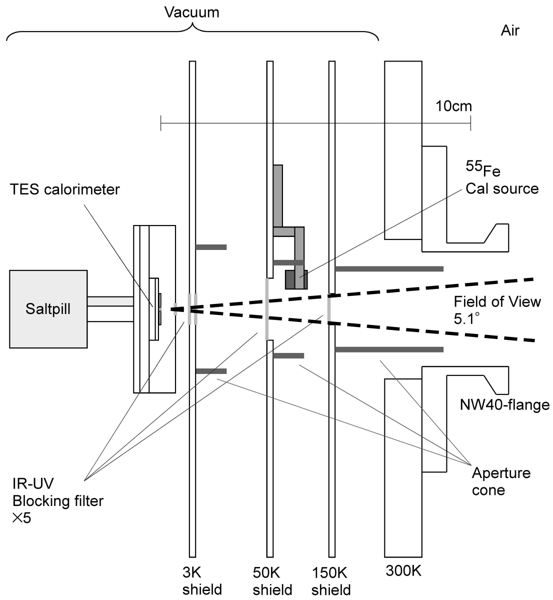

Figure 2.21: The cross-sectional view of the X-ray window. The filters are installed in 150 K, 50 K, and 3 K shields (×2) and the cryoperm shield of the detector box. The field of view is about 5.1°. The calibration isotope (^{55}Fe) is mounted above the 50 K filter without interfering the line of X-ray incidence.

and the cryoperm shield box of the detector. The field of view is designed to be about 5.1° ($\sim$ 6.2 $\times$ 10^{-3} str), though there may be a small inclination between the X-ray incident axis and the direction defined by each filter. The angular size is determined by the filter at the 150 K shield with 10 mmϕ. The overall detector efficiency, including the transmissions of all the windows and the quantum efficiency of the TES calorimeter, is indicated in Fig 2.22 (a). In the case of the experiment conducted in second measurement, we installed higher transmission X-ray windows using thin Parylene-N films. It uses five 70 nm aluminum filters in series, deposited on a 100 nm Parylene-N (C_8H_8) substrate. The aluminum thickness of 70 nm is the thinnest product we could purchase for the Parylene-N filters. The Parylene-N film does not contain oxygen, nitrogen, or any other high-Z material, therefore the Parylene-N films significantly improve the transmission in the energy range around 600 eV, compared with the Toray Lumirror films which contain oxygen. On the other hand, the Parylene-N films are much more fragile than the Torray-Lumirror films, two out of five films are supported with meshes, each of which has 86 % transmission. Transmissions for both filters are presented in Fig 2.22 (b) (see in Sec. 2.4.2). We also introduced aperture cone structures in front of the films to protect them from adhesion of contaminant for second experiment.

2.4.2 Transmission measurement with soft X-ray generator

In our laboratory at TMU, we measured the transmission of the X-ray window using a continuum spectrum from a soft X-ray generator, Manson Model 3B. The ADR system was connected to the X-ray generator with a vacuum duct, and the X-ray spectra from the electron beam target, Al, were obtained by cooling down to 100 mK in both setups. We observed bremsstrahlung continuum and fluorescence lines from the electron target modified with C- and O-edges of the filters and strong C-/O-K$_\alpha$ lines as shown in Fig. 2.23. In Setup I, 4 $\times$ 540 nm Toray Lumirror films were introduced while 4 $\times$ 100 nm Parylene-N films were used in Setup II. We note that number of films in both Setup I and Setup II were different f rom that in the plasma measurement respectively. The thickness of each

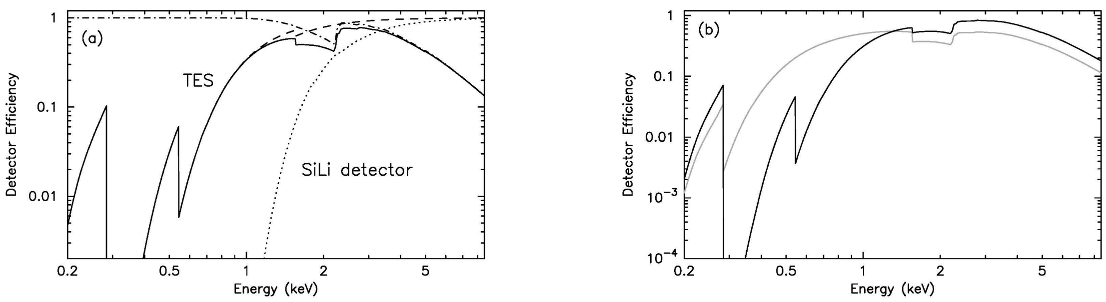

Figure 2.22: (a) The detector efficiencies of the TES calorimeter (solid line) and SiLi detector (dotted) including the transmission of the ADR X-ray window (dashed) and the quantum efficiency of the TES calorimeter (dot-dashed). (b) Comparison of the expected detector efficiency in first measurement (black solid, same as (a)) with 5×540 nm Toray Lumirror films, and that in second measurement when 5×100 nm Parylene-N films were used (gray solid). Two out of five Parylene-N films are supported with Ni meshes, each of which has 86% transmission.

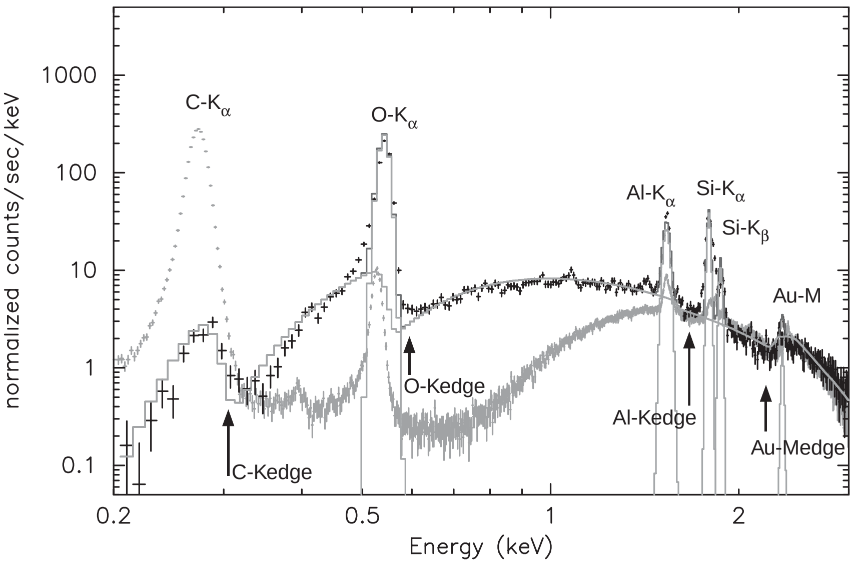

Figure 2.23: Gray or black crosses represent the obtained X-ray spectrum for Setup I (4 Toray-Lumirror filters) or II (4 Parylene-N filters). For Setup I / II, the high voltage of the X-ray generator: 3 kV / 3.5 kV, total count: 550 kcts / 6.4 kcts, integration time: 16 ks / 3.2 ks, energy resolution at O-K$_\alpha$: 23.5 eV / 26.1 eV, respectively. The best fit model convolved with the detector response is overlaid for the Setup II spectrum. The Au-M edge is due to the quantum efficiency jump of the gold X-ray absorber, and not the blocking filter origin.

material was calculated based on the spectral fit of the edge-depths observed in the detected X-ray continuum spectrum varying the contents of C, O, and Al in filters. The fit result was suggested 1.3 ± 0.3 μm build-up of ice for O. Some impurities, most of which are thought to be H_2O, have degraded the transmission apparently as shown in Fig. 2.24. The degradation was much more severe in Setup I which did not have the aperture cone structures (Fig. 2.21). The surfaces of the films were probably contaminated by impurities in vacuum when the cryostat was cooled down.

In this thesis, we examined the obtained X-ray spectrum with / without considering the impurities on the films of the X-ray window. There is no experimental results about the time growth of the impurity for the ADR system, and we could not investigate the transimission during the measurement in AIST. But gate-valves installed to the experimental setup of the port section were closed before cooling down to 0.1 K as same to our labo, and the degree of vacuum in the port section was greater than that of soft X-ray generator, we assume that any more extent of impurities were not acquired on the film than that in our labo.

It is important to answer preventing ice from being build-up on the blocking filters in future missions. Possible solutions are: (1) cutting down on aluminized-Mylar as thermal insulation in the cryostat, which is supposed to be the major source of the outgassing; (2) installing an absorbent material to help absorption of the outgassing around the blocking filters; (3) having a heater on each filter to keep a higher temperature on filters than surrounding materials.

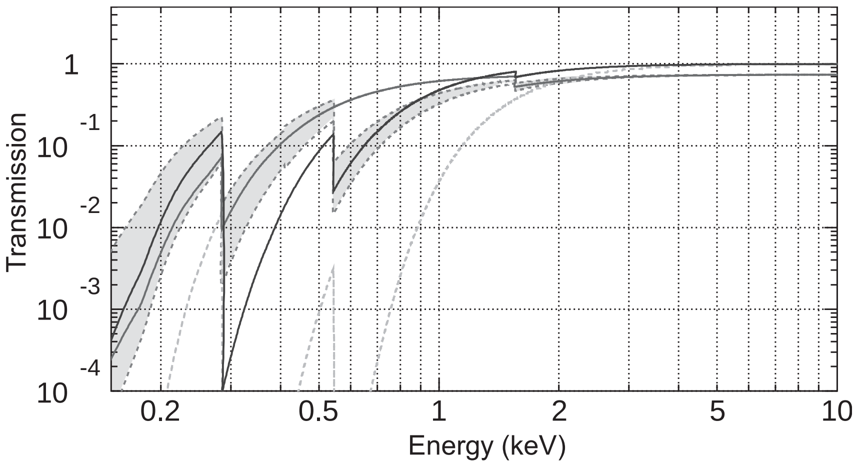

Figure 2.24: Expected transmission in Setup I (black solid lines) and that in Setup II (gray solid lines). 2 gray dotted lines represent the upper or lower limit of the allowed transmission range of the Parylene-N filters in Setup II respectively, which are calculated from the absorption depths around the element edge energies.

2.5 TPE-RX

TPE-RX is a large RFP device for nuclear fusion experiment at AIST. Fig. 2.25 shows the schmatic view of TPE-RX. The RFP is similar to a tokamak, in the sense that part of the confining magnetic field is generated by the plasma current itself. One of the advantage of the RFP plasma is that the confining magnetic field is relatively weak. The magnetic toroidal field at the plasma edge is usually 10 times smaller than the poloidal magnetic field, and its direction is opposite to that at the plasma center as shown in Fig. 2.26. The configuration of the RFP plasma is sustained by the dynamo effect due to magnetic fluctuation. The TPE-RX vacuum vessel (torus) is made of stainless steel SUS316L (Fe: 66%, Cr: 17%, Ni: 14%). Inside the torus, mushroom-type molybdenum limiters (98.5 mm ϕ) are attached for the purpose of protection against the strong heat load. The total number of limiters installed in the port section is 244.

The dianostic system of TPE-RX consists of measurement systems for (1) the equilibrium configuration, (2) the perturbing modes, and (3) the global confinement properties. In particular, it's important to compare the results of the TES calorimeter with the results of the other measuring system of global confinement properties, about electron and ion temperature, electron density, and impurity contents. Global confinement properties

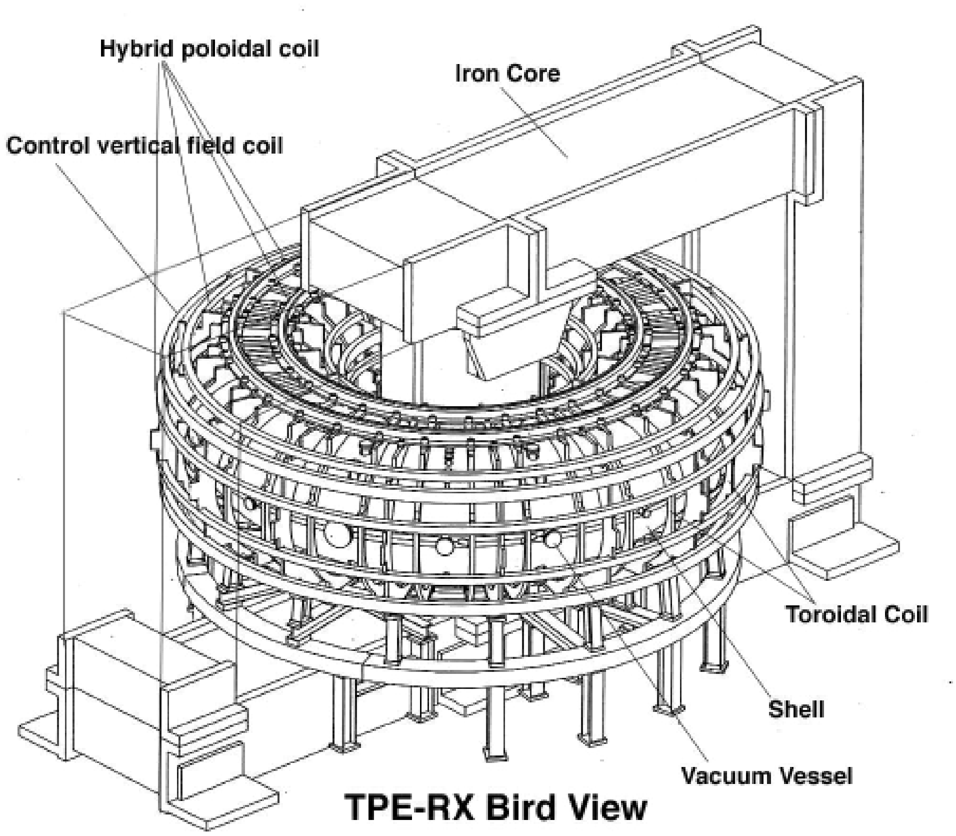

Figure 2.25: The view of the Toroidal Pinch Experiment RX — TPE-RX.

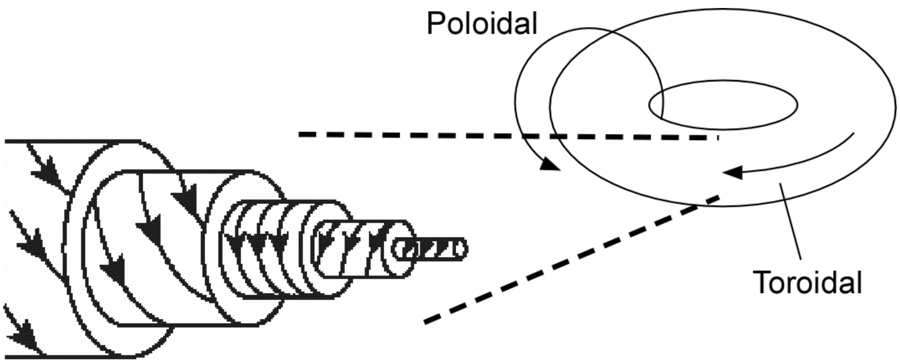

Figure 2.26: Construction drawing of reversed field pinch magnetic confinement. Magnetic field is along a toroidal field in a center, while poloidal field and reverses its sign in an edge.

are measured using a single-pulse single-point Thomson scattering system, a dual-chord CO_2 interferometer system, a single-chord neutral particle energy analyser (NPA), and a SiLi detector. The chord-averaged radiation loss power is measured using the bolometer system.

2.5.1 Ruby laser Thomson scattering system

The central electron temperature and density are measured using the Thomson scattering system. It is a single-point single-pulse system using a ruby laser of 694.3 nm with the maximum energy of 15 J (4–5 J is typically used). Since the electron density of TPE-RX

Table 2.3: Device parameter of SiLi detector

parameter	specification
detector active diameter	4 mm
detector thickness	4.48 mm
window filter	Be / 12.7 μm
	Au / 20 nm
	Si / 100 nm
added window filter	Be / 75 μm
E resolution (FWHM)	150 eV@5.9 keV *
amplifier time constant	$\sim$10 μs

* It's best energy resolution.

is relatively low ($\sim 5 \times 10^{18}$ m^{-3}), the laser energy should be high enough to give good photon statistics. There are ten wavelength channels from 618.5 nm (1.9 keV) to 688.4 nm (9 eV), and photomultiplier tubes (R955 Hamamatsu Photonics) are used for the detector. The initial experiment showed a Maxwellian distribution under the standard discharge conditions [35]. Typical electron temperature $T_{\rm el}$ measured by the system using a ruby laser is approximately 600 eV at the plasma current $I_{\rm p} = 220$ kA.

2.5.2 Interferometer

Line-averaged electron density is measured using the two-color, heterodyne, Michelson-type laser interferometer system with the CO_2 (10.6 μm) / He - Ne (3.39 μm) The system is developed under collaboration with the Consorzio RFX in Padua. The mechanical vibration is compensated by the conventional two-color method as well as the double-path method developed in Padua. There are two chords of the laer beam line through the plasma column at $r/a = 0$ and 0.69.

2.5.3 SiLi detector

The X-rays from TPE-RX have also been measured with a lithium drifted silicon detector (hereafter SiLi; ORTEC SLP-04170-P) at the same #15 port in October 2003. The SiLi detector has a sensitive diameter of 4 mm, detector thickness of 4.48 mm, and Be window of 12.7 μm thick. Another Be filter of 75 μm thick is also inserted to reduce pile-up events and constrain signals in hard energy band ($E \gtrsim 1.5$ keV). The detection efficiency of the SiLi detector is indicated by a dotted line in Fig. 2.22. The nominal energy resolution (FWHM) is 150 eV at 5.9 keV, but it is thought to be degraded to $\sim 250 - -300$ eV during the plasma shots.

2.5.4 Bolometer

Fast-response, thin-film bolometers were developed for the forerunner machines, and five bolometers of these are used in TPE-RX. The bolometer consists of a comb-shaped Ge thermistor 1 μm thick on the 2 μm thick SiO_2 insulating layer on 4 μm thick gold foil with a gold-thick coating to enhance the sensitivity in the visible light region. It has a high sensitivity of 2.5 mV/μJ and a fast response time of 10 μs.

Koguchi et al.(2004) [17] suggests that the radiation fraction to the input power is 15 % at $t = 30$ ms, which correspond to ~ 0.6 MW from the input power 4 MW at $Ip = 220$ kA.

Chapter 3

Experiment

3.1 Overview

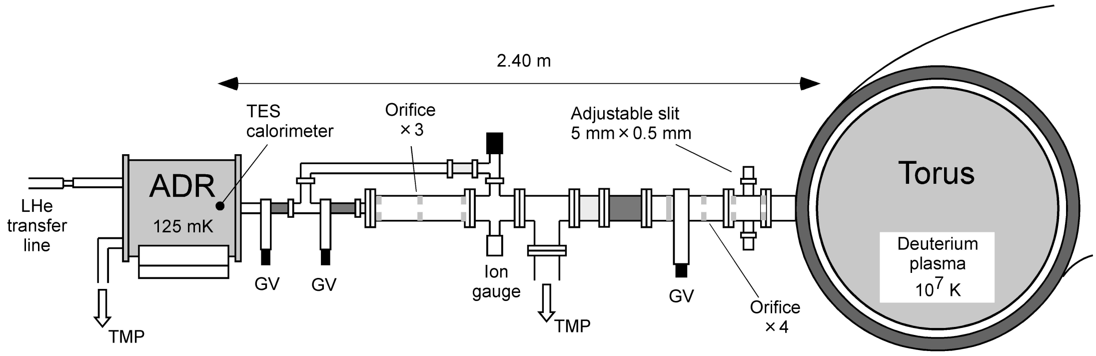

Figure 3.1: The experimental setup between the ADR and TPE-RX. An adjustable slit, turbo molecular pumps (TMP), three gate-valves (GV), three bellows joints (gray parts) and 7 orifices (light gray parts) are equipped in the system.

Figure 3.1 shows the experimental setup of the present measurement, which includes a torus of TPE-RX, a vacuum duct for connection, and the TES calorimeter installed in the ADR. There are sixteen port-sections in TPE-RX, and the port #15 was used in our experiment.

Table 3.1: Plasma shot numbers on each date

Date	Shot ID	Number
Aug. 16, 2004	39603 – 39660	58
Aug. 17, 2004	39661 – 39736	76
Aug. 18, 2004	39737 – 39839	103
Mar. 07, 2005	41793 – 41840	48
Mar. 08, 2005	41841 – 41870	30
Mar. 09, 2005	41871 – 41938	68
Mar. 10, 2005	41939 – 41987	49
Mar. 11, 2005	41988 – 42047	60
Mar. 12, 2005	42048 – 42119	72
Mar. 14, 2005	42120 – 42193	74

Table 3.2: Typical plasma parameters in this experiment

Parameter	Value
plasma current, $I_{\rm p}$	220 kA
electron density, $n_{\rm e}$	5×10^{18} m^{-3}
electron temperature, $T_{\rm el}$	600 eV
ion temperature, $T_{\rm i}$	300 eV
* poloidal beta, $\beta_{\rm p}$	0.07
† reversal parameter, F	-0.10 (at 30 ms)
‡ pinch parameter, Θ	1.5 (at 30 ms)

* $\beta_{\rm p} = 2\mu_0\langle p\rangle/B_{\rm p}^2(a)$, † $F = B_{\rm t}(a)/\langle B_{\rm t}\rangle$, ‡ $\Theta = B_{\rm p}(a)/\langle B_{\rm t}\rangle$.

See Sec. 3.4 for details.

The TES calorimeter detects X-ray photons originated in the deuterium plasma inside the torus, as well as fluorescent X-rays from the torus wall. Details of the experimental setup are described in Sec. 3.3. The measurement were done mainly two times. we had the first measurement on August 3-18, 2004, and we introduced the electromagnetic shield to reduce the noise during a plasma shot in second measurement on March 1-14, 2005. The plasma shot numbers are listed with respect to the date of the experiment in Table 3.1. We mainly show the result taken in the last three days of the August 2004 as first measurement, and total 7 days of the March 2005 as second measurement, when the TES calorimeter was operated in a good condition (see Sec. 5). Typical plasma parameters are listed in Table 3.2, and brief descriptions are given in Sec. 3.4.

3.2 Installation of TES calorimeter

Since both TES and SSA are superconductive devices, it is definitely essential to shield the magnetic field produced by the ADR magnet in order to prevent from trapping the field inside the device. We designed a detector box made of oxygen free copper (OFC) covered with superconducting Al/Pb and cryoperm shields as shown in Fig. 3.2. Photographs inside the box and front-end assembly are presented in Fig. 3.3. The TES calorimeter is mounted at the center of an OFC table inside the box, and the temperature of the table is monitored with two Ruthenium-Oxide (RuOx) thermometers. The calorimeter is surrounded by Al/Pb shields, each of which has 2 mm ϕ or 4 mm ϕ hole for the X-ray detection and two 2.1 mm ϕ screw holes to provide a thermal link with the OFC table. The box itself is shielded by μ-metal cryoperm, which also has a 4 mm ϕ hole in the direction of the X-ray incidence. Since TES is most seriously affected by the vertical magnetic field, thermal link between the box and the saltpill is provided by an OFC arm which is attached to the side walls of the detector box using two M3 brass screws. Therefore, the direction from the detector to the saltpill is completely covered with the shielding materials.

Electric wiring for the TES calorimeter and RuOx thermometers are both connected using electric feed-throughs installed in the side walls of the box. The SSA is mounted at the bottom of the 1.7 K He tank, and is triply shielded by a Nb box, a cryoperm box, and a permalloy plate, from inside to outside (in Sec. 2.1.6). The shunt resistor ($R_{\rm S}$ in Fig. 2.2) and the bias resistor ($R_{\rm b}$) are also fixed on the He tank. Superconducting NbTi in twisted pairs is used as the wiring material among the TES calorimeter, SSA, and both resistors.

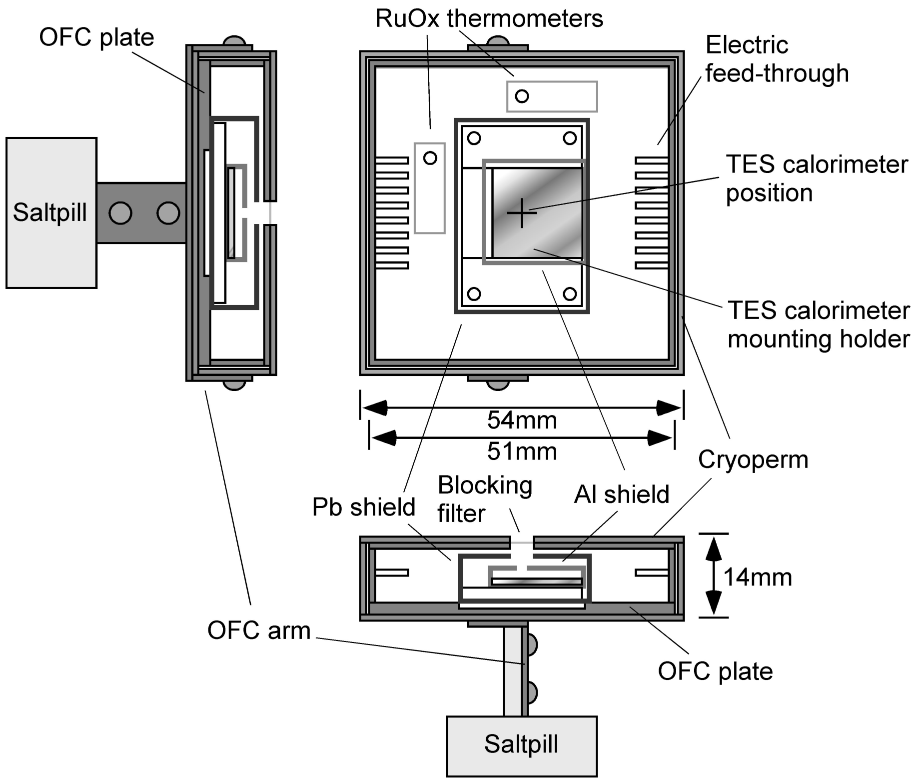

Figure 3.2: The detector box design in this experiment. The TES calorimeter is mounted at the center and the temperature of the box is measured with two thermometers at the side of the detector. TES calorimeter is surrounded by Al/Pb shield, and the whole box is shielded by a μ-metal cryoperm shield box.

In order to calibrate the detector gain continuously, a ^{55}Fe radioactive source is equipped above the 50 K filter without interfering the line of X-ray incidence as indicated by Fig. 2.21. The 5.9 keV (Mn-Kα) X-rays always shine the detector with a counting rate about 0.1 c s^{-1}, which is high enough for monitoring the gain, while these X-rays cause negligible effect during the plasma shots.

3.3 Connection between ADR and TPE-RX

The ADR was horizontally connected to #15 port section of TPE-RX with a vacuum duct as already shown in Fig. 3.1. The distance from the inner vessel of the torus to the detector surface is 2.40 m. Six stainless orifices (32 mm ϕ hole, 3 mm thick) and one aluminum orifice (10 mm ϕ hole, 0.5 mm thick) are placed to block stray X-rays caused by reflection inside the duct, as shown in Fig. 3.4. An adjustable slit is placed at the port section to regulate the X-ray flux, which is fixed to 5 mm width and 0.5 mm height throughout the measurement. Light axis of the vacuum duct between TPE-RX and the ADR dewar is calibrated with a laser beam. The turbo molecular pump (TMP) connected to the ADR is stopped during the plasma measurements, while the vacuum duct is kept at $\sim 5 \times 10^{-8}$ Torr by another TMP connected to the duct (middle of Fig. 3.1). Three gate-valves (GV) are equipped to the vacuum duct. A rotary pump (ULVAC VD401, 670 ℓ/min) is connected to the L-He transfer line to keep the pumped L-He bath at 1.7 K during the measurement. All the pumps and TPE-RX are electrically insulated from the ADR system in order to avoid the ground loops in which large current is induced during the plasma operation.

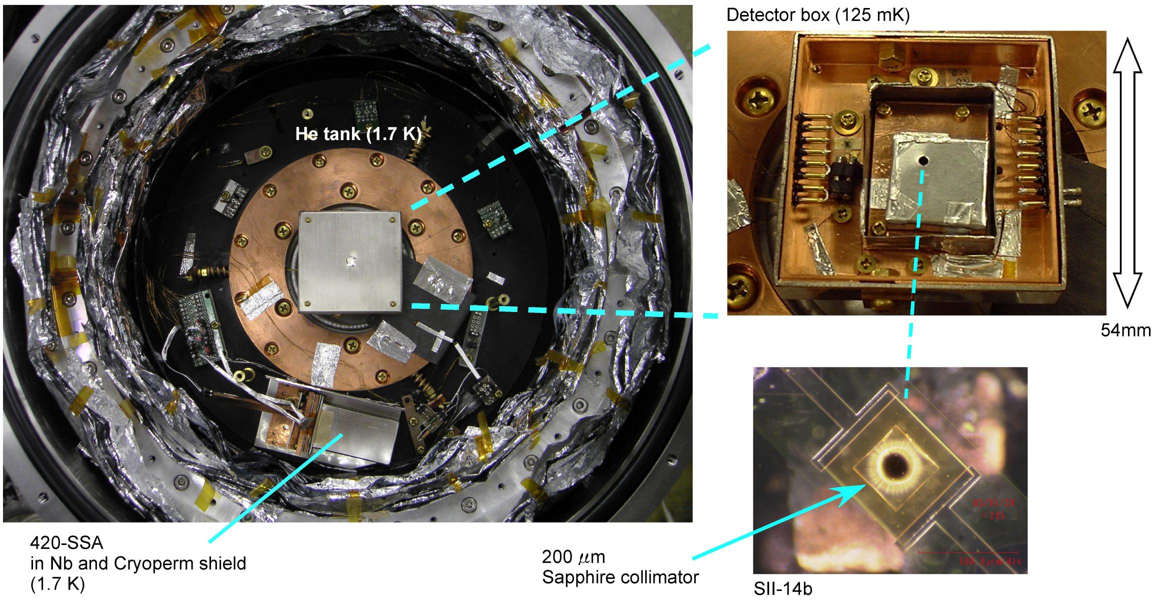

Figure 3.3: Experimental setup of the detector box and front-end assembly. A collimator is attached to the device. The device is mounted at the center of the OFC detector box and shielded by Al/Pb box. The window size for the cryoperm shield box is 4 mm ϕ. The box is installed along the central axis of the cryostat. The calorimeter signal is picked up by the SSA mounted at the bottom of the 1.7 K L-He bath.

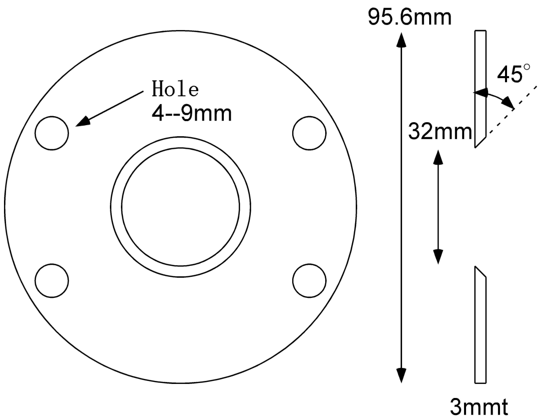

Figure 3.4: The design of the orifice installed in the port section.

3.4 Plasma parameter

The experimental condition of TPE-RX is controlled by changing voltages of the capacitor banks, such that the plasma current, I_{p}, the reversal parameter, $F = B_{\mathrm{t}}(a)/\langle B_{\mathrm{t}}\rangle$, and the pinch parameter, $\Theta = B_{\mathrm{p}}(a)/\langle B_{\mathrm{t}}\rangle$, take the values shown in Table 3.2, during the plasma current flat-top phase ($t \sim 30$ ms) for the discharges. Here, $B_{\mathrm{t}}(a)$ is the toroidal field at the plasma edge, $\langle B_{\mathrm{t}}\rangle$ is the volume-averaged toroidal flux, and $B_{\mathrm{p}}(a)$ is the poloidal field at the plasma surface. Note that poloidal beta, β_{p} is defined as $\beta_{\mathrm{p}} = 2\mu_0\langle p\rangle/B_{\mathrm{p}}^2(a)$, where μ_0 is the vacuum permeability, $\langle p\rangle$ is the volume averaged plasma pressure.

The first measurement was conducted on 16–18 August 2004 at AIST, and 210 plasma shots were obtained with sufficient quality for analysis. Each shot was basically generated in every 5 min interval, which is determined by the TPE-RX specifications. Plasma shot numbers on each date are given in Table 3.1. The plasma current was set to $I_{\mathrm{p}} = 220$ kA during the flat-top phase as indicated by gray lines in Fig. 4.1. The deuterium gas pressure was kept constant at 0.4–0.5 mTorr during the discharge. Typical plasma parameters in

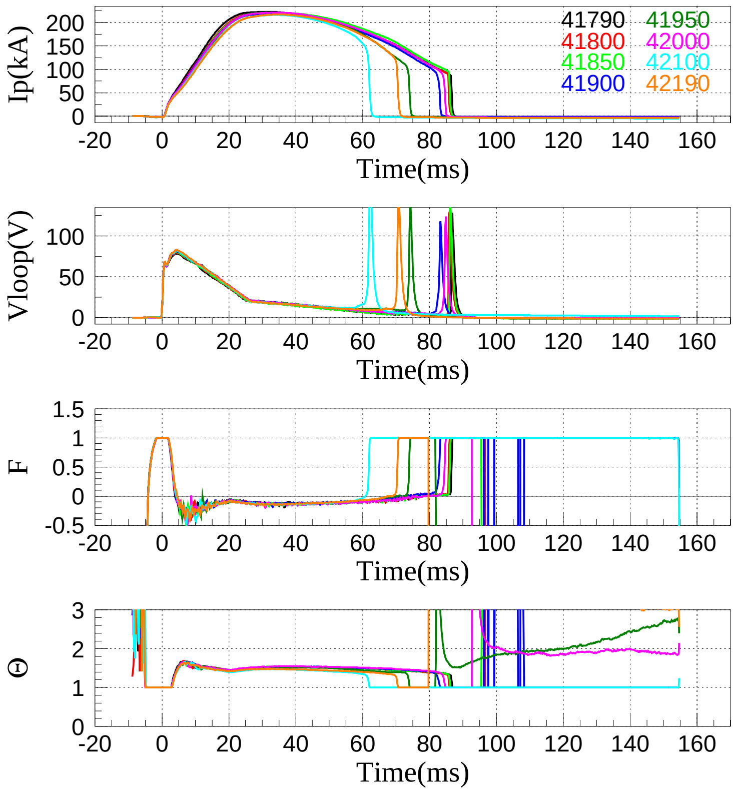

Figure 3.5: Examples for plasma parameters in each shot in second measurement.

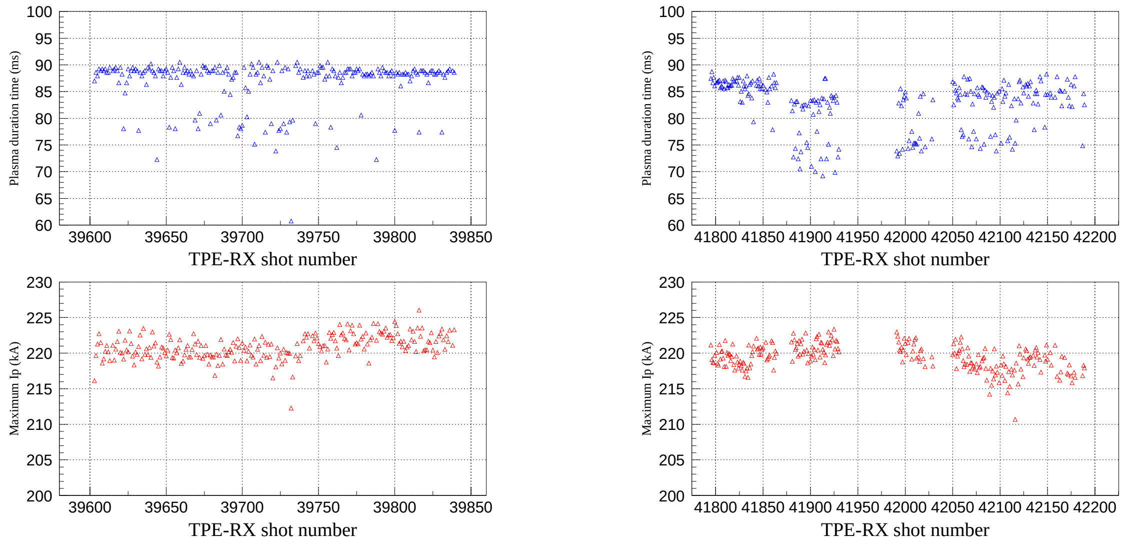

Figure 3.6: The plasma duration time and maximum plasma current I_p history. left : in first measurement. The mean I_p is 220.11 kA and rms is 1.49 kA. right : in second measurement. The mean I_p is 219.43 kA and rms is 1.80 kA.

this condition are listed in Table 3.2. The electron density, $n_{el} = 5 \times 10^{18}$ m^{-3}, electron temperature, $T_{el} \sim 600$ eV, and ion temperature, $T_i \sim 300$ eV, are measured from other diagnostics system of TPE-RX [35].

Fig. 3.5 shows typical results of plasma parameters in second measurement. The reproducible results were obtained for I_p, loop voltage along the circle of the major radius V_{loop}, the reversal parameter F, and the pinch parameter Θ, while the plasma duration

Table 3.3: Typical operating parameters of TES calorimeter, SII14b in first experiment

PARAMETER	VALUE
temperature of detector box, T_s	125 mK
TES resistance, R	52 mΩ
bias voltage, V	2.4 μV
TES current, I	45 μA
signal time constant, $\tau_{\rm eff}$	200 μs
shunt resistance, R_s	10 mΩ
parasitic resistance, R_p	5.9 mΩ

time had some degree of dispersion. We assumed that plasma in the time duration of 35–70 ms, in which we accumulate the X-ray signals for the energy spectrum, was almost same condition between each shot. But we extracted the X-ray signals from shots with less than 70 ms plasma duration time. On the other hand, results of plasma parameters were very stably obtained in first measurement,

Fig. 3.6 shows the history of the plasma duration time and maximum plasma current I_p. The rms of I_p has only less than 1 % in both measurements, physical properies of TPE-RX are sufficiently reproducible. We note that the history shown in Fig. 3.6 includes only shot numbers in which we obtained X-ray signals for the spectral analysis, not the all shot numbers (especially there are some blanks in second measurement), so that the figure does not correctly represent the statistical properties of TPE-RX.

3.5 Operating condition of TES calorimeter

3.5.1 first experiment — 3 – 18 Aug, 2004

We used the TES calorimeter SII14b in first measurement, on 3 – 18 Aug, 2004. The ADR was cooled down to $T_s = 125$ mK and the TES calorimeter was operated at $R = 58$ mΩ with the bias voltage of $V = 2.4\ \mu$V. Typical parameters of the TES calorimeter at this operating point is summarized in Table 3.3. Fig. 3.7 shows electrical and thermal properties of the TES in AIST and in TMU. The results are used with the ADR system, different from that in Fig. 2.7. In fact, the operating temperature and resistance are slightly higher than the optimal point, because we encountered a significant increase of low-frequency noise when the TES current was increased. This is due presumably to deterioration of electric contacts of superconducting NbTi wiring which does not stick well to solder, resulted from the vibration shock during the transportation from TMU to AIST. As an evidence, the shunt resistance R_s and the parasitic resistance R_p increased by about a few mΩ larger than the normal values, 4 mΩ and < 1 mΩ, respectively.

Based on the analysis of the calibration isotope data, it is demonstrated that the energy resolution (FWHM) was 19.2 ± 0.8 eV at 5.9 keV and 14.6 ± 0.3 eV at 0 keV in quiescence, i.e., 5 min interval between each plasma shot. However, the energy resolution was degraded to ~ 50 eV during the plasma shots, due mainly to a noise increase probably caused by the fluctuation of the strong magnetic field generated by the plasma current. It is also notable that the counting rate during the plasma shot is relatively high ($\gtrsim 600$ c s^{-1}) as compared with the signal time constant of $\tau_{\rm eff} = 200\ \mu$s, which is also significantly degraded from the optimal value of $\sim 75\ \mu$s. The degradation of the signal time constant is partly due to the non-optimal operating condition and also to the trapping of a magnetic field at the TES.

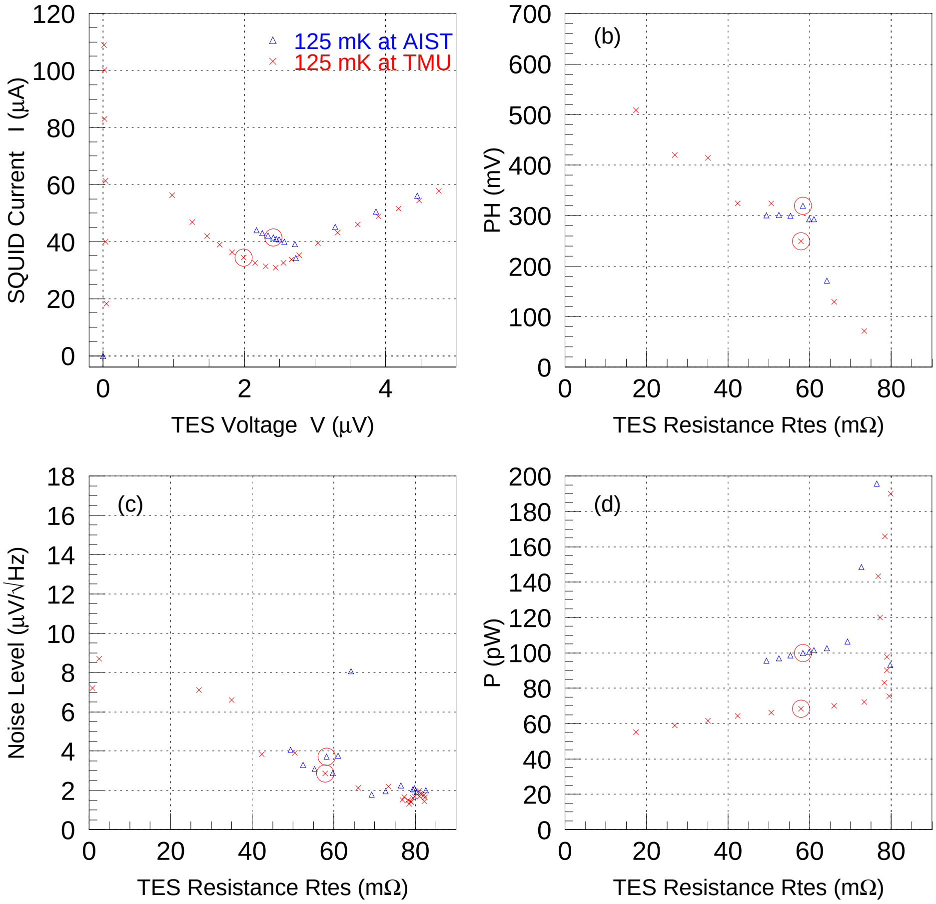

Figure 3.7: (a) Relation between TES current $I_{\rm sq}$ and TES voltage $V_{\rm tes}$ (IV curve). (b) Operating point dependences of the pulse height PH (mV). (c) Operating point dependences of noise level at 4 kHz. (d) Operating point dependences of Joule power calcurated from the IV curve. Red crosses represent the results at TMU after the plasma measurement in AIST.

Table 3.4: Typical operating parameters of TES calorimeter, SII110 in second experiment

Parameter	Value
temperature of detector box, $T_{\rm s}$	100 mK
TES resistance, R	109–117 mΩ
bias voltage, V	3.9–4.1 μV
TES current, I	34.7–35.5 μA
signal time constant, $\tau_{\rm eff}$	222–247 μs
shunt resistance, $R_{\rm s}$	12 mΩ
parasitic resistance, $R_{\rm p}$	$<$ 1.1 mΩ

3.5.2 second experiment — 7 – 14 Mar, 2005

In second measurement, we used the TES calorimeter SII110 on 1 – 14 Mar, 2005. Typical parameters of the TES calorimeter at this operating point is summarized in Table 3.3, and Fig. 3.7 shows electrical and thermal properties of the TES in AIST and in TMU. The results are also measured with the ADR system. There also was somewhat deterioration

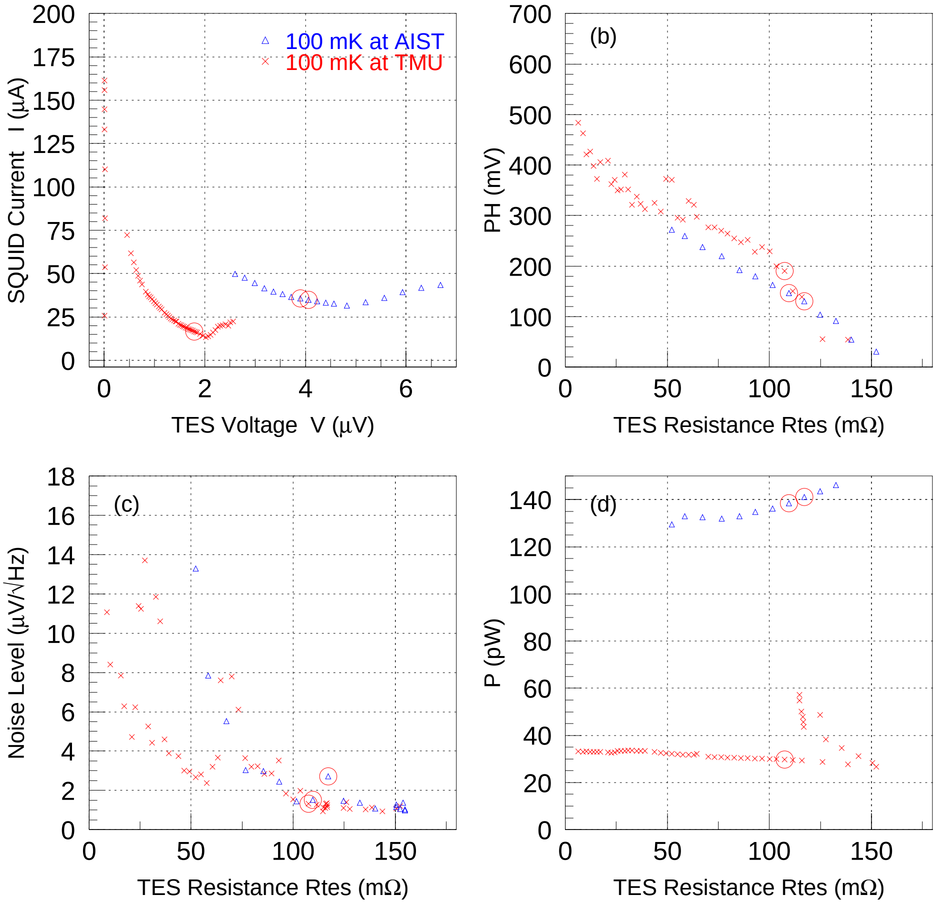

Figure 3.8: (a) Relation between TES current $I_{\rm sq}$ and TES voltage $V_{\rm tes}$ (IV curve). (b) Operating point dependences of the pulse height PH (mV). (c) Operating point dependences of noise level at 4 kHz. (d) Operating point dependences of Joule power calcurated from the IV curve. Red crosses represent the results at TMU after the plasma measurement in AIST.

of electric contacts of shunt resistor ($4 \rightarrow 12$ mΩ), which caused the lower pulse height compared to that in TMU. From the calibration isotope data, it is demonstrated that the energy resolution (FWHM) was 28 – 55 eV at 5.9 keV and 15 – 20 eV at 0 keV in quiescence, i.e., 5 min interval between each plasma shot. During the plasma shots, the energy resolution was degraded to $\sim$ 50 eV during the plasma shots. The signal time constant was 222–247 μs, which was larger than that in TMU ($\tau_{\rm eff} \sim 168$ μs). In addition, we installed higher transmission X-ray windows using thin Parylene-N films, so that the adjustable slit was fixed to 5 mm width and 0.005 mm height throughout the measurement. As a result, the counting rate during the plasma shot was $\sim$ 350 c s^{-1}, which was about a half of that in the first experiment.

3.5.3 Electromagnetic shield

In a typical waveform during a plasma generation of TPE-RX, a DC level fluctuation which was very similar to the derivative of plasma current was measured in first experiment (shown in Fig. 4.1). At a few msec before the plasma shot, it's dominant for the measured waveform of the TES to be affected by the toroidal magnetic field of TPE-RX, while it was dominantly affected by the poloidal field during a shot. The maximum toroidal field

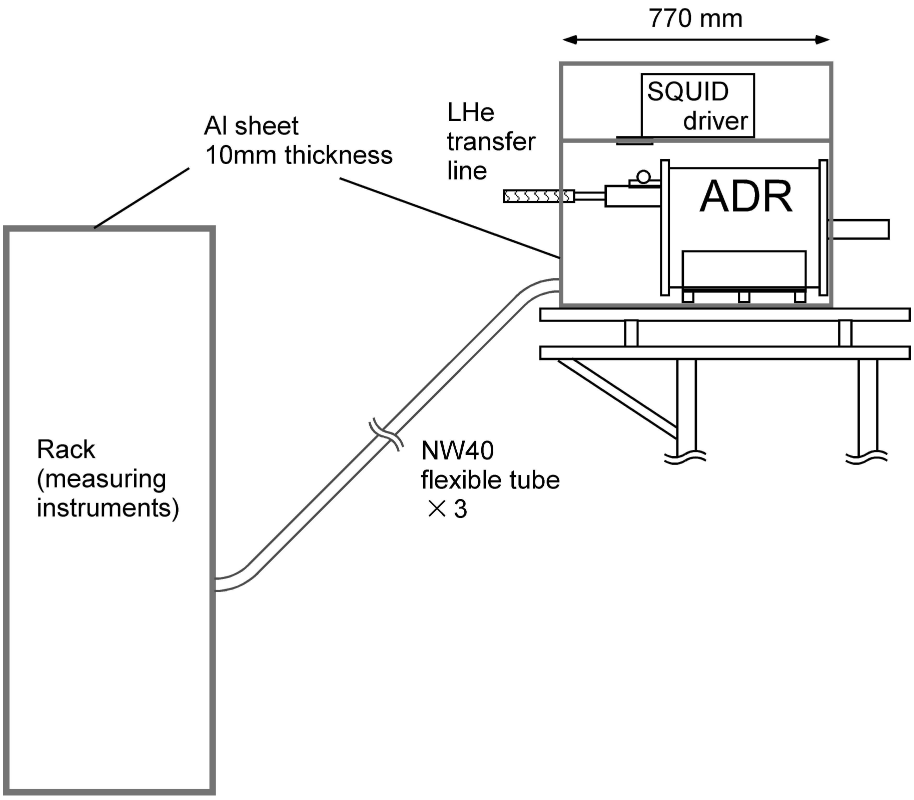

Figure 3.9: Assembly of Al electromagnetic shield. 2 of 3 stainless-steel flexible tube connected between the shield around the ADR and that introducing measuring instruments were electrically breaked.

around the refrigerator is assumed to be < 10 Gauss, and the maximum poloidal field is less than 100 Gauss. To reduce the fluctuation, we introduced the electromagnetic shield made of aluminum alloy sheets around the ADR as well as our measuring instruments in second measurement, as shown in Fig. 3.9. The time constant of electromagnetic field to permiate into a shield is

$$B_{\rm in} = B_{\rm out}(1 - \exp(-t/\tau_{\rm B})), \qquad \tau_{\rm B} = 2\pi\mu_0\sigma D^2 \sim 2\pi\mu_0\sigma D x \tag{3.1}$$

where $B_{\rm in}$ is the field in the shield with the thickness D, $B_{\rm out}$ is the field outside of the shield, x is the typical length between the TES and the shield, μ_0 is magnetic permeability of vacuum, and σ is the conductance of the shield. We employed 10 mm thickness sheet and $\tau_{\rm B}$ is $\sim 6.3\times10^{-3}$ sec for $x = 20$ cm. More than 160 Hz field is expected to be cut off. We also introduced the shield around the commercial SQUID driver which was put on the ADR. Electric wires between the ADR, the SQUID driver and measuring instruments were connected through the NW40 stainless-steel flexible tube.

3.5.4 Critical current of the TES calorimeter

An energy resolution of a TES calorimeter is degraded when it traps a magnetic field, which causes a smaller sensitivity α and smaller pulse height of X-ray signals. Fig. 3.10 shows the measured value of the critical current at various temperature in TMU and AIST for SII14b with the ADR. According to the Ginzburg-Landau theory [33], the critical current at temperature T of a thin wire or film is given by,

$$I_{\rm c} = I_{\rm c0} \times \left(1 - \frac{T}{T_{\rm c0}}\right)^{1.5} \tag{3.2}$$

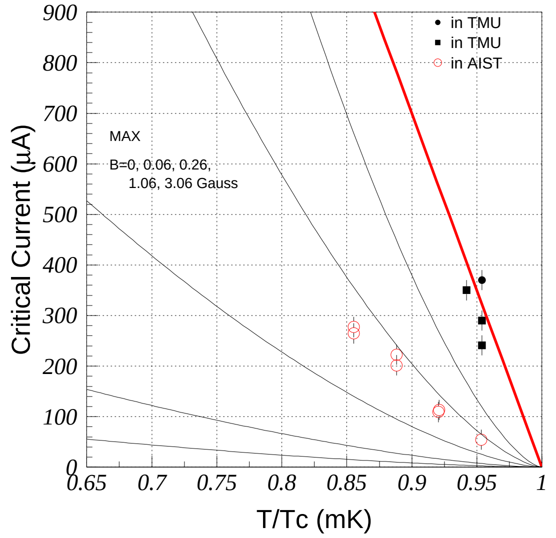

Figure 3.10: Relation between critical current and temperature of the TES calorimeter SII14b normalized with transition temperature. Circles are measured in sideway configuration, and squares are in vertical. Thin solid lines show the critical current lines with each amplitude of residual magnetic field, 0, 0.06, 0.26, 1.06, 3.06 Gauss, respectively. Thick solid lines show the maximum critical current lines. The transition temperature of SII14b is 152 mK.

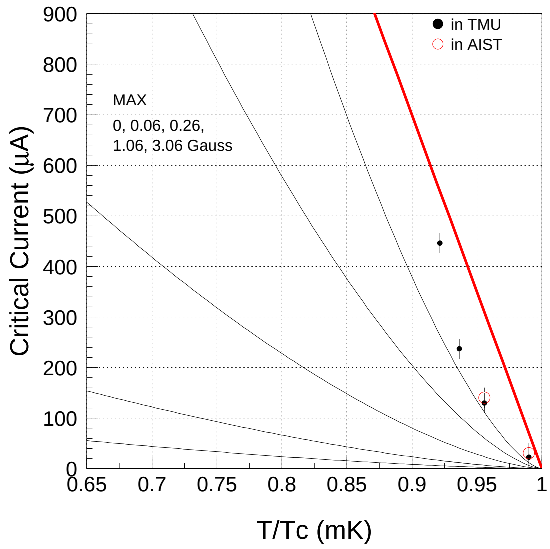

Figure 3.11: Relation between critical current and temperature of the TES calorimeter SII110 normalized with transition temperature. Solid lines represent the same lines for SII14b. The transition temperature of SII110 is 147 mK.

The critical current I_c was precisely measured in various amplitude of vertical magnetic fields, $B = 0, 0.06, 0.26, 1.06, 3.06$ Gauss by using the dilution refrigerator at TMU (thin solid lines in Fig. 3.10). But larger critical current was measured when the Pb magnetic shield was installed around < 1.6 K devices in the dilution refrigerator, which was assumed to be the maximum current (thick solid lines in Fig. 3.10). The measurement derives the critical current at zero temperature and at $B = 0$, $I_{\mathrm{c}0} = 12$ mA, and the critical temperature at zero current and at $B = 0$, $T_{\mathrm{c}0} = 152$ mK. We also assumed the empirical formula in the measurement,

$$I_\mathrm{c} = I_{\mathrm{c}0} / \left(1 + \frac{B}{B_0}\right) \tag{3.3}$$

B_0 is assumed to be the normalized magnetic field. From Eq. 3.2 and 3.3, we obtain,

$$I_\mathrm{c} = I_0 \times \left(1 - \frac{T}{T_{\mathrm{c}0}}\right)^{1.5} / \left(1 + \frac{B}{B_0}\right) \tag{3.4}$$

In Fig. 3.10, we overplot results of the critical current with the ADR. The TES calorimeter was trapped about 0.3 Gauss in AIST, which caused by fields of TPE-RX components around the ADR, while it was not trapped in sideway configuration as well as in vertical in TMU.

Fig. 3.11 also shows the measured value of the critical current for SII110. It provides almost same results between in TMU and AIST, which indicated that thin Al sheet at the backside of the detector has effectively prevented the trap of the magnetic field in AIST.

3.6 Data acquisition

The SSA connected to the TES calorimeter (Fig. 2.2) is operated with a commercial SQUID driver produced by SIINT, and the small change of the TES current ($\sim$ a few μA) is converted to the voltage output with a conversion factor of 50 kV A^{-1}. The voltage output is analyzed by a digital oscilloscope (Yokogawa DL708E) which has a long 4 MW memory and 2 GB hard disk drive (HDD) inside. All the waveform during every plasma shot is sampled with an ADC (2 MHz sample rate, 13 bit resolution) and stored into the local HDD. The waveform acquisition is triggered by the plasma current generation ($t = 0$), and waveforms between -60 ms $\leq t \leq$ 140 ms are saved. These raw waveforms are then delivered to the dedicated off-line analysis described in § 4. An optical fiber is used for the trigger line to avoid induction current caused by the plasma operation. The X-ray signals from the calibration isotope are separately stored by another identical oscilloscope with self-triggered pulse-by-pulse scheme.

The resistance of the RuOx thermometer on the detector box is measured by an AC resistance bridge (Cryocon Model 62), and is continuously monitored by a notebook PC in every one second. The notebook PC then determines the ADR magnet current based on the improved PID method (§ 2.3), and controls the current commanding to a source meter (Keithley 2400). The source meter can control the current in 5 μA step up to 100 mA. Such a precision is required to control the ADR temperature better than the accuracy 10 μK r.m.s., while the maximum current of 100 mA is by far not sufficient for the demagnetization process. We therefore employ another current source (KENWOOD PDS36-10) in parallel during the demagnetization phase.

3.7 Operation cycle

Since L-He must be refilled in every 14 hours, the experiment was basically conducted in one-day cycle. In early morning, pumping from the L-He transfer line is stopped, and the L-He tank volume is very slowly ($\sim$ 1 hour) purged by He gas up to 1 atm. About 9 ℓ of the L-He is refilled horizontally from the transfer line, and is pumped down to 1.7 K again ($\sim$ 1 hour). During this procedure, we must be careful to preserve the superconduction of the Nb shield for the SSA, because it allows penetration of the magnetic flux from surrounding materials, which are slightly magnetized during the demagnetization phase. Once this penetration happens, the magnetic field is trapped in the SSA and this trapping is not cleaned away until the whole system is warmed up to room temperature.

After the pumping down, the detector box is cooled down by the adiabatic demagnetization ($\sim$ 2 hour). The starting temperature and magnetic flux density of the demagnetization was typically 2.7 K and 2.8 T with the magnet current of 5.5 A, and the lowest temperature after the demagnetization was $\sim$ 85 mK at AIST. The efficiency of the magnetic cooling was by about 10% worse at AIST than that at TMU, because there was assumed to be worse of the degree of vacuum. It is important to bias the TES calorimeter before cooling down, otherwise we have to raise the temperature of the detector box up to the transition temperature of the TES (151 mK), which shortens the time of tight temperature control by gradually decreasing the magnet current. At this point, we can measure the X-rays from TPE-RX, and the measuring time is usually limited by the holding time of the L-He ($\sim$ 8 hours are left). After the measurement, we have to refill the L-He and pump it down in the same procedure described above. We cannot omit the last pumping down process because L-He evaporates much faster without this procedure in the sideway configuration.

Chapter 4

Data Analysis and Signal Reduction

X-ray calorimeters have very small fundamental energy fluctuation and potentially can achieve good spectral energy resolution, in principle. However, an actual signal shape is affected by the noise, and a simple signal peak is not a good estimate of the pulse height. We have to apply an optimal filter described below to obtain the minimized error. Furthermore, we acquired the X-ray signals by triggering the plasma current generation TPE-RX, so that the technique of signal extraction from the waveform is required. In this section, a typical waveform, the noise behavior during a plasma shot, the method of the data reduction, and the derived energy resolution of the TES calorimeter are presented.

4.1 Waveform during a plasma generation

4.1.1 first experiment

Typical waveforms of the TES calorimeter output in the first mesurement are presented in Fig. 4.1 obtained by the digital oscilloscope during plasma shots. The waveform acquisition is triggered by the plasma current generation in TPE-RX at $t = 0$ of the x-axis. When the GV is open, X-ray signals are clearly detected around 20–80 ms, while there are none when closed. In general, X-ray signals indicate a shape of exponential decay $\propto \exp(-t/\tau_{\rm eff})$, with $\tau_{\rm eff} \simeq 200$ μs throughout our measurement, as seen in Fig. 4.1 (c).

The DC level of the TES output is affected by the strong magnetic field and probably by mechanical vibration around the detector, too, at a lower level. Our system looks susceptible to both the toroidal magnet field along the torus and the poloidal field across the torus. The latter is mainly generated by the plasma current $I_{\rm p}$ during the shot where $I_{\rm p} > 0$. The toroidal coil current is applied at 5 ms before the plasma current generation, where we can see a sharp jump in the TES output. On the other hand, the poloidal field is dominant during the shot and the global structure of the TES output is similar to the time derivative of the plasma current, $(dI_{\rm p}/dt)$, which is equal to the plasma loop voltage as shown in Fig. 4.3. To produce an energy spectrum, we accumulate the X-ray signals in time duration of 35–70 ms corresponding to the flat-top of $I_{\rm p}$ (see also Sec. 5.2). Because shot-by-shot difference in the RFP plasma characteristics is negligible, X-ray signals in all shots are combined together for later analysis.

4.1.2 second experiment

Fig. 4.2 shows the typical waveform of the TES output (GV was opened) in the second measurement. Though there was also a DC level fluctuation during a plasma shot, while it could reduce a high frequency noise for the electromagnetic shield. Most of signals were

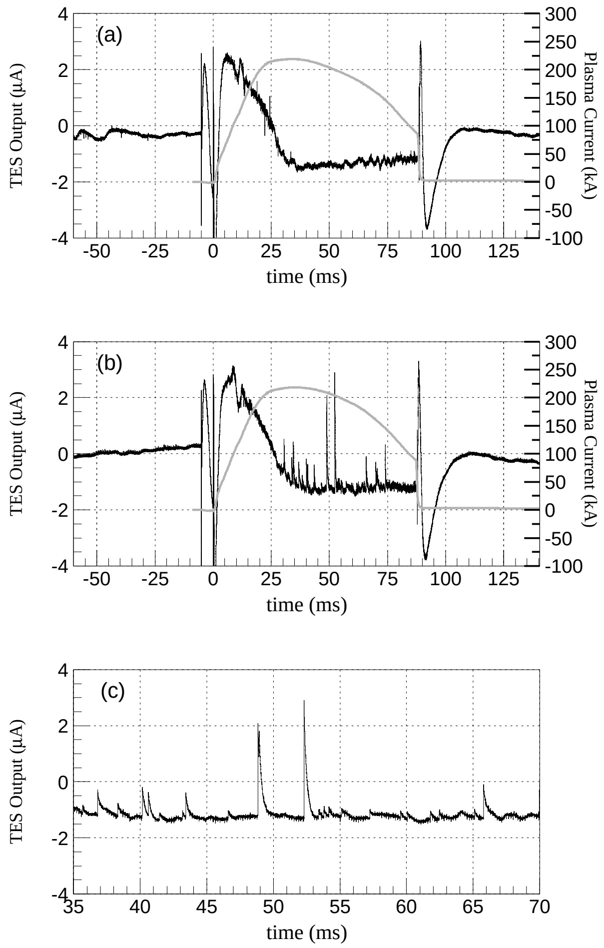

Figure 4.1: Typical waveforms of the oscilloscope (black) and the plasma current (gray) during plasma shots. (a) GV close. (b) GV open. (c) Zoom up for GV open between 35 ms $< t <$ 70 ms where the X-ray signal extraction was conducted.

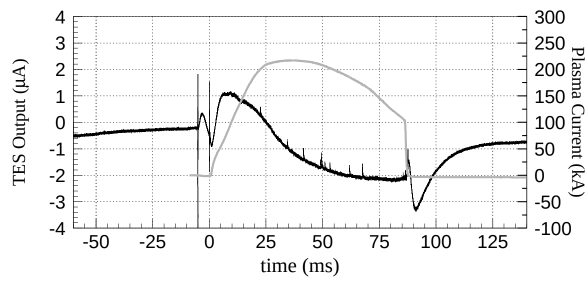

Figure 4.2: Typical waveform of the oscilloscope (black) and the plasma current (gray) during a plasma shot in second measurement.

very soft X-ray ($<$ 1 keV) because of the improvement of the transmission of the X-ray window (Sec. 2.4).

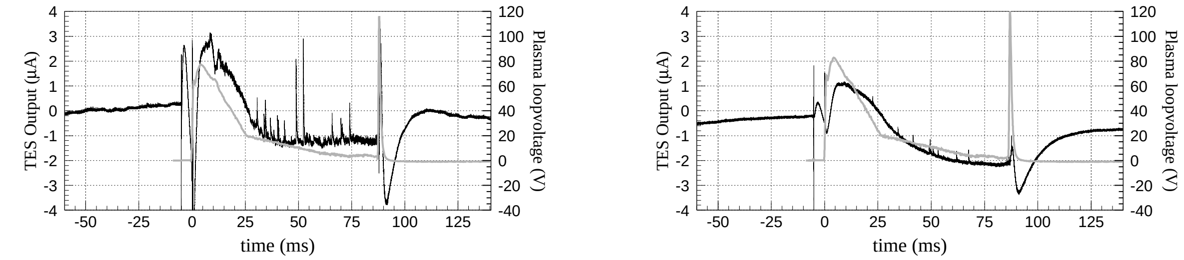

Figure 4.3: Typical waveform of the oscilloscope (black) and the plasma loop voltage (gray) during a plasma shot in first measurement (top) and in second measurement (bottom).

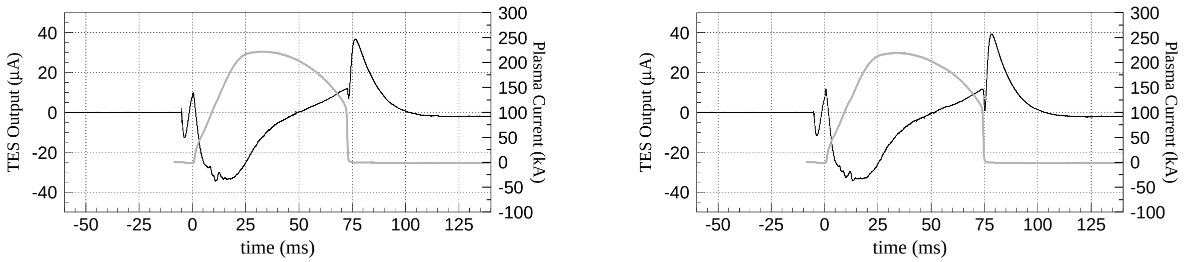

Figure 4.4: The waveform of the TES output in superconducting state. left: GV open, right: GV close, and electric circuitry of the TES was closed in the ADR.

4.2 Analysis of DC level fluctuation and noise

4.2.1 DC level fluctuation

In the second measurement, we obtained the TES output until TES calorimeter was normal or superconducting state during a plasma shot, which were shown in Fig. 4.4, 4.5. The amplitude of the DC level fluctuation was apparently increased in the superconducting state, while it's smaller in the normal state. In addition, the behavior of the fluctuation in both states were inverse to the fluctuation in transition edge (operating state). It's also suggested that the DC level fluctuation was dominantly affected by the induction current from magnetic field generated by TPE-RX, rather than a mechanical vibration or thermal radiation for the plasma.

If an induction current runs to increase I_{b}, the differrent output is measured for the state of the TES, because of the different R_{TES}. However, under the prediction, the estimated maximum induction current in normal state of the TES by using Eq. 2.28 was 70.0 μA, while the current in superconducting state was 37.8 μA, which was twice smaller than the former. Furthermore, it cannot explain the feature that the amplitude of the

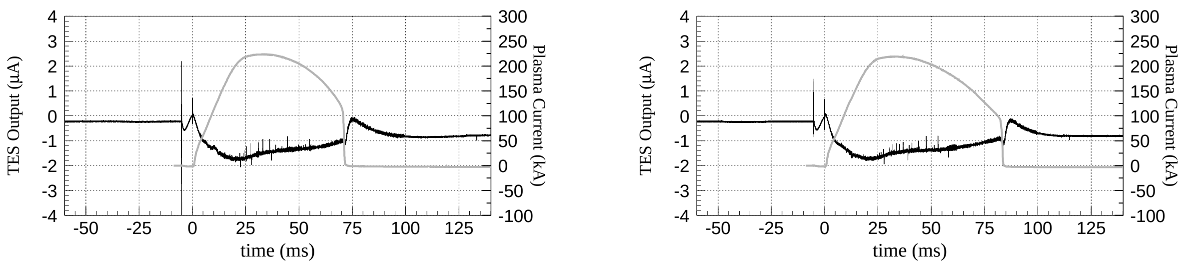

Figure 4.5: The waveform of the TES output in normal state. left: GV open, right: GV close, and electric circuitry of the TES was closed in the ADR.

fluctuation when electric circuitry of the TES was closed in the ADR is almost the same as that when not close in both superconducting and normal states (Fig. 4.4 and 4.5), because 5 kΩ of 15 kΩ bias resistance R_b in the circuitry is installed out side of the ADR.

If the parallel circuit which consists of R_s, R_{TES} and the input coil of the SQUID is only considerd, the estimated maximum induction voltage V_{in} is

$$V_{in} = (R_{TES} + R_s + R_p) \times I_{sq} \tag{4.1}$$

From Eq. 4.1, V_{in} in normal state is $\sim$ 286 nV, which is consistent with that in superconducting state, $\sim$ 290 nV. This picture can easily explain the same amplitude problem descrived above. An induction voltage was also expected to occur in bias line, However, the induction current was sufficiently small because we measured the current by using the SQUID amplifier and R_b was very large compared to R_s and R_{TES}. Basically, we installed the electric wires of the TES as twist wires, but it can be easily considerd to generate such a small induction in the circuitry.

Assuming that the total cross section of the loop is ~ 1 cm^{-2}, the intruding magnetic field is calculated to be less than 1 Gauss, which is an order of 1/100 of the generated magnetic field at the distance of the ADR from the torus.

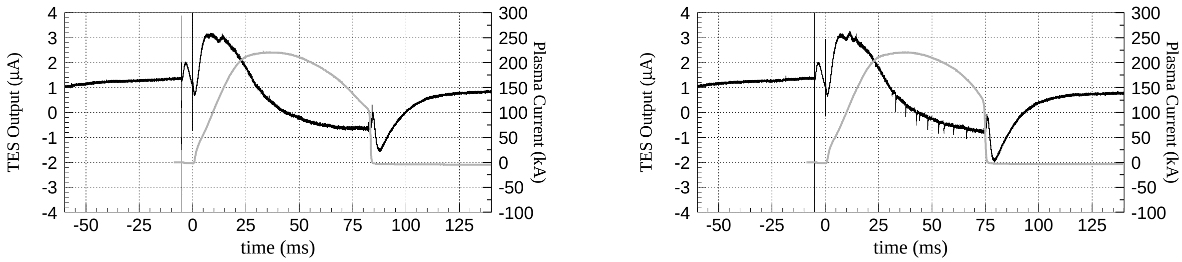

Figure 4.6: The waveform of the TES output during the opposite bias, $I = -35.5$ μA. left: GV close, right: GV open, inverse X-ray signals were obtained.

We also obtained the waveforms when the TES current was -35.5 μA, as shown in Fig. 4.6. The whole fluctuations in both setup (GV open and closed) were almost the same as that at normal current, while palarity of X-ray signals were negative. If the fluctuations were caused by the temperature rise of the TES, these signals would also be negative. Over all, it apparently indicates that the induction current was generated in the ADR, not in the power unit nor through electric lines in room temperature.

4.2.2 Fluctuation of the TES operating point

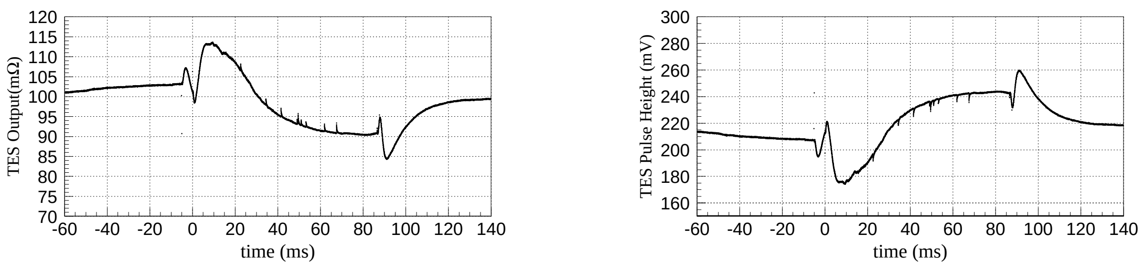

Figure 4.7: Expected fluctuation of R_{TES} and pulse height for 5.9 keV X-ray signals by using the same shot number of Fig. 4.2.

The fluctuation of the TES operating point and the pulse height of X-ray signal during a plasma shot are considered. Before the measurement, we obtained the relation between

$I_{\rm sq}$ and $R_{\rm TES}$, and between $I_{\rm sq}$ and the pulse height of X-ray signal for ^{55}Fe source. Fig. 4.7 shows the expected fluctuations of $R_{\rm TES}$ and the pulse height for 5.9 keV X-ray signals during the plasma shot, assuming that the DC level fluctuations were sufficiently longer compared with the time constant (C/G) for the TES. These parameter were used to obtain the TES output which was the same shot number of Fig. 4.2.

We note that the above picture is derived if the fluctuation of the waveform of the TES calorimeter during plasma shots was caused by the induction current, but there are other influences during shots, because the waveform in normal state of the TES cannot be simply scaled to suprconducting state. We assume that Fig. 4.7 represents the upper limit of the fluctuation of the pulse height and $R_{\rm TES}$, and there is a possibility that the pulse heights for X-ray signals were up to about 20 % larger during plasma shots than in quiecence.

4.2.3 Noise power spectrum during a plasma shot

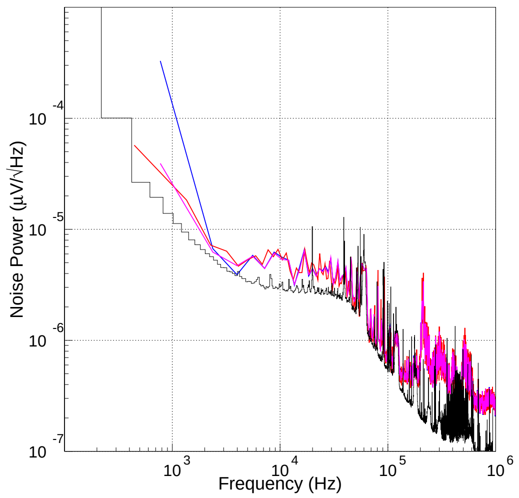

Figure 4.8: The noise power spectrum in quiescence (black) and in the time duration of 35-70 ms corresponding to the flat-top of $I_{\rm p}$ during a plasma shot (blue) in first experiment. Red line represents after reducing the DC level fluctuation, and magenta line represents in 50-70 ms after reducing.

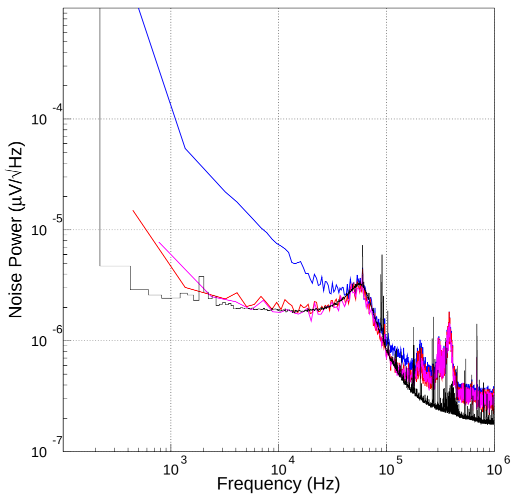

Figure 4.9: The noise power spectrum in second experiment.

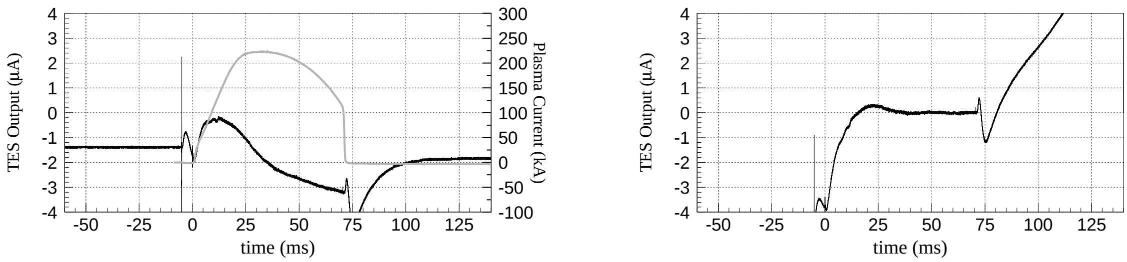

Figure 4.10: Example of the waveform during a plasma shot (left), and after reducing the DC level fluctuation (right).

The noise power spectrum during a plasma shot is compared with that in quiescence. Fig. 4.8 shows the noise power spectrum of the TES calorimeter in the time duration of

35-70 ms during a plasma shot in first experiment (blue), and that in quiescence (black). The spectrum during a plasma shot is large in low frequency in comparison with that in quiescence, because of the DC level fluctuation. We extracted the fluctuation as shown in Fig. 4.10, and the noise spectrum after reducing the fluctuation (red) is also presented. Basically, the energy resolution of the TES is determined dominantly by the signal to noise ratio in 1–100 kHz (in Sec. 4.3). The noise power during a plasma shot was apparently increased in this frequency, which was assumed to be one of the reasons for degrading the resolution for the TES (in Sec. 4.5) in the first measurement. On the other hand, the noise power during a plasma shot in the second measurement was mostly reduced to that in quiescence (Fig. 4.9). The noise power in 1–100 kHz is mainly due to electromagnetic field, not a mechanical vibration, so that we consider that the electromagnetic shield around the refrigerator has effectively reduced the noise power.

4.2.4 Temperature of the detector box during a plasma shot

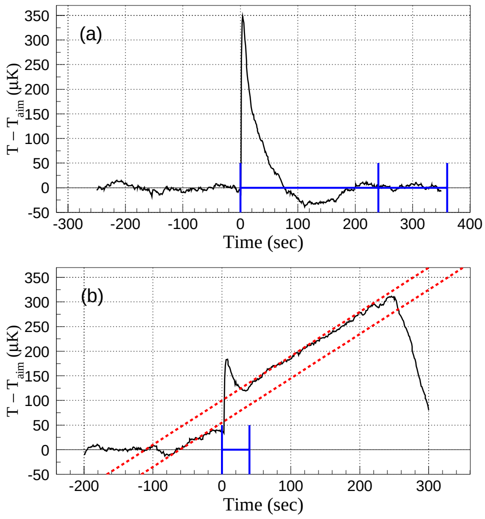

Figure 4.11: Typical measured temperatures of the detector box during a plasma shot. (a) when we maintained the temperature of the box $T_{\rm aim} = 115$ mK with the improved PID method. Blue solid lines represent the time of 240 sec, and 360 sec after a shot respectively. (b) The measured temperature without the temperature control. Blue solid lines represent the time of 40 sec after a shot. Red dotted lines represent the expected line of temperature rise before and after a shot respectively, and the residual between the lines is 45 μK.

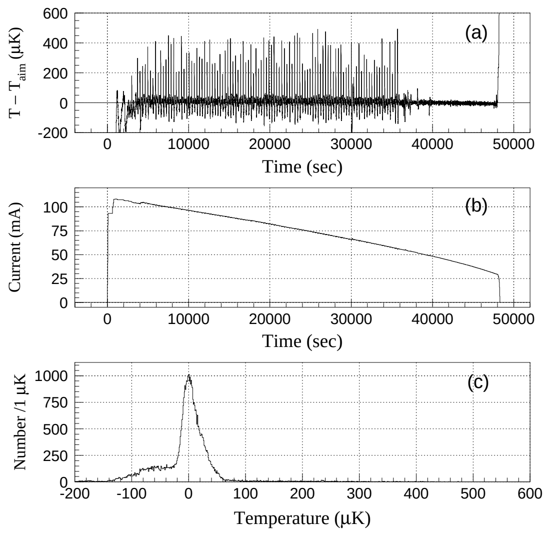

Figure 4.12: (a) Measured temperature of the detector box during the measurement on 18 - Aug, 2004 in first measurement. $T_{\rm aim} = 125$ mK. (b) The magnet current plotted versus time in second. (c) The histgram of the residual temperature at each second in whole time range plotted in (a).

Fig. 4.11 shows the typical temperature behavior during a plasma shot. When the plasma was generated, the temperature rose typically 200–400 μK over the aimed temperature, then recovered by the feed back operation of the PID control method. After 240 sec, the measured temperature was almost the same as the aimed temperature, and consider that the tempetarure of the detector box must be returned before the next shot (after 300–360 sec). However, the operating condition of the TES calorimeter was not probably returned in such a time scale, we have to take into account the effect of different temperature and current condition of the TES (see Sec. 4.2). Because the temperature rise includes the electric noise of the thermometer bridge, measured amplitutes of temperature rises are not correct. We also measured without the temperature control during a plasma shot as shown in Fig. 4.11 (b). The expected lines of temperature rise before a shot were apparently defferent from that after a shot, which indicated that thermal energy caused by an induction heating or a mechanical vibration was generated in the detector box and the saltpill. The residual between the expected lines is 45 μK, which assumed that the thermal input was ~ 30 μJ per one shot. Amount of the thermal input was about 10–15% of the total energy of the detector box including the thermal inflow, the holding time may be somewhat shorter. The reproducibility of the ramping time was typically ~10% (see Sec. 2.3.4), so that the effect of thermal input to the holding time could not be correctly obtained. The measured temperature without the temperature control after a plasma shot was also dropped, and then turned to increase slowly with almost same $\mathrm{d}T/\mathrm{d}t$ to that before a shot.

Fig 4.12 shows the measured temperature of the detector box during the total 103 plasma shots on the last day in the first measurement. It did not show a periodicity for amplitutes of the temperature rise in each shot, and the histgram of the residual temperature in Fig 4.12 (c) indicates that the temperature could maintain 125 mK in the whole time range plotted in (a). We overplot the temperature despersions during the temperature control in AIST in Fig.2.20, which indicates that the temperature of the detector box could be controlled in the same as in TMU. In the second measurement, the behavior of the measured temperature of the detector box was almost the same as that in the first measurement. The induction heating was reduced by the Al magnetic shield around the ADR in the second measurement (also see Sec. 3.5.3), so that the thermal input to the detector box during a shot was assumed to be dominantly caused by the mechanical vibration.

4.3 Optimal filtering of X-ray signals

4.3.1 The method of optimal filtering

The energy of each pulse is determined by the optimal filtering (or Wiener filtering) method commonly used for the microcalorimeter signal analysis [31]. An average pulse shape $s(t)$ is obtained from 5.9 keV (Mn-Kα) X-rays from the calibration isotope, and the filtering template $p(t)$ is calculated using a noise power spectrum $N(f)$ in quiescent periods between plasma shots (in Sec. 2.1.4). If it is assumed that the X-ray energy only scales by the normalization of the signal and that the signal and the noise are independent with each other, the filtered output,

$$e(t) = \int_{-\infty}^{\infty} y(t')\, p(t'-t)\, dt', \tag{4.2}$$

of the cross-correlation between the measured signal, $y(t) = s(t) + n(t)$, and the filtering template, $T(t)$, maximizes the signal to noise ratio, i.e., gives the best energy resolution.

The filtering template is calculated separately in each date, and the energy scale of the filtered output is linearly determined from the average pulse of the 5.9 keV X-rays. Figure 4.13 (a) shows the average pulse, $s(t)$, and the filtering template, $p(t)$. The average pulse can be well fitted by a formula:

$$s(t) = a\left[\exp\left(-\frac{x-t_0}{\tau_{\mathrm{eff}}}\right) - \exp\left(-\frac{x-t_0}{\tau_{\mathrm{rise}}}\right)\right], \tag{4.3}$$

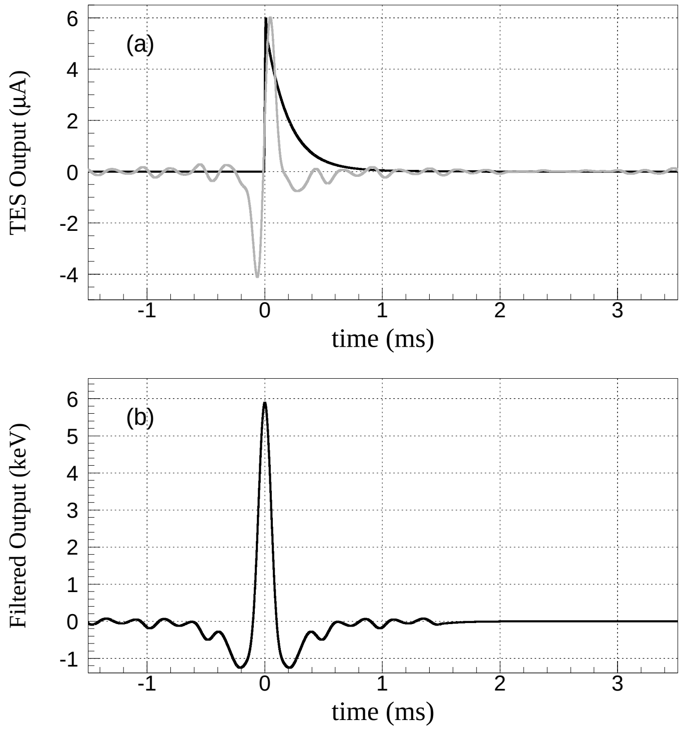

Figure 4.13: (a) The average pulse $s(t)$ derived for 5.9 keV X-rays from the calibration isotope and the filtering template $p(t)$, indicated by black and gray lines, respectively. (b) Filtered output of the average pulse, which is defined as $g(t)$ in text.

where a, $\tau_{\rm eff}$, $\tau_{\rm rise}$, and t_0 represent the pulse height, decay time, rise time, and incident time of the pulse, respectively. Typical values are $a = 6\ \mu$A, $\tau_{\rm eff} = 191\ \mu$s, and $\tau_{\rm rise} = 3.3\ \mu$s. The gray line indicates the filtering template, $p(t)$, in arbitrary unit. As indicated by eq. (2.19), the shape of the template will be identical to the average pulse if the noise is white, i.e., $N(f) =$ constant, except for a constant offset. The constant offset is usually determined by $\int_{-\infty}^{\infty} p(t)\ dt = 0$, so that cross-correlation of $p(t)$ with a pure noise waveform gives an expectation value of 0. The filtered output for the average pulse is shown in Fig. 4.13 (b), which is normalized so that the peak value corresponds to the Mn-Kα energy of 5.9 keV. Here, we define this pulse shape as, $g(t) \equiv \int_{-\infty}^{\infty} s(t')\ p(t'-t)\ dt'$, for later use.

4.3.2 Data extraction after filtering

Figure 4.14 (a) represents the typical filtered output, $e(t)$, calculated for the waveform during the plasma shot in Fig. 4.1 (c). Each peak corresponds to the X-ray signal, and the vertical axis is normalized to the X-ray photon energy in unit of keV. We then extracted individual X-ray signals in the following way: (i) find the maximum point (t_i, e_i) in the filtered output, and determine the arrival time $t = t_i$ and the photon energy $e = e_i$; (ii) subtract $g(t)$ from $e(t)$ after normalized and shifted to match both peaks; (iii) repeat these two procedures until no peak higher than 0.2 keV exist. Figure 4.14 (b) represents the residual after the X-ray signal extraction. The signal extraction looks successful, because the large under-shoot which is seen around the high energy X-rays in Fig. 4.14 (a) disappeared in the lower panel after subtractions. However, it is found that the energy resolution is significantly degraded to ~ 50 eV during the plasma shots, by evaluating the distribution around the zero-level in the residual plot of Fig. 4.14 (b) (Sec. 4.5).

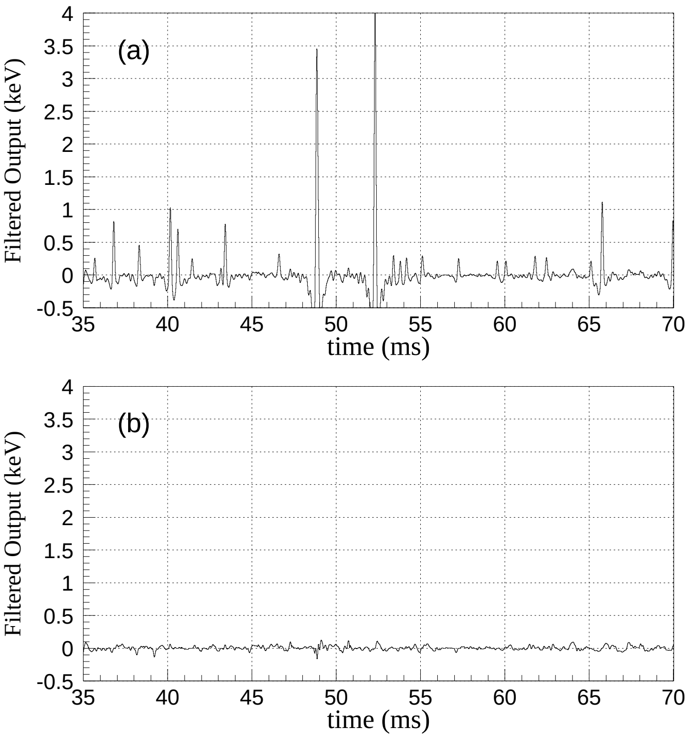

Figure 4.14: (a) Filtered output $e(t)$ calculated for the waveform in Fig. 4.1 (c) during a plasma shot. (b) Residual after the signal extraction.

After the signal extraction, we further screened the events by rejecting the pile-up events and the possible fake detection of noises. The pile-up events are rejected by requiring the time interval between two successive events to be greater than 200 μs. Fig. 4.15 and 4.16 show the histogram of the time interval between the event and the previous event. If events are detected in Poisson random process, the distribution function of the time interval is

$$I(\mathrm{t}) \propto \exp(-r \times t) \tag{4.4}$$

where r is mean predicted event rate, and net count rate is expected to be r/t. In this case, the ratio of pile-up events is $1 - \exp(-r \times t_{\mathrm{thre}})$, where t_{thre} is the time threshold of pile-up rejection. From Fig. 4.15 and 4.16, we suggests that about 14 % and 8 % of detected signals are pile-up events in the first and second measurement, respectively.

We also rejected events where the influence due to the tails of nearby events are significant ($>$ 0.3 keV). The fake events are rejected by calculating the standard deviation of the $e(t)$ and $g(t)$ around the detected signal ($>$ 0.06 keV).

4.4 Detected count history and the histogram

Fig. 4.17 and 4.18 shows the history of detected counts per one shot by using the data extraction summarized in Sec. 4.3.2. In the first measurement, most of span of the plasma duration time were $\sim$ 90 msec, and number of detected counts per one shot extracted in 35–70 ms and 0.2–3.0 keV band follows a Poisson distribution. Results of plasma parameters were stably obtained (see also Sec. 3.4). There are 2 groups in the relation between the span of plasma duration time and number of detected counts, and relatively larger counts were detected from the shot with shorter duration time in 20–80 ms and full

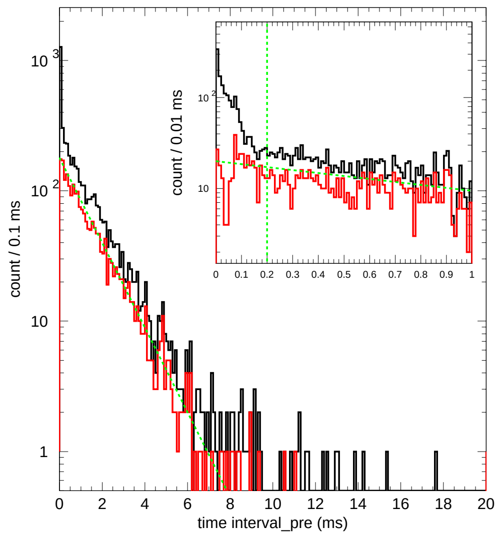

Figure 4.15: Example of the histograms of the time interval between a two successive events for all events in 20–80 ms (black) and 0.2–3.0 keV band (red) in first measurement. Green dash lines represent $\propto \exp(-0.75 \times 1\text{ ms})$ and the threshold of pile-up rejection 200 μs.

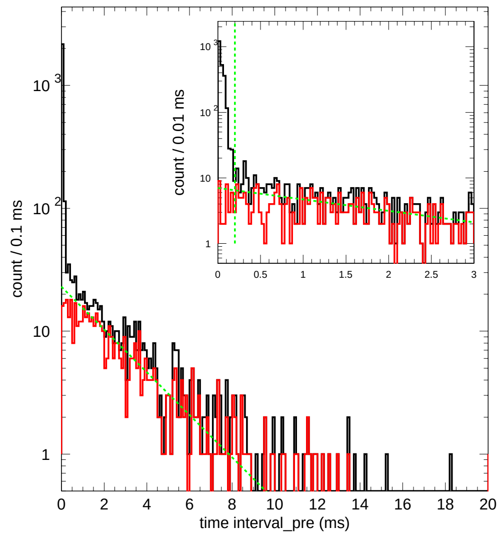

Figure 4.16: Example of the histograms of the time interval for the same as Fig. 4.15 in second measurement. Green dash lines represent $\propto \exp(-0.4 \times 1\text{ ms})$ and the threshold of pile-up rejection 200 μs.

energy band. We suggest that it includes many fake signals (noise, not a X-ray signal) extracted from the last few mili-seconds in the plasma shot. Particularly, number of detected counts were rapidly increased in shorter spans of plasma duration time, with a wider distribution of the duration time in the second measurement. We overplot number of detected counts after screening the events by rejecting the pile-up or fake events. The screened events were assumed to be effectively selected for the spectral analysis.

We examined the X-ray measurement without core-bias of TPE-RX which did not magnetize the Fe core, to investigate the influence of induction voltage from it. But plasmas in this condition were not stably generated and the duration time became shorter. Therefore the signals from plasma shots without core-bias are not included in this study.

4.5 Spectral energy resolution during a plasma shot

We examined the spectral energy resolution of the TES calorimeter during plasma shots by evaluating the distribution around the zero-level in the residual waveforms after the signal extraction. The distributions are produced by adding the residual waveforms for all shots in each day, then averaged the value of energy distribution. Fig. 4.19 shows the energy resolution in -40 – -20, 20–35, 35–50, 50–65, 55-70, 65–80, 110–130 ms in the first measurement. The resolution between -40 – -20 ms and between 110–130 ms are better than 20 eV and almost the same between each days, which indicates that the main cause of the energy degradation during plasma shot does not influence the performance of the TES calorimeter drastically (magnetization, wreckage etc..) as well as the cooling performance of refrigerator. The energy resolution between 20–80 ms duirng a plasma shots are 45∼75 eV, which are factor of 2–3 larger than in quiescence.

In the second measurement, the resolution of the TES calorimeter during plasma shots is degraded to ∼90 eV between 20-30 ms, then improved to ∼45 eV between 50–60 ms,

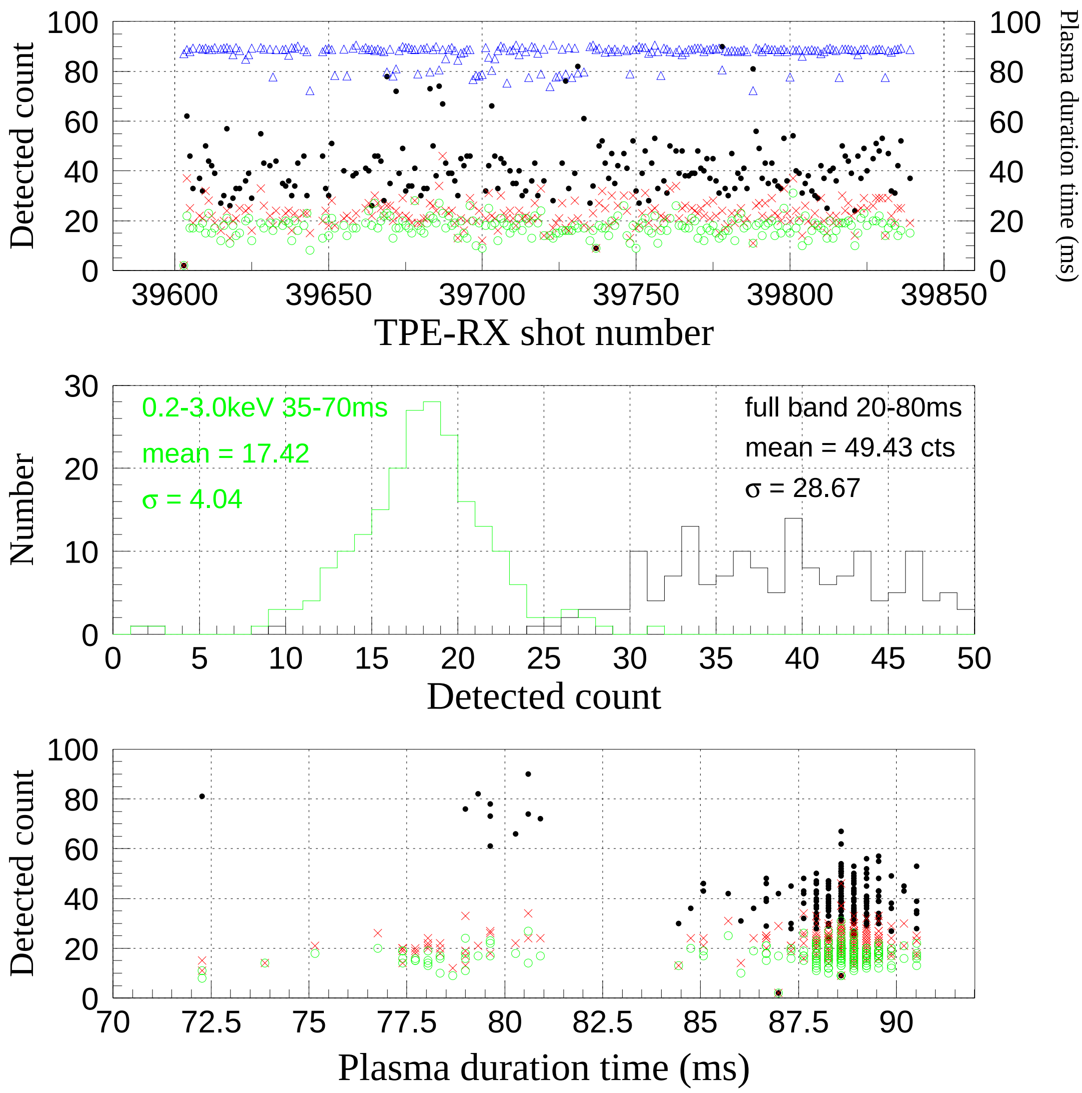

Figure 4.17: Detected count history and the histogram in first experiment. Top : Detected counts of each plasma shot. Filled black circles represent in 20–80 ms in full energy band, red crosses represent in 35–70 ms in 0.2–3.0 keV band, and green open circles represent after being screened. Blue triangles represent the plasma duration time. Middle : Histograms of the detected counts in 20–80 ms in full energy band (black) and in 35–70 ms in 0.2–3.0 keV band after being screened (green). Bottom : Relations of the plasma duration time and the detected counts in each shot.

while 25–35 eV in quiescence, as shown in Fig. 4.20. The degradations of the resolution in the second measurement are somewhat reduced in comparison with that in the first measurement, because of the improvement of the noise power by introducing the electromagnetic shield as described in Sec. 4.9. However, we could not obtain the good energy resolution even in quiescence, so the resolution between 35–70 ms is 58 ± 4.0 eV, which is worse than that in the first measurement.

We overplot the resolution by considering the change of the operating point of the TES described in Sec. 4.2.2, which is improved because of a larger pulse height. We assume that there is a possibility of reducing the degradation to 35 eV between 50–70 ms in the second measurement. In Sec. 5, We indicate that uncertainties of the energy resolution of the TES is almost negligible in the spectral analysis, and we analyzed the X-ray spectrum by using the degraded resolution which was obtained without considering the change of

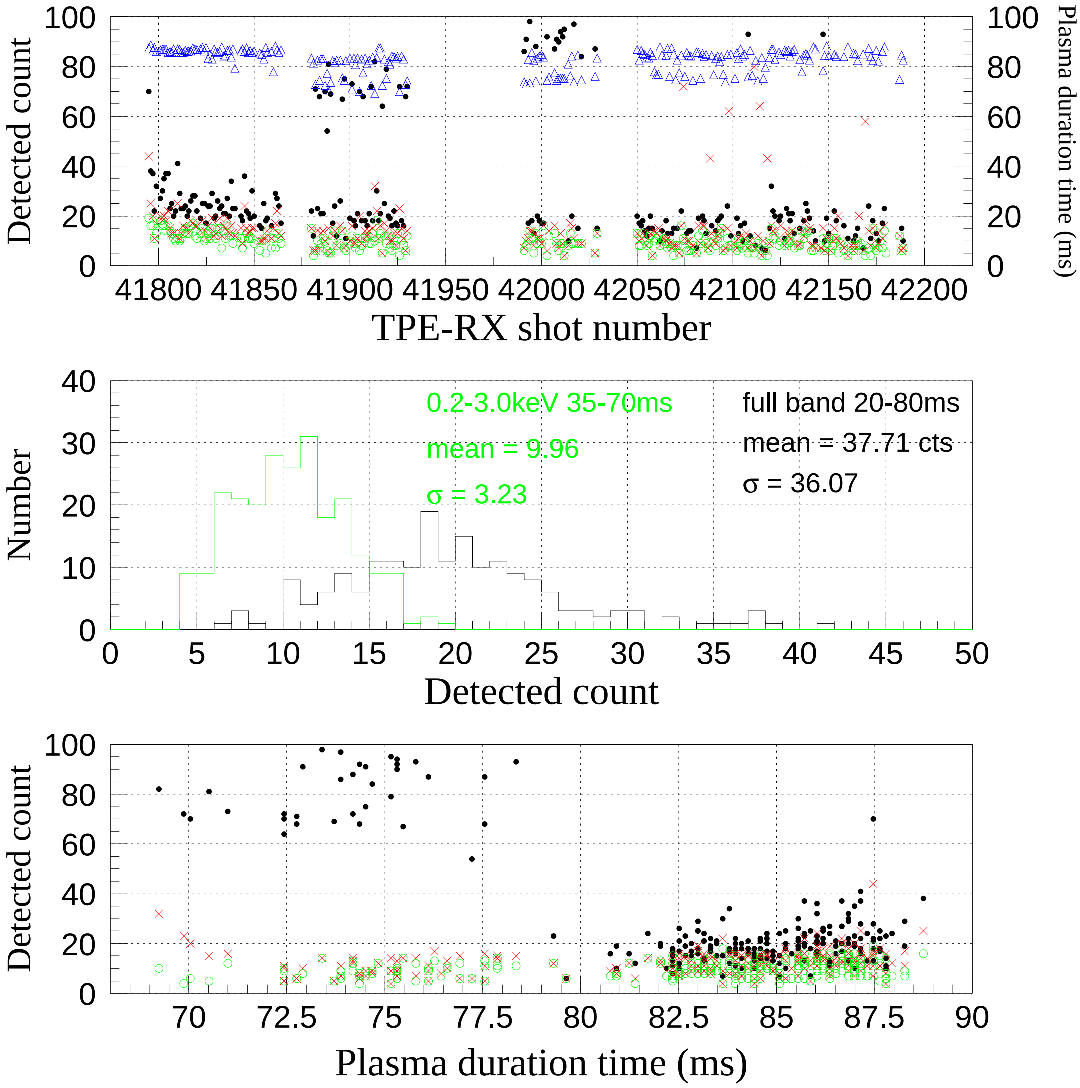

Figure 4.18: Detected count history and the histogram in second experiment, same as Fig. 4.17.

the operating point. g

4.6 Low-energy tail

In principle, TES calorimeter has a flat continuum in lower energy band from a photo-absorbed X-ray energy caused by loss of escaped electrons. Fig. 4.21 shows an example of an energy spectrum when 5.9 keV isolated X-rays are photo-absorbed by TES calorimeters. The spectrum basically includes not only the gaussian line due to the energy resolution of TES calorimeter, but low energy flat tails. In the lower energy band, the tail signals are accumulated by tails from higher energy X-rays, then the influence becomes much higher.

In this thesis, the tail signals are considered as the background of each spectra in the spectral analysis by the simple assumption described below. When $Y_{\rm N}$ counts in $=X_{\rm N}$ bin is detected (N is the bin number) in measured spectrum, the number of tail signals $T_{\rm N-1}$ in $X_{\rm N-1}$ bin is,

$$T_{\rm N-1} = (Y_{\rm N} - F_{\rm N}) \times \frac{S_1}{S_2} \times \frac{1}{N-1} \tag{4.5}$$

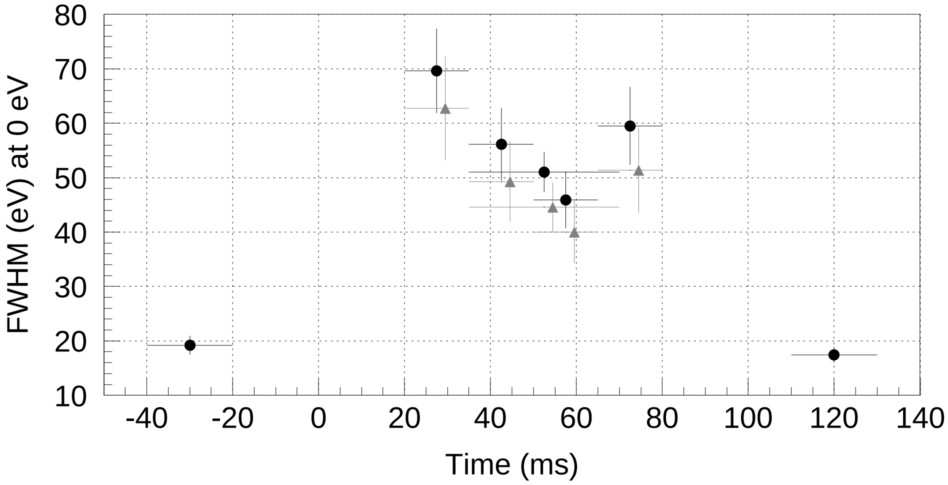

Figure 4.19: Top : Spectral energy resolution in -40 – 150 ms during a plasma shot in first measurement. Black circles represent the resolution without considering the change of the operating pointxg of the TES, and gray triangles represent by reducing the operating point described in Sec. 4.2.2.

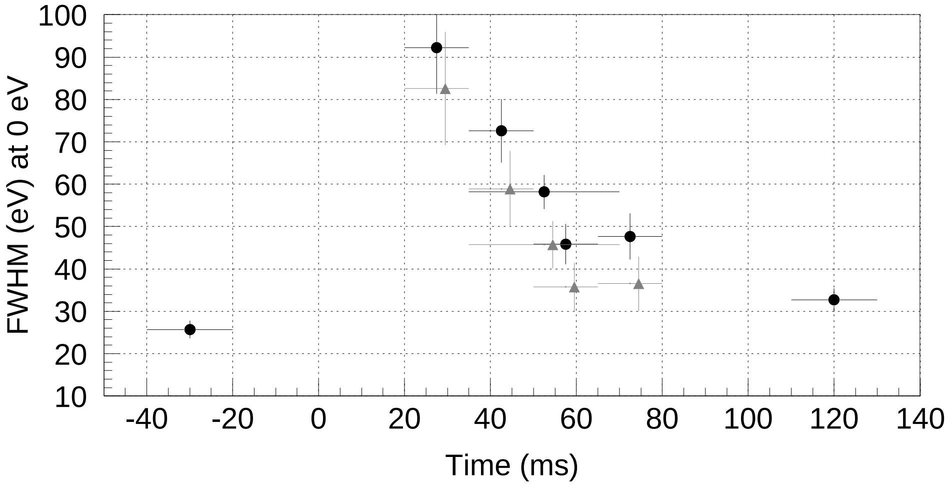

Figure 4.20: Top : Spectral energy resolution in -40 – 150 ms during a plasma shot in second measurement.

where S_2/S_1 is the ratio of number of tail signals / line signals, and $F_{\rm N}$ is sum of number of tail signals calculated from Y in higher bins.

Fig. 4.22 shows the energy spectrum of the TES calorimeter in 35–70 ms in the first measurement, including the expected spectrum of tail signals. We calculated the ratio S_2/S_1 from the result of ground calibration measurement for XRS2 in Suzaku, in which over 500 kcts were measured by using a ^{55}Fe radioactive source with good energy resolution of $\sim$ 6 eV. The ratio is 2.52 ± 0.25%, and we concluded that effects of tail signals were negligible in the spectral analysis. We note that the microcalorimeter of XRS2 instrument has a 8 μm thick HgTe absorber so that the effect of electron loss is different from that of Au absorber of the TES calorimeter, and it's also expected that there is an energy dependence in the ratio S_2/S_1. Though the effects of tail signals can not be negligible if that the ratio S_2/S_1 is more than 12%, no other results withsufficient counts have been measured by microcalorimeters. we consider it unlikely that a TES shows factor of five

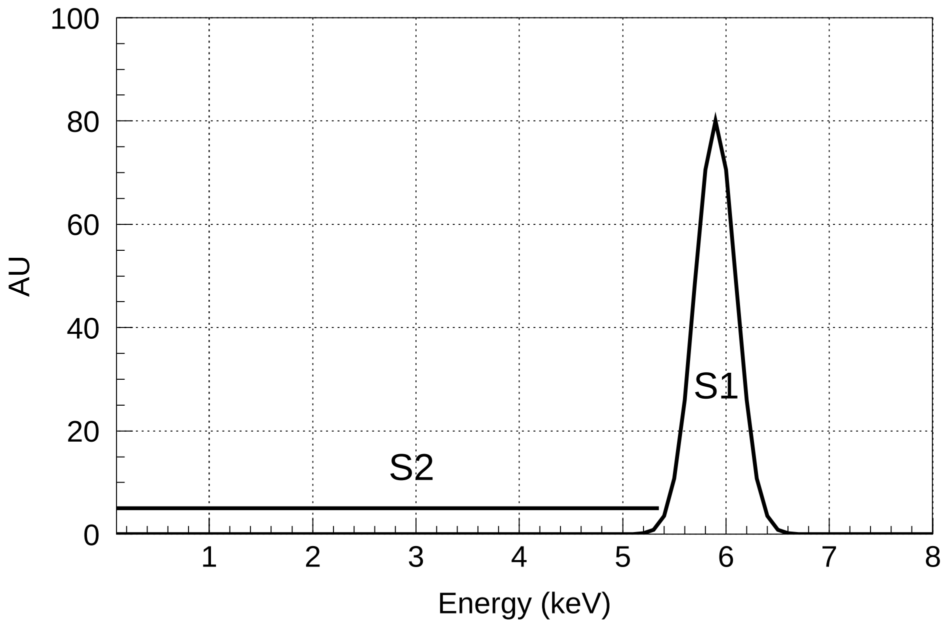

Figure 4.21: Example of an energy spectrum including tails as well as a gaussian line when isolated X-rays (5.9 keV in the figure) are photo-absorbed by TES calorimeters. The ratio of number of tail signals / line signals is S_2/S_1.

larger tail ratio than the XRS.

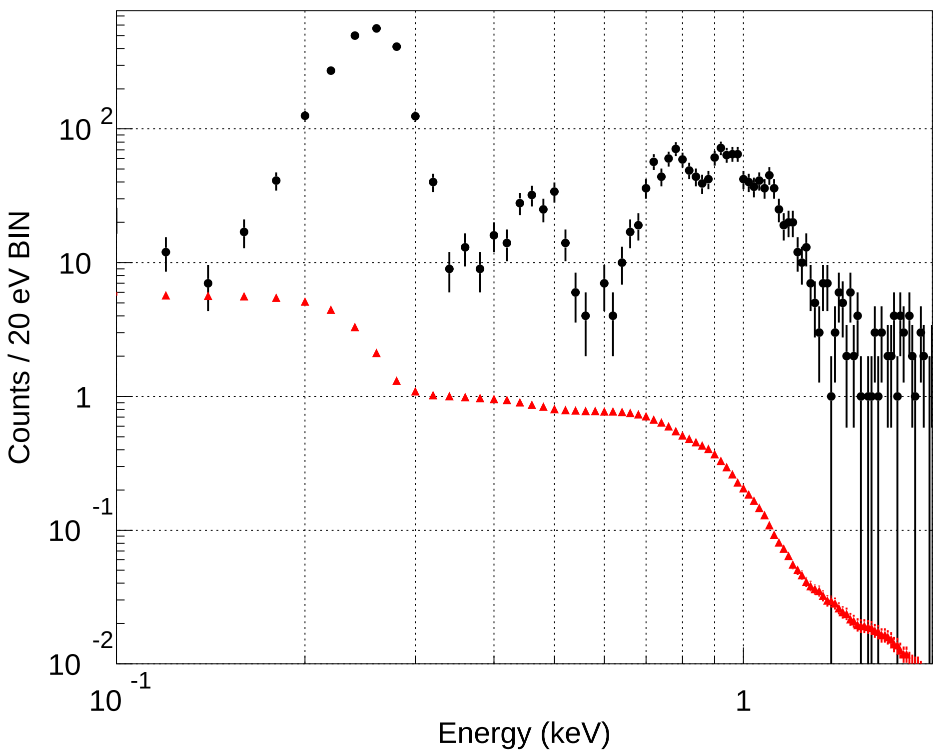

Figure 4.22: The energy spectrum of the TES calorimeter (black circles) and the expected tail signals (red triangles). Measured spectrum is obtained in 35–70 ms after pile-up extraction in first measurement. $S_2/S_1 = 2.52\%$.

Chapter 5

X-ray Spectral Analysis

In this chapter, analysis of the X-ray spectra of TES calorimeters obtained by the data reduction discussed in Sec. 4 are described, including the time variability together with the hard X-ray spectrum from the SiLi detector. The obtained spectra in the first measurement are examined simultaneously with that measured with SiLi detector in almost the same conditions. However, the spectra in the second measurement are independently examined, because apparently different electron temperatures were measured from the ruby laser Thomson scattering method in this measurement.

5.1 Introduction of X-ray radiation process

In nature, X-rays are produced by a variety of processes which may be classified roughly as thermal or non-thermal processes. The emission mechanisms include blackbody radiation, bremsstrahlung (thermal or nonthermal), line emission, recombination radiation, synchrotron radiation, and inverse Compton radiation. If the energy of the generating electron is thermal, the electrons are described by a Maxwellian energy distribution characterized by a certain temperature T, we speak of *thermal* process. Temperature of a million Kelvin or more are required.

The important process considered in this study are line and continuum emission from optically thin deuterium plasma icluding some impurities in which collisional ionization (collisional excitation) process is dominant. Its characteristic parameters are electron temperature T, element–impurity abundances, electron density $n_{\rm e}$, and emission measure EM — $\int n_{\rm e} n_{\rm i} dV$. The ionization balance of each elements are mainly determined by electron collision, not a phtoionization. Furthermore, magnetic field B for the plasma confinement makes an important process in the deuterium plasma. We principally consider three kind of emission process, (1) thermal bremsstrahlung continuum, (2) discrete line emission of ions, (3) cyclotron emission. In (1), the total loss rate of the plasma is

$$-\left(\frac{\mathrm{d}E}{\mathrm{d}t}\right)_{\rm brems} = 1.435 \times 10^{-40} Z^2 T^{1/2} \bar{g} n_{\rm e} n_{\rm i} \ \mathrm{W\ m^{-3}} \tag{5.1}$$

where Ze is the charge of ions and $Z = 1$ is used in this study. $\bar{g}$ is a frequency averaged Gaunt factor. Detailed calculations shows that $\bar{g}$ lies in the range $1.1 - 1.5$ and a good aproximation is 1.2. The total loss rate of thermal bremsstrahlung is propotional to EM. In (2), we can investigate the ratio of elements in the plasma.

In addition, we have to consider the X-ray emission other than the plasma, bremsstrahlung, neutral X-ray fluorescent lines, scattering and reflection from the surface of the stenless vessel.

XSPEC

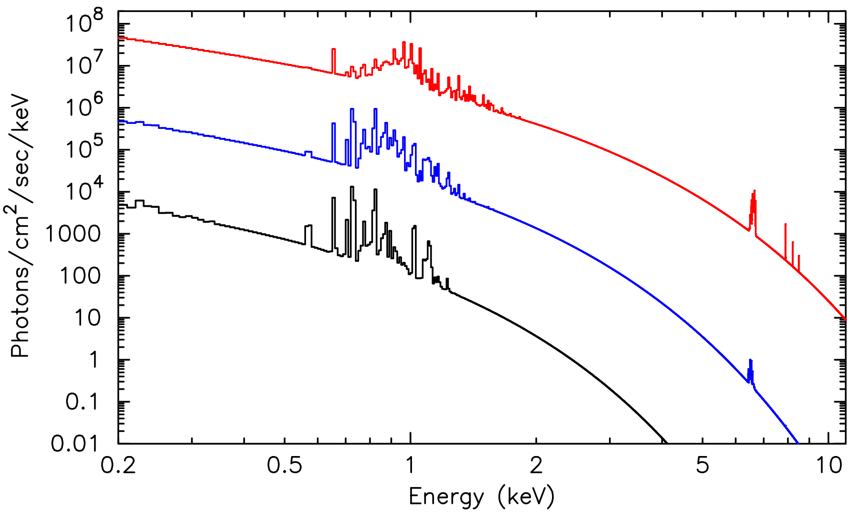

Figure 5.1: Examples of optically thin, thermal plasma model spectra in collisional ionization equilibrium —MEKAL. 3 electron temperatures (0.4, 0.6, 1.0 keV) are represented by black, blue, and red lines, respectively. Oxygen (1×10^{-4}) and Fe (1×10^{-5}) are only assumed in these spectra of hydrogen plasmas (photons are varied in each model).

X-ray spectral modeling is an important tool to study the physical parameters of hot plasmas. The usual procedure is to apply a forward modeling technique by convolving theoretical model spectra with the instrumental response and to vary the model parameters in order to optimize the fit of the model to the observational data. In this study, the spectra are examined using a spectral fitting package XSPEC v11.3 (http://xspec.gsfc.nasa.gov/) [1] which is widely used in the X-ray astronomy. In this package, we can compare measured spectra $D(PI)$ which is defined in the detector channel space PI with various model spectra $M(E)$ in the energy space E, based on the χ^2 statistics or the Maximum likelihood fitting. To conduct the spectral fit, a detector response must be supplied, which is represented by a matrix $R(E, PI)$ containing detector information such as detection efficiency, energy scale, energy resolution, etc. The model is compared with the data after folded by the response matrix as $\sum_E R(E, PI)\, M(E)$. Here, PI represents the pulse height invariant, which is usually determined to be propotional to E by subtracting an offset and correcting non-linearity for raw detector channel number, although this is not a requirement. The XSPEC package internally has a library of a large number of spectral models including several kinds of plasma emission code. Multiple number of models can be included in the model spectrum by adding or multiplying them, and also multiple number of data spectra can be treated simultaneously in the spectral fitting. We derived errors in 90% confidence level.

Fig. 5.1 shows examples of optically thin, thermal plasma model spectra — MEKAL model in collisional ionization equilibrium (CIE). In particular, line emissions in 0.7-1.2 keV band as well as the continuum emission vary as a strong function of temperature, but we note that ionized emission lines from Cr-L are not included in the MEKAL model, which is partly responsible for the fit residuals around Fe-L complex (0.7–1.2 keV).

5.2 Spectral analysis at flat–top phase

We have extracted X-ray signals in the time duration between 35–70 ms from all the available plasma shots obtained in the first measurement, which amounts to 214 shots in total.

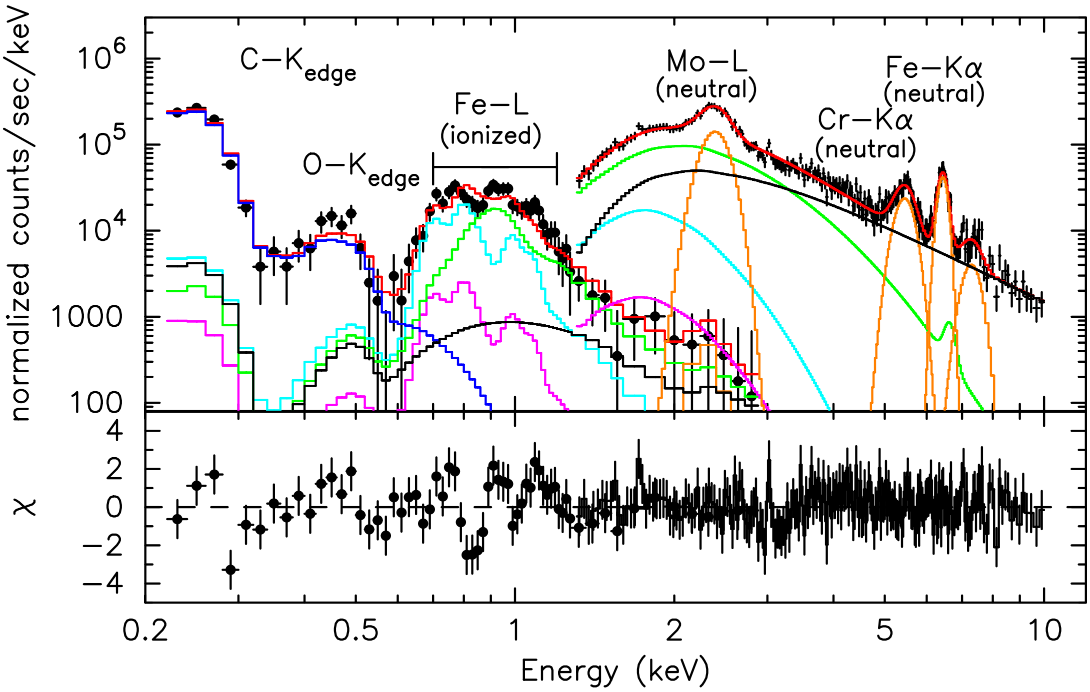

Figure 5.2: 0.2-3.0 keV X-ray spectrum of the TES calorimeter obtained in 35–70 ms after the pile-up extraction, and the SiLi detector in 1.3–10 keV band. Two red lines show the best-fit model spectra folded by the detector response matrices for both detectors, and contribution each component is indicated by different colors.

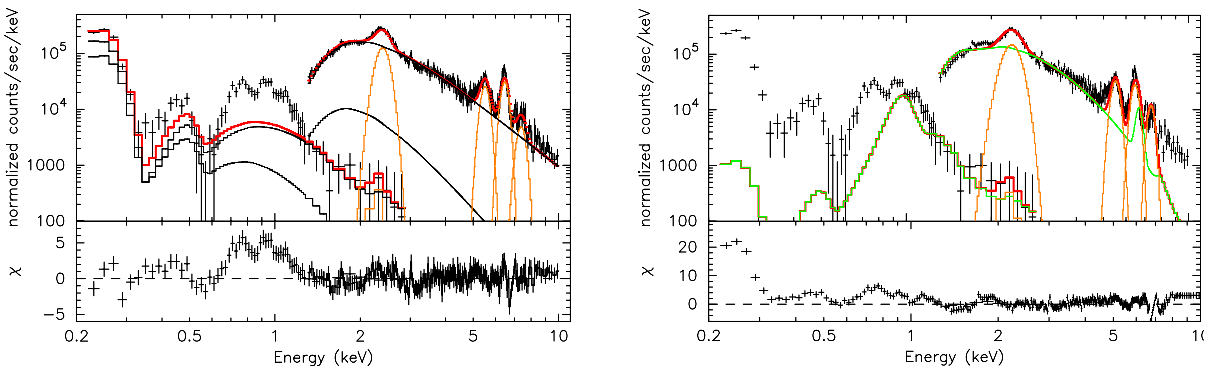

Figure 5.3: X-ray spectra with the TES calorimeter (black crosses) in the 0.2–3.0 keV band and the SiLi detector in 1.3–10.0 keV band. Left: The model spectra (red lines) including 4 gaussian lines (orange) and 1 power-law continuum (black lines) have apparent differences from the measured spectra. Right: The model spectra (red lines) including 4 gaussian lines (orange) and 1 continuum of thermal plasma (green lines).

Several shots in Table 3.1 are excluded because of GV closure, failure in the calorimeter measurement or in the plasma operation. The average number and the standard deviation of the detected count per each shot are 17 ± 4 c shot^{-1}, corresponding to ~ 514 c s^{-1}, and fluctuation of the count is consistent with the Poisson distribution. With this rate, 14 % of detected signals suffer from pile-up compare with the incident count rate ~ 750 c s^{-1}. We rejected the pile-up events.

As a result, 3258 count per 214 shots (7.49 s exposure) remain in the energy range of 0.2–3 keV, after 1098 pulses are rejected as pile-up or fake events. The obtained energy spectrum is presented in Fig. 5.2 shown by crosses with filled circles.

The X-rays above 1 keV have been measured with the SiLi detector at the same port with similar plasma parameters in October 2003. We have also utilized this spectrum

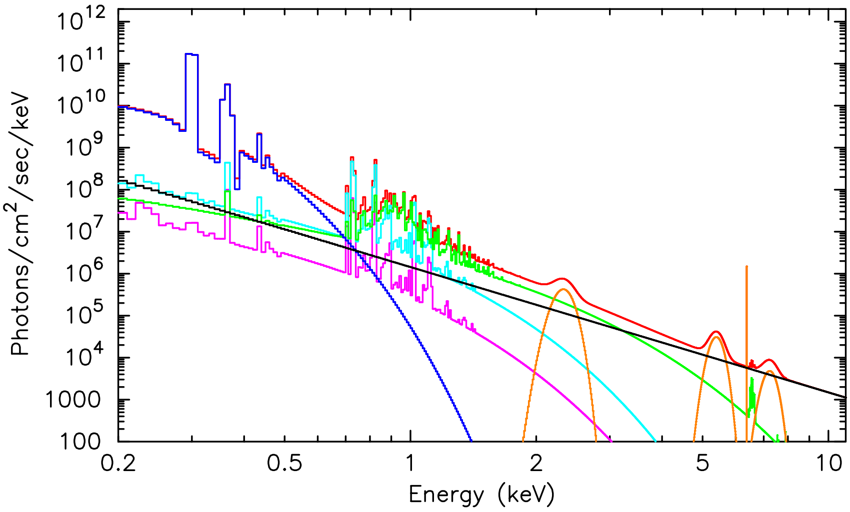

Figure 5.4: The incident best fit model spectrum indicated in Fig. 5.2 in energy space (red line). The contribution each component is indicated by different colors (see Tab. 5.1 in detail).

which containes 13,394 count per 25 shots (0.875 s exposure) in 1.3–10 keV, between 35–70 ms in the spectrum, as indicated by crosses in Fig. 5.2. The plasma current $I_{\rm p}$ of TPE-RX was 200 kA during the SiLi measurement which was slightly different from that at the measurements of the TES (220 kA), but the difference is negligible in the analysis. The measured spectra of the TES calorimeter and the SiLi detector spectra are fitted simultaneously with the same model parameters except for the overall normalization in our spectral analysis. We have prepared response matrices for both detectors based on the detector specifications, which are plotted in Fig. 2.22. The energy scale is determined by the Mn-Kα (5.9 keV) line from the calibration isotope for each detector. The energy resolution for the TES calorimeter is 51 eV FWHM at 0eV (baseline fluctuation) and rises linearly up to 51–300 eV at 5.9 keV, while, for the SiLi detector, we have adopted 304 eV at 5.9 keV and used the relation FWHM(E) = 304 eV $\times$ (E/5.9 keV)$^{1/2}$ (see also Sec. 5.3).

The red lines in Fig. 5.2 represent an example of the spectral fitting result, in which 4 optically-thin thermal plasma emission models + 1 power-law model + 4 Gaussian models are considered. As a first step, 2 power-law continuum or 1 temperature optically thin thermal plasma continuum in addition to 4 Gaussian lines have been considered. But there are large residuals particularly between 0.7-1.2 keV for the 2 power-law model spectra, while 1 temperature thermal model spectra gives a poor fit in $<$ 1 keV and $>$ 5 keV bands, as shown in Fig.5.3. It indicates that the measured spectra cannot be modeled by a monochromatic emission. We have adjusted the energy scale for the TES calorimeter by about 2% to eliminate the residual structure around carbon and oxygen K-edges (279 eV and 533 eV, respectively) produced by the X-ray window of the ADR, which we think are within the uncertainty considering a slight non-linearity in the energy scale. The incident X-ray model spectrum in the energy space described in Fig. 5.2 is plotted by the red line in Fig. 5.4, and contribution of each component is indicated by different colors. Number of fitting parameters are 26 in total, and the best fit χ^2/d.o.f. = 287.9/265, where d.o.f. represent the degree of freedom, i.e., the number of spectral bins subtracted by the number of fitting parameters.

MEKAL model: $F_X = 0.206$ erg cm^{-2} s^{-1} (0.2–10 keV)	
$kT_1 = 52^{+4.5}_{-2}$ eV, $norm_1 = 7.50^{+1.8}_{-2.6} \times 10^8$,	$F_X = 0.180$ (blue)
$kT_2 = 157^{+27}_{-52}$ eV, $norm_2 = 2.69^{+0.56}_{-0.67} \times 10^7$,	$F_X = 0.020$ (light blue)
$kT_3 = 350^{+33}_{-97}$ eV, $norm_3 = 3.90^{+9.52}_{-2.76} \times 10^6$,	$F_X = 0.003$ (magenta)
$kT_4 = 800^{+56}_{-43}$ eV, $norm_4 = 2.27^{+0.47}_{-0.41} \times 10^6$,	$F_X = 0.002$ (green)
[C/D] $= 133^{+34}_{-60} \times 10^{-5}$, [O/D] $< 1.2 \times 10^{-5}$	
[Fe/D] $= 1.6^{+0.50}_{-0.45} \times 10^{-5}$	
power-law model:	$F_X = 0.001$ (black)
$\Gamma = 2.98^{+0.065}_{-0.065}$, $norm = 1.39^{+0.66}_{-0.43} \times 10^5$	
gaussian model:	$F_X = 0.0001$ (orange)
$E_1 = 2322^{+11}_{-11}$ eV, $\sigma_1 = 113^{+12}_{-11}$ eV, $S_1 = 9.96^{+2.28}_{-1.42} \times 10^3$,	EW = 0.369 keV
$E_2 = 5389^{+27}_{-27}$ eV, $\sigma_2 = 186^{+35}_{-19}$ eV, $S_2 = 1.18^{+0.19}_{-0.12} \times 10^3$,	EW = 1.30 keV
$E_3 = 6370^{+48}_{-10}$ eV, $\sigma_3 = 0^{+46}$ eV, $S_3 = 1.22^{+0.11}_{-0.10} \times 10^3$,	EW = 2.26 keV
$E_4 = 7232^{+98}_{-109}$ eV, $\sigma_4 = 244^{+112}_{-72}$ eV, $S_4 = 242^{+92}_{-63}$,	EW = 0.714 keV

(Errors are 90% confidence level)

Table 5.1: List of best fit parameters indicated in Fig. 5.2. The colour of each component in 5.4 are also listed.

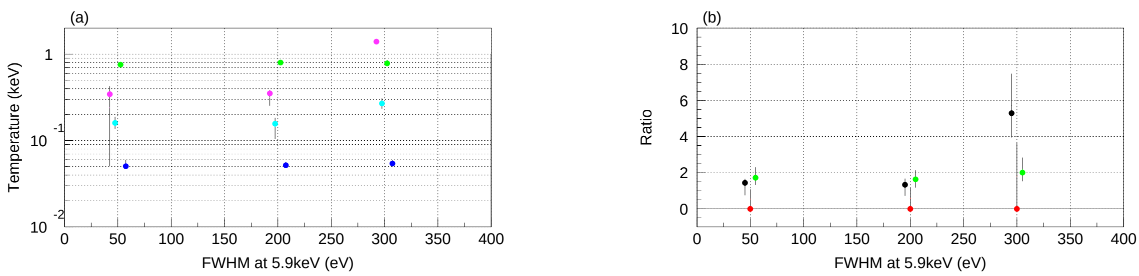

Figure 5.5: Energy resolution dependences of various parameters for spectral fitting. (a) relation between the resolution at Mn Kα and temperatures of each thermal plasma model component with same colours described in Fig. 5.4. (b) relation between the resolution and fraction of impurities, Carbon ($\times 10^{-3}$, black), Oxygen ($\times 10^{-5}$, red), Fe ($\times 10^{-5}$, green).

5.2.1 Energy resolution dependence

The energy resolution of the TES calorimeter at 0 eV due to baseline fluctuation is closely examined by evaluating the distribution around the zero-level in the residual waveforms after the signal extraction, as described in Sec.4.5. However, the derived spectra contain no spectral line. Therefore we have checked the dependence on energy resolution by applying various energy responses for the TES calorimeter.

Fig. 5.5 shows the dependence of energy resolution for fraction of impurities and temperatures of each thermal plasma model component. The spectral model used in this analysis is 4-thermal plasma + 1 power-law and 4-gaussian, which is the same as Fig. 5.4. We obtained FWHM 69 ± 2 eV from the fitted line at $\sim$250 eV, which is considered to be upper limit of the energy resolution. There is a Carbon-edge at 279 eV and the transmission below 280 eV rapidly drops (Fig. 2.22), therefore this provides a line-like shape even it is a continuum. We have to perform a detailed analysis by evaluating through various model spectra. On the other hand, we have obtained a poor fit when the assumed energy resolution was 500 eV at 5.9 keV (FWHM 70 eV at 250 eV). We can assume that FWHM < 500 eV at 5.9 keV. As shown in Fig. 5.5(b), impurities derived in spectral fitting are considered to be the same within the errors, while the temperature of one thermal plasma component shows a dependence on FWHM. However, variation of the energy resolution gives little difference in the derived temperature distribution. In this analysis, we have used mainly the energy response of the TES which gives the energy resolution of 200 eV at 5.9 keV.

5.2.2 Contamination on the X-ray window

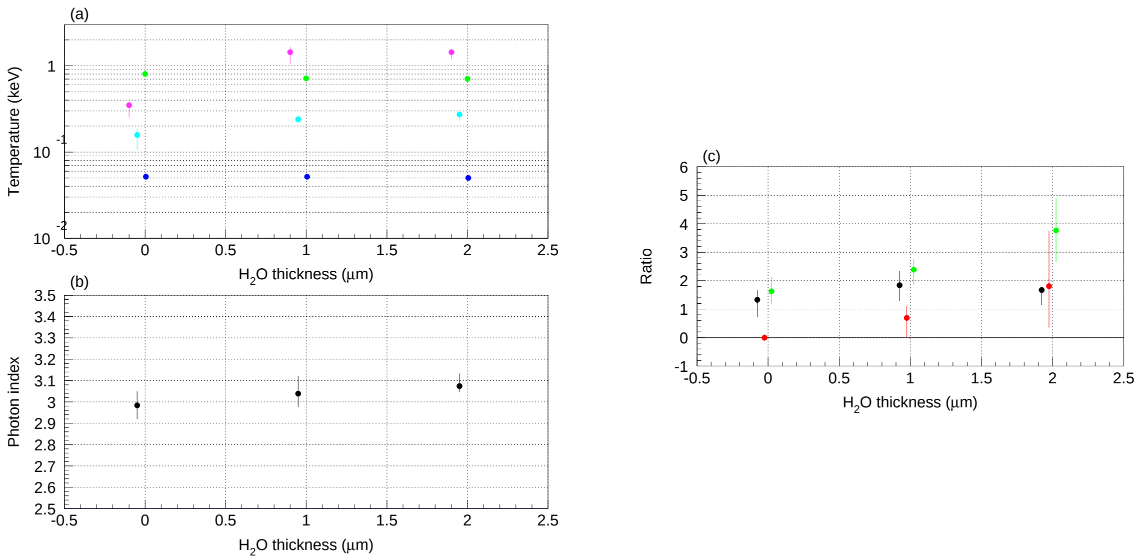

Figure 5.6: (a) relation between the thickness of H_2O on the films of X-ray window and temperatures of each thermal plasma model component with same colours described in Fig. 5.4. Filled circles represent the model of 4 thermal plasma and 1 power-law. (b)relation between the H_2O thickness and power-law photon index. (c) relation between the H_2O thickness and fraction of impurities, Carbon ($\times 10^{-3}$, black), Oxygen ($\times 10^{-4}$, red), Fe ($\times 10^{-5}$, green).

As described in Sec. 2.4.2, we measured the transmission of the X-ray window in TMU and obtained a result that some impurities — most of which were considered to be ice — built-up on the surface of the films used for the X-ray window. In measurements at TMU, 1.3 ± 0.3 μm thickness of Oxygen was estimated for the same X-ray window used in the second measurement, while thicker Oxygen was thought to be contaminated on the few aperture cones in the first measurement. We cannot measure the thickness of impurities directly because the surface of the films are contaminated during the cooling operation. We may assume that most of the impurities are on the films above 50 K and 150 K shield, and the temperature distribution in the ADR was constantly controled except for the components under 0.1 K during plasma measurements at AIST. Therefore, the thickness of impurities are unlikely to be drastically varied in these measurements.

Fig. 5.6 shows the difference on the spectral results by assuming various thicknesses of ice (0, 1, 2 μm of H_2O). The 3 temperatures out of 4 show no correlaction, while the temperature of plasma component becomes lower when the fraction of impurities is larger with higher thickness of H_2O. In particular, the fraction of Carbon exceeds 2×10^{-3}, which seems unlikely in the present TPE-RX plasma. We may, therefore, assume that less than 1μm of H_2O was built-up on the films in the first measurement.

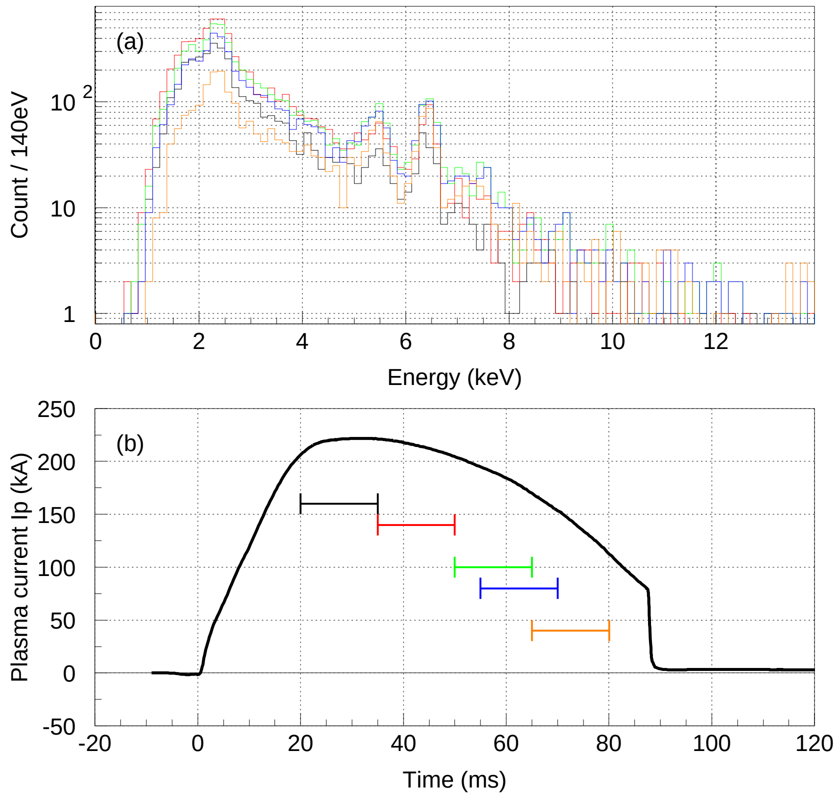

Figure 5.7: (a) X-ray spectrum obtained by the SiLi detector at the plasma current $I_{\rm p} = 200$ kA. Black, red, green, blue, and orange solid lines represent the energy spectrum in 20-35 ms, 35-50 ms, 50-65 ms, 55-70 ms, 65-80 ms, respectively. (b) Typical waveform of the plasma current $I_{\rm p}$ and signal extracted time regions for each spectrum.

5.3 Spectral analysis of SiLi detector

We also examined the spectral analysis for SiLi detector independently. The obtained spectra of SiLi detector for 25 shots in total are shown in Fig. 5.7(a) and 5.8 (see also Sec. 2.5.3). There are 18246 counts per 25 shots (1.5 sec exposure) during 20–80 ms in 1.3–10 keV band.

As our first step, we fitted the reduced spectrum in 20–80 ms with a single power-law and 4-simple gaussian model (for 2.3 keV Mo-L, 5.4 keV Cr-K, 6.4 keV Fe-K, $\sim$7.4 keV Fe-Kβ–Ni-K) in 1.3–10 keV band. Number of fitting parameters are 14 in total, and the best fit χ^2/d.o.f. $= 222.2/231$. In the best-fit results, we obtained the power-law photon index $\Gamma = 3.80 \pm 0.01$, X-ray flux $= 1.27 \times 10^{-3}$ erg cm^{-2} s^{-1} in 1.3–10 keV band, and equivalent width (EW) of Fe-K line at 6.4 keV is 2440 eV. The line energy is consistent with the neutral Fe-Kα within the error.

The FWHM of Fe-K line $= 304 \pm 25$ eV was obtained from the spectral fitting, while FWHM of other lines were larger than 350 eV. The nominal energy resolution of the SiLi detector is 150 eV at 5.9 keV, but apparently it is degraded during the plasma shot. The FWHM of the Fe-K line suggests it may contain more than 2 spectral lines, so it's thought to be the upper limit of energy resolution for the SiLi detector during the plasma shot. In our spectral analysis, we adopted the energy resolution of the detector FWHM = 304 eV at 5.9 keV and FWHM(E) $= 304 \times$ (E/5.9 keV)$^{0.5}$.

In the next step, we divided the measured signals into five time regions, 20–35, 35–50, 50–65, 55–70, 65–80 ms, respectively, as described in Fig. 5.7(b) to examine the time variability of X-ray spectrum of the SiLi detector. Then we fitted the spectrum with the

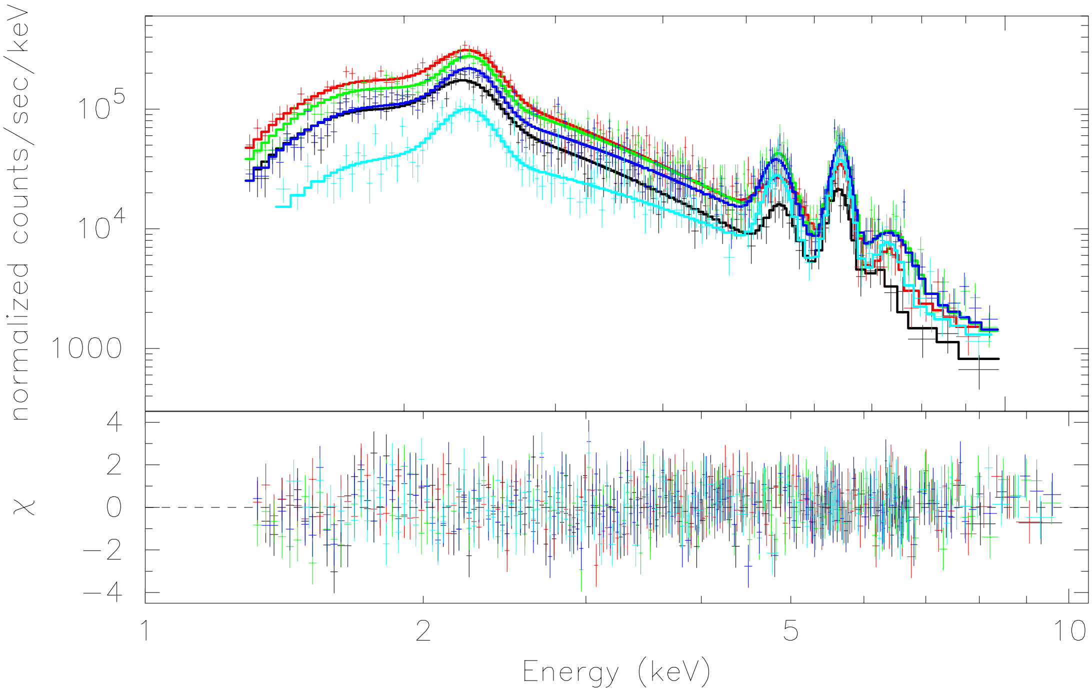

Figure 5.8: Top : X-ray spectrum obtained by the SiLi detector. Each solid lines represent as same to Fig. 5.7(a). Bottom : The residuals in terms of sigmas for each energy bin.

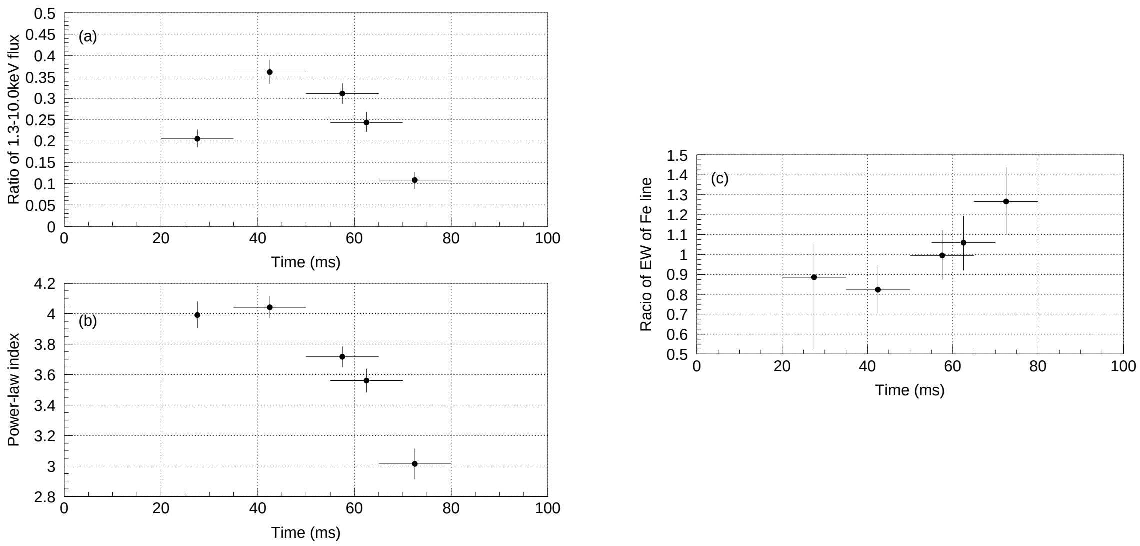

Figure 5.9: Time dependence of the 1.3–10.0 keV flux, power-law index, and the equivalent width of Fe line in X-ray spectrum of the SiLi detector. The flux and the equivalent width are normalized with results obtained from the 20–80 ms spectrum respectively.

same model to the 20–80 ms spectrum. Fig. 5.9 shows the time dependence of the 1.3-10 keV flux and spectral parameters from fitting results. The flux and the equivalent width of Fe-K are normalized with results obtained from the 20–80 ms spectrum respectively. The time dependence of the 1.3-10 keV flux is very similar to that of the plasma current I_{p}, but the time at the maximum flux is 40–45 ms, which is different from the flat-top ($\sim$ 30 ms) phase of I_{p}. The X-ray specra becomes harder and the EW of Fe-K line becomes larger with time. We suggest that the X-ray spectrum varied significantly during the plasma shot.

5.4 Time dependence of X-ray spectra

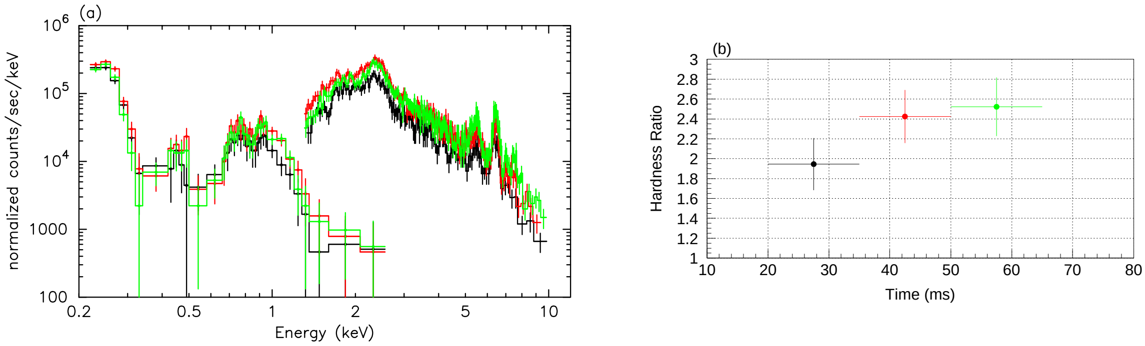

Figure 5.10: (a) X-ray spectra with the TES calorimeter in 0.2–3.0 keV band and SiLi detector in 1.3–10 keV band (black: 20–35 ms, red: 35–50 ms, green: 50–70 ms, as same to Fig. 5.8). (b) Time dependence of the hardness ratio, counts in 0.8–3.0 keV band / counts in 0.5–0.8 keV band.

Time dependence of the X-ray spectra obtained with the TES calorimeter is considered. Because of the poor statistics against the spectral fitting, we calculated the hardness ratio (HR) for each spectra, namely detected counts in 0.8–3.0 keV band divided by the counts in 0.2–0.8 keV band. Fig. 5.10 shows the obtained spectra together with the SiLi detector data, and the calculated HR as a function of extracted time region. The HR rises with time, indicating that the X-ray spectrum becomes harder in the same way as that seen with SiLi detector (Fig. 5.9).

5.5 Spectral analysis of second measurement

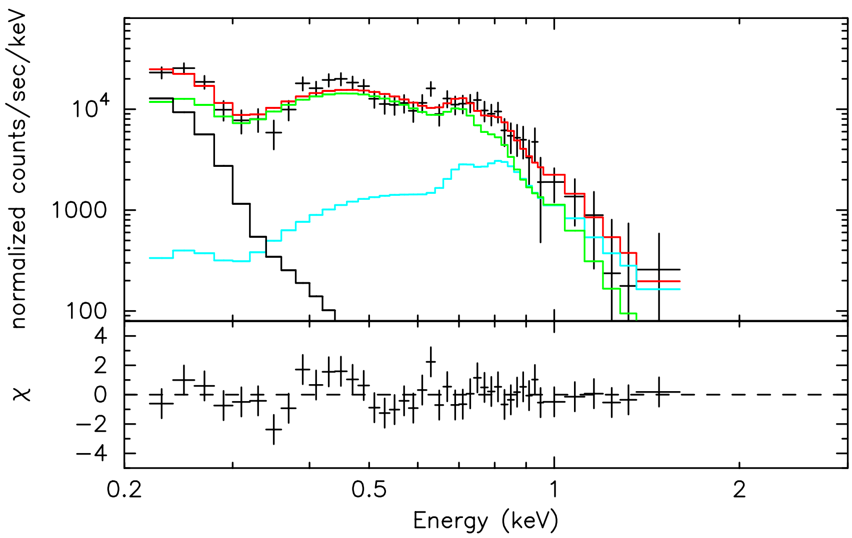

Figure 5.11: 0.2-3.0 keV X-ray spectrum of the TES calorimeter obtained in 35–70 ms after the pile-up extraction in second measurement. Red lines show the best-fit model spectra (2 thermal plasma + 1 power-law) and contributions of each component are indicated by different colors.

We also carried out the spectral analysis for the TES calorimeter data in the time duration between 35–70 ms from all the available plasma shots in the second measurement. The measurement amounts to 273 shots in total. As shown in Fig. 3.6 and described in Sec. 4.4, there are some plasma shots with less than 70 ms duration, which are discarded

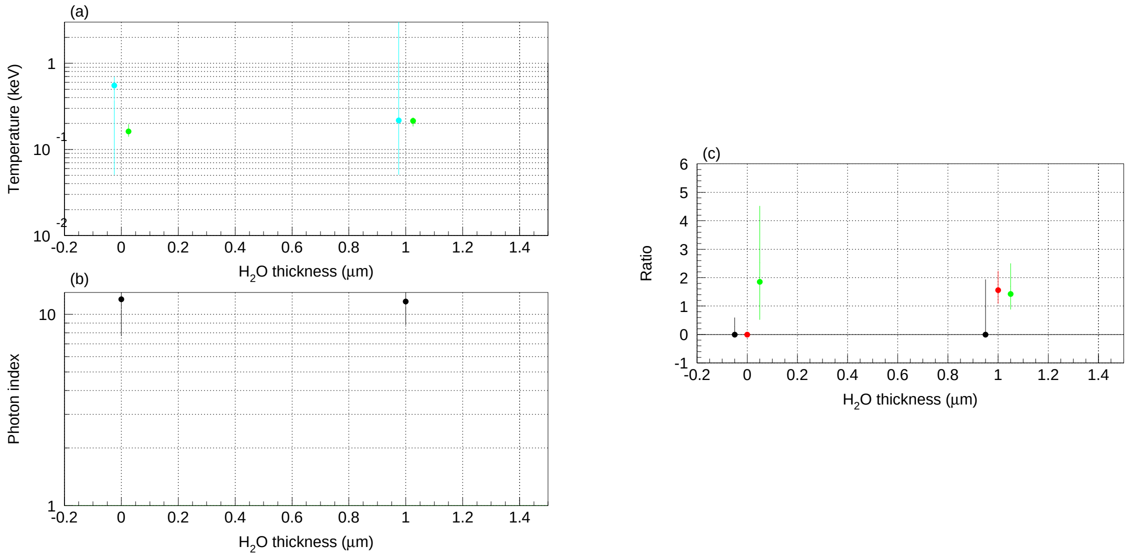

Figure 5.12: (a) relation between the thickness of H_2O on the films of X-ray window and temperatures of each thermal plasma model component with same colours described in Fig. 5.11. (b)relation between the H_2O thickness and power-law photon index. (c) relation between the H_2O thickness and fraction of impurities, Carbon ($\times 10^{-5}$, black), Oxygen ($\times 10^{-5}$, red), Fe ($\times 10^{-6}$, green).

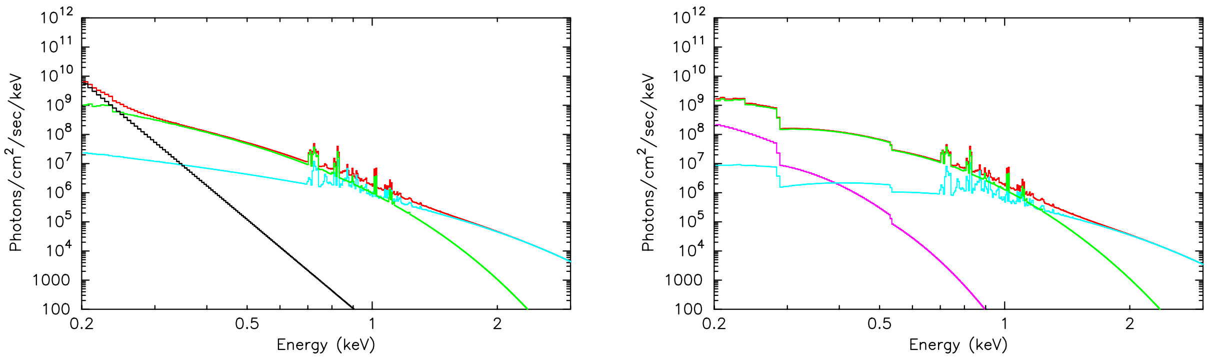

Figure 5.13: The incident best fit model spectra indicated in Fig. 5.11 (2 thermal plasma + 1 power-law – left panel) and Fig. 5.14 (3 thermal plasma when C and O absorption were considered – right). in energy space (red lines). The contributions of each component are indicated by different colors.

in extracting the X-ray signals to the spectrum. The average number and the standard deviation of the detected count per each shot are 10 ± 3 c shot^{-1}, corresponding to ~ 286 c s^{-1}, and fluctuation of the count is also consistent with the Poisson statistics. As a result, 1920 counts in the 273 shots (9.56 s exposure) remain in the energy range of 0.2–3 keV, after 546 pulses are left aside as pile-up or fake events.

When the model including 4-thermal plasma, the same in the first measurement was considered, we had a poor fit (χ^2/d.o.f. = 44.3/32) and there were large residuals between the measured spectra and model in 0.3–0.7 keV band. Then moderately good fits are obtained by including a very steep (> 10) power-law continuum (χ^2/d.o.f. = 35.0/34), as shown in Fig. 5.11. Contrary to the results in the first measurement, line emissions are weaken in the X-ray flux in the 0.7–1.2 keV range, and only the upper limits of the fraction of Carbon and Oxygen can be obtained.

Fig. 5.12 represents the differences of spectral results through various thickness of ice (0, 1 μm of H_2O) on the films of X-ray window. We assume that the thickness of H_2O is smaller than 2 μm from the results of the measurement at TMU. Most of parameters, temperatures of thermal plasma components, photon index and fraction of impurities except for Oxygen do not show significant on the thickness of the contamination on the X-ray window.

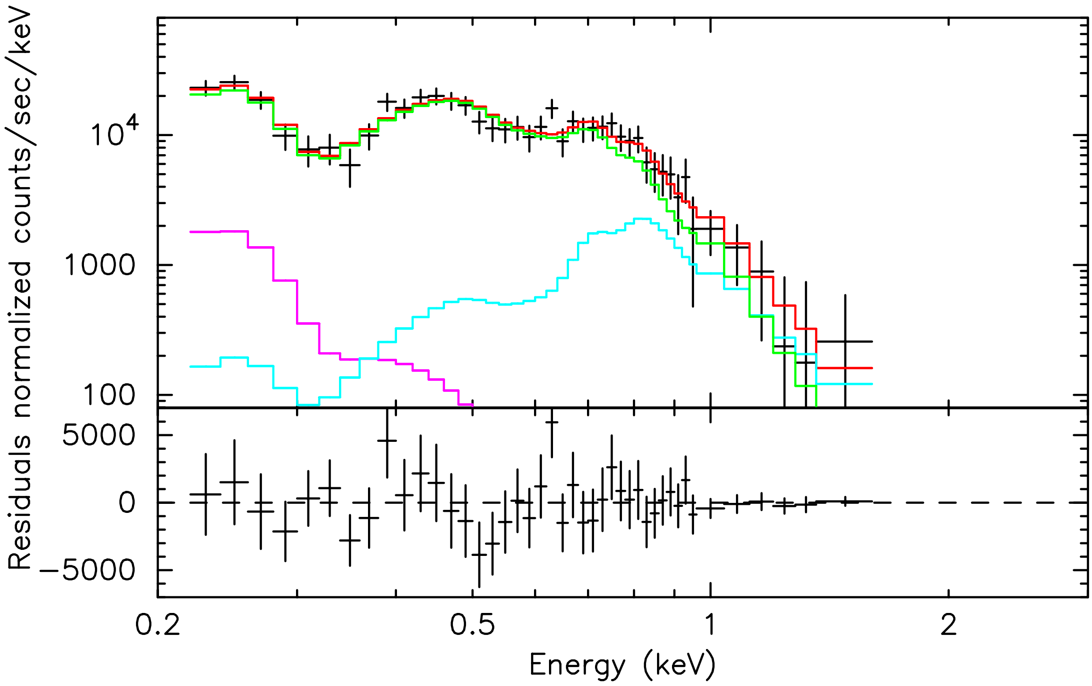

Figure 5.14: 0.2-3.0 keV X-ray spectrum of the TES between 35–70 ms and red lines show the best-fit model spectra by considering 3 thermal plasma after C and O absorption. The contributions of each component are indicated by different colors.

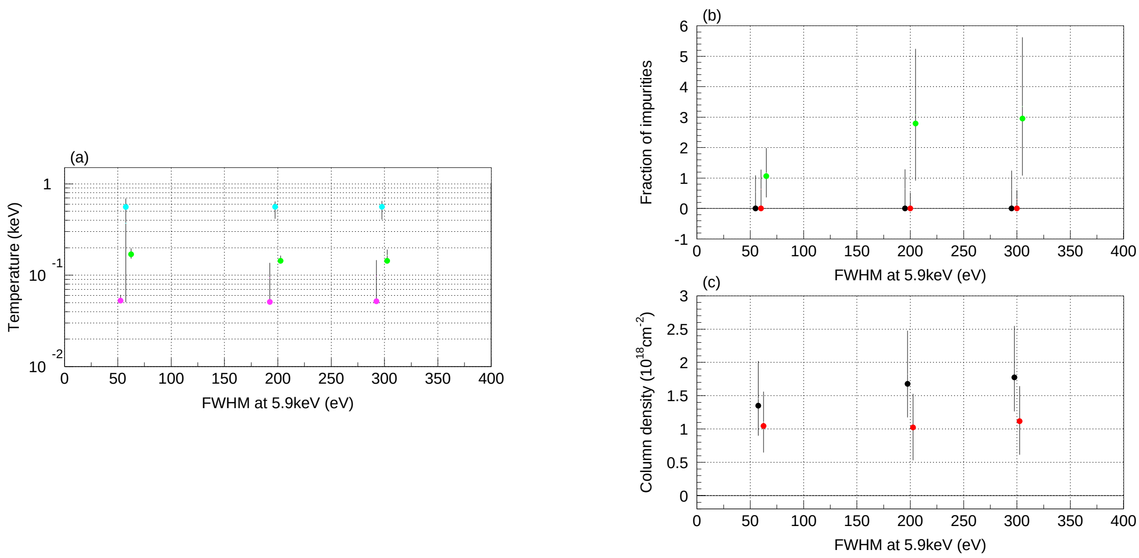

Figure 5.15: Energy resolution dependences of various parameters for spectral fitting by using the same model to Fig.5.14. (a) relation between the resolution at Mn Kα and temperatures of each thermal plasma model component. (b)Top: relation between the resolution and fraction of impurities, Carbon ($\times 10^{-5}$, black), Oxygen ($\times 10^{-6}$, red), Fe ($\times 10^{-6}$, green). Bottom: relation of the column densities of Carbon and Oxygen.

Next, we have introduced photoelectric absorptions with Carbon and Oxygen to 3-thermal plasmas ("vphabs" in XSPEC). Fig. 5.13 shows the comparison of incident best fit model spectra between the models with and without power-law and absorptions. We obtained better results using C-statistic, as shown in Fig. 5.14. The X-ray flux is dominated by the 100–250 eV thermal plasma component (green) while higher temperature of thermal plasma is required in > 1.5 keV band in both models. The dependence of energy resolution on various parameters for spectral analysis by using the model of 3-thermal plasma after C/O absorption are shown in Fig. 5.15. We recognize no clean dependence between the energy resolution and the spectral parameters. We consider that the films of X-ray window were significantly contaminated by Oxygen in H_2O, and there are probably larger thickness of Carbon than 5 layers of parylene-N films installed as X-ray windows in this measurement.

Chapter 6

Discussion

6.1 Detector performance

6.1.1 TES calorimeters

This measurement is the first attempt of TES calorimeter applied to a thermonuclear fusion experiment, which means that we observed the effect of the DC level variation of the TES output with magnetic field, as well as obtained the X-ray spectrum of ground based thermal plasma for the first time. The DC level apparently affected by the poloidal magnetic field during the plasma shot, which causes the variance of operating point and optimal filtering of X-ray signals.

In our analysis, we consider that the DC level fluctuation is mainly caused by induction current which is generated in the circuit consisting of shunnt resistance R_{s}, the TES R_{TES} and the input coil of the SQUID (Eq. 4.1). This circuitry has very small resistance ($< 0.2\ \Omega$) so that it can provide a large input current caused by a little induction voltage. In addition, the TES signal circuitry has to achieve the significantly short responce time, and low frequency ($\sim$ 10–100 Hz) magnetic fluctuation cannot be supressed. Therefore, an efficient magnetic shield around the TES, SQUID, and shunt resistance in the ADR is critical to obtain good performances.

The edge energy of Carbon and Oxygen in the spectrum of the TES are apparently different from the nominal 284.2 eV and 531 eV respectively, when we assume that the variance of operating point is purely caused by the DC level fluctuation. It indicates that the condition of the TES calorimeter (ex. RT curve) has changed by the magnetic field as well as by mechanical vibrations. In addition, degragation of the energy resolution is mainly determined by the power amplitude in $1-10$ kHz region of the noise spectrum, which significantly increased during the plasma shot in comparison with that in quiescence. This effect could be solved by introducing the electromagnetic shield around the ADR. Furthermore, DC level fluctuation will be reduced by optimization of the TES operating point.

6.1.2 ADR system

The ADR system has operated in reasonably good condition at AIST. The temperature control would be thought to suffer from a mechanical vibration or magnetic field. In particular, there was no estimation concerning the influence of a high frequency magnetic variance to cooling materials, which was more sensitive than dilution refrigerators. Nevertheless, the operation system provided good conditions to the TES calorimeter (Sec. 4.2.4). We notice that the poloidal / toroidal magnetic fields generated by TPE-RX are vertical to that of the superconducting magnet and the saltpill in the ADR since we used it in sideway configurations, which was thought to prevent the interference with the magnetic field of the saltpill.

We note that one of the most important issue about the ADR in this plasma measurement was the hold time of liquied He. We had to refill the L-He and pumped it down in every 14 hours, which mostly determined the operation cycle of the measurement and caused inconvenience in obtaining statistically good spectra. Recently we reconstructed the L-He transfer line and succeeded to have the twice longer hold time of liquid He, namely 27 hours in sideway configurations. We will have to install a mechanical cooler or a continuous ADR to attain a constant measurement without recharges in future.

6.2 Implication from the spectral analysis

Regarding the TES calorimeter spectrum, the obtained spectrum is strongly affected by the deep C and O K-edges due to the IR-UV blocking filters. The energy resolution is not as good as the expected performance of ~ 6 eV, and degraded by a factor of eight to ~ 50 eV. Nevertheless we can clearly see emission lines around 0.7–1.2 keV. They are certainly originated in the Fe-L complex at various ionized states, which are typical for the optically-thin thermal plasma emission. The characteristic L-shell X-rays from neutral Fe are known to be $L\alpha = 705.0$ eV, $L_{\beta 1} = 718.5$ eV, etc, but the energies of the detected emission lines are shifted to much higher and wider energy range. This is a clear evidence that Fe ions exist in the deuterium plasma as an impurity, and that they are collisionally interacting with thermal electrons. It is anticipated that high Z impurities enter the plasma due to the sputtering in the plasma-wall interaction. In this sense, the Fe ions are thought to be migrated into the plasma from the SUS316L stainless steel vessel of the torus. The constituent of SUS316L is Fe: 66%, Cr: 17%, and Ni: 14%, hence smaller fraction of Cr and Ni ions should also be constrained in the plasma. It is suggested from the spectral fitting that $\sim 85\%$ of the X-ray flux in the 0.7–1.2 keV range is dominated by the Fe-L line emissions. We can calculate the impurity fraction [Fe/D] in the present plasma, which turned out to be $[\mathrm{Fe/D}] = 1 - 6 \times 10^{-5}$. This value is comparable to the [C/D] or [O/D] fractions measured in the VUV band [17]. As for the impurities of lighter elements such as C and O, we could poorly determine their fractions due to the very low transmission of the X-ray window. This is because energies of the emission lines for ionized species usually come just above the K-edge of the neutral element.

It is also notable that the Fe-L complex is relatively broad with the line width extending up to ~ 1.2 keV. Such a situation is difficult to account for with a single temperature thermal equilibrium plasma. The spectral fit suggests that at least three different temperature components ranging $T = 200$–900 eV are required to explain this structure. The average temperature of these three components (except for the lowest temperature component) is calculated to be 220–330 eV, weighted with the emission measure of each component $\propto \int n_{\mathrm{el}} n_{\mathrm{i}} dV$. This temperature is smaller than the value ~ 600 eV obtained with the ruby laser Thomson scattering method. It is suggested that there is a temperature gradient from the center of the plasma toward the plasma surface, as reported in a similar RFP machine [7]. Here, we have utilized the MEKAL model in XSPEC, which is based on the optically-thin thermal collisional equilibrium plasma emission code [21]. It is known that the value of $n_{\mathrm{el}}\, t$ gives a good measure for the thermal equilibrium [19], and $t \simeq (10^{18}\ \mathrm{m}^{-3})/n_{\mathrm{el}}$ sec is required to establish the ionization equilibrium for abundant ions. This suggests that the plasma in TPE-RX ($n_{\mathrm{el}} t \sim 5 \times 10^{17}\ \mathrm{m}^{-3}\mathrm{s}$) does not fully achieve the equilibrium, hence it is anticipated that the ionization level is lower than that in the same temperature plasma under a collisional equilibrium.

On the other hand, though four lines are detected in the SiLi spectrum, their line

Table 6.1: Calculated emission measure of each thermal component from Tab. 5.1.

Component	EM (cm^{-3})	EM / $\mathrm{EM_{MAX}}$
	$\mathrm{EM_{MAX}} = 2.9 \times 10^{27*}$	
$kT_1 = 52$ eV,	$\mathrm{EM}_1 = 8.48^{+2.1}_{-2.9} \times 10^{28}$	$29.2^{+7.2}_{-10}$
$kT_2 = 157$ eV,	$\mathrm{EM}_2 = 3.04^{+0.60}_{-0.76} \times 10^{27}$	$1.05^{+0.26}_{-0.2}$
$kT_3 = 350$ eV,	$\mathrm{EM}_3 = 4.41^{+10.8}_{-3.12} \times 10^{26}$	$0.15^{+0.38}_{-0.10}$
$kT_4 = 800$ eV,	$\mathrm{EM}_4 = 2.57^{+0.53}_{-0.46} \times 10^{26}$	$0.09^{+0.02}_{-0.02}$

* electron density $n_\mathrm{e} = 2.56 \times 10^{13}$ cm^{-3} is assumed.

center energies are almost consistent within the error with neutral Mo-L (2293 eV), Cr-K (5415 eV), and Fe-K (6404 eV) lines, respectively. The line center energy $\sim$ 7231 eV is slighty different from Ni-K (7478 eV), which could be confused near by lines (ex. Fe Kβ 7058 eV). When the response matrix for the SiLi detector was generated with the energy resolution of 200 eV (FWHM), all these three lines seem to be significantly broadened. The energy resolution of the SiLi detector is probably degraded to 250–300 eV during the plasma operation, too. Their origins are thought to be fluorescent X-rays from the molybdenum limiters and the SUS316L vessel sputtered by high energy electrons which have escaped from the magnetically confined plasma. A high energy tail is also suggested from the spectral fitting, represented by the power-law component (black) in Fig. 5.2 (b). The SiLi spectrum is also useful to constrain hard band continuum in $E \gtrsim 1.5$ keV.

6.3 Soft component

There is low-energy component in the obtained spectrum, which is prominent below the C K-edge (284.2 eV). When thermal synchrotron radiation is considered, the typical critical angular frequency $\omega_c \sim 6.9 \times 10^{11}$ s^{-1}, which corresponds to 4.5×10^{-4} eV, is derived by assuming the magnetic field of the torus center 0.2 T and electron temperature 600 eV. It cannot be measured in soft X-ray band. On the other hand, the emission measure of each thermal component $\int n_\mathrm{e} n_\mathrm{i} dV$ is obtained from the mean distance to the plasma $\sim$3 m, as listed in Tab. 6.1. We also calculated the ratio of the EM to the expected maximum emission measure $\mathrm{EM_{MAX}}$. $\mathrm{EM_{MAX}}$ is estimated to be 2.9×10^{27} cm^{-3} from the observed volume of the TES calorimeter 4.5 cm^3 and maximum electron density 0.4 mTorr $= 2.56\times10^{13}$ cm^{-3}. The ratio of EM / $\mathrm{EM_{MAX}}$ for $kT_1 = 52$ eV soft component is too large for the present plasma. In addition, obtained [C/D] fraction is $> 1 \times 10^{-3}$, which is significantly larger than [O/D]. In TPE-RX, no component made of Carbon is installed in the vacuum vessel so that it's unlikely that the abundance of Carbon exceeds Oxygen. Over all, it suggests that the soft component is caused by reflection or scattering at the surface of the stenless vessel rather than X-ray emission directly from the plasma. Other thermal components (kT=157 eV, 350 eV, 800 eV) are considered to be X-ray emission from the plasma, but these may also include some scattering. We note that there are uncertainties in the detection efficiency in low energy band, in particular concerning the X-ray transmission of the films of X-ray window and low energy flat continuum.

6.4 Fraction of impurity and radiation loss

As shown in Fig. 5.4, $\sim 85\%$ of the X-ray flux in the 0.7–1.2 keV range is dominated by the Fe-L line emissions from the spectral fitting. The Fe fraction [Fe/D] is $1-6\times10^{-5}$, which suggests that less than 1 μg of Fe are migrated into the plasma from the stenless steel vessel in the time duration 35–70 ms per 1 shot. The radiation fraction of the Fe-L(Cr-L, Ni-L) line emissions is 2 % in 0.2–10.0 keV band, while it becomes 16 % when the 52 eV soft component is neglected.

Total radiation loss is estimated to be 3.2 kW, by using Eq. 5.1 with the spectral fitting result, with the 52 eV soft component not included. On the other hand, 0.2–30.0 keV radiation loss is calulated to be 1–5 kW from the best fit model spectra including impurities except for the 52 eV soft component. As a result, we suggest that radiation loss in the time duration of 35–70 ms is < 5 kW. The mean input power $I_{\mathrm{p}}V$ is ~ 2 MW in 35–70 ms, thus the radiation fraction < 0.3 % is derived. We note that the mean input power includes the induction voltage at the outer shell (Cu, Al), not the total input to the deuterium plasma.

6.5 Thermal equipartition time scale and temperature gradient

Basically, Joule heating generated by a plasma current along the toroidal field is used to heat the deuterium gas in TPE-RX, and the energy supply per particle depends on the number of particles. Thus high energy electrons are probably generated in TPE-RX. In addition, when the electron energy provided by the electric field exceeds the thermal energy ($eE\lambda > k_{\mathrm{B}}T$), electrons begin to be accelerated. We infer that such a high energy electron escapes from the confined plasma, sputter the vaccum vessel, and it causes a power-law emission continuum in hard X-ray band.

A condition that plasma with different temperatures can exist in the present experiment is considered. Since the mean free path of thermal electron is assumed to be $\lambda_{\mathrm{e}} \sim 1.4\times10^{5}$ m, it is sufficiently large compared with the typical length scale of temperature gradient ($(\frac{\alpha \ln T}{\alpha r})^{-1} < 0.2$ m) as well as the minor radius (0.45 m) of TPE-RX. Elastic collisions of particles will lead to a relaxation to the Maxwellian distribution. The time scale of this equipartition for electron – electron collision $\tau_{\mathrm{e-e}}$ is

$$\tau_{\mathrm{e-e}} \sim 6.0\times10^{-5}\left(\frac{k_{\mathrm{B}}T_{\mathrm{e}}}{1\ \mathrm{keV}}\right)^{3/2}\left(\frac{n_{\mathrm{i}}}{1.28\times10^{13}\ \mathrm{cm}^{-3}}\right)^{-1}\left(\frac{\ln\Lambda}{20}\right)^{-1}\ \mathrm{sec} \tag{6.1}$$

Electron can achieve this relaxation rapidly. However, kinetic motion of electron is strongly affected by magnetic field, and the Larmor radius r_{L} of 1 keV thermal electron in the center of the minor radius is

$$r_{\mathrm{L}} \sim 5.3\times10^{-2}\left(\frac{T_{\mathrm{e}}}{1\ \mathrm{keV}}\right)^{1/2}\left(\frac{B_{\mathrm{center}}}{0.2\ \mathrm{T}}\right)^{-1}\ \mathrm{cm} \tag{6.2}$$

which is very small compared with the minor radius. Next, the time scale of the equipartition for electron – ion $\tau_{\mathrm{e-i}}$ is

$$\tau_{\mathrm{e-i}} \sim 0.23\left(\frac{k_{\mathrm{B}}T_{\mathrm{e}}}{1\ \mathrm{keV}}\right)^{3/2}\left(\frac{n_{\mathrm{i}}}{1.28\times10^{13}\ \mathrm{cm}^{-3}}\right)^{-1}\left(\frac{\ln\Lambda}{20}\right)^{-1}\ \mathrm{sec} \tag{6.3}$$

Table 6.2: Plasma parameters used in this thesis

	Meaning	Formula	Value
ω_c	critical angular frequency	$\frac{3}{2}\left(\frac{c}{v}\right)\gamma^3\omega_{\rm B}\sin\theta = \frac{3}{2}\left(\frac{\gamma^2 qB\sin\theta}{mc}\right)$	$6.9\times10^{11}\left(\frac{B_{\rm center}}{0.2\ {\rm T}}\right)\left(\frac{T_{\rm e}}{1\ {\rm keV}}\right)^{-1/2}$ str^{-1}
$r_{\rm L}$	Larmor radius	$\frac{\gamma m_{\rm e}v}{eB} = \frac{\gamma m_{\rm e}^{1/2}(3k_{\rm B}T_{\rm e})^{1/2}}{eB}$	$5.33\times10^{-2}\left(\frac{T_{\rm e}}{1\ {\rm keV}}\right)^{1/2}\left(\frac{B_{\rm center}}{0.2\ {\rm T}}\right)^{-1}$ cm
$\tau_{\rm e-e}$	electron–electron relaxation time	$\frac{3m_{\rm e}^{1/2}(k_{\rm B}T_{\rm e})^{3/2}}{4\pi^{1/2}n_{\rm e}e^4\ln\lambda}$	$6\times10^{-5}\left(\frac{T_{\rm e}}{1\ {\rm keV}}\right)^{3/2}\left(\frac{n_{\rm i}}{1.28\times10^{13}\ {\rm cm}^{-3}}\right)^{-1}\left(\frac{\ln\Lambda}{20}\right)^{-1}$ sec
$\tau_{\rm e-i}$	electron–ion relaxation time	$\frac{3m_{\rm e}^{-1/2}m_{\rm i}(k_{\rm B}T_{\rm e})^{3/2}}{4\pi^{1/2}Z^2n_{\rm i}e^4\ln\lambda}$	$0.23\left(\frac{T_{\rm e}}{1\ {\rm keV}}\right)^{3/2}\left(\frac{n_{\rm i}}{1.28\times10^{13}\ {\rm cm}^{-3}}\right)^{-1}\left(\frac{\ln\Lambda}{20}\right)^{-1}$ sec
$\lambda_{\rm e}$	mean free path of electron	$(3k_{\rm B}T_{\rm e}/m_{\rm e})^{1/2}\tau_{\rm e-e}$	$1.4\times10^{5}\left(\frac{T_{\rm e}}{1\ {\rm keV}}\right)^{1/2}\left(\frac{n_{\rm i}}{1.28\times10^{13}\ {\rm cm}^{-3}}\right)^{-1}$ cm
$\tau_{\rm cond}$	conduction time	$\frac{n_{\rm e}k_{\rm B}}{\kappa}\left(\frac{T}{\lvert\Delta T\rvert}\right)^2$	$50\left(\frac{T_{\rm e}}{1\ {\rm keV}}\right)^{-5/2}\left(\frac{n_{\rm i}}{1.28\times10^{13}\ {\rm cm}^{-3}}\right)^{-1}\times\left(\frac{\ln\Lambda}{20}\right)^{-1}\left(\frac{T/\Delta T}{45\ {\rm cm}}\right)^{2}$ sec

Table 6.3: Device parameter and confinement database [37]

Parameter	Meaning	Value	Note
$I_{\rm p}$ max	maximum plasma current	220 kA	
$V_{\rm p}$	plasma volume	6.88 m	
$B_{\rm pa}$	poloidal magnetic field	0.2 T	maximum field at the center
$n_{\rm e}$	electron density	1.28×10^{13} cm^{-3*}	$n_{\rm e}\simeq n_{\rm i}$

* Radial destribution is not assumed.

which is larger than the plasma duration at flat top phase $\sim$ 35 ms. Also the ionization equilibration time scale is even larger ($\gg$ 100 ms). Furthermore, the time scale of heat conduction $\tau_{\rm cond}$ is

$$\tau_{\rm cond}\sim 50\left(\frac{T_{\rm e}}{1\ {\rm keV}}\right)^{-5/2}\left(\frac{n_{\rm i}}{1.28\times10^{13}\ {\rm cm}^{-3}}\right)^{-1}\times\left(\frac{\ln\Lambda}{20}\right)^{-1}\left(\frac{T/\Delta T}{45\ {\rm cm}}\right)^{2}\ {\rm sec} \tag{6.4}$$

It's very larger than $\sim$ 35 ms. Definitely, properties of the thermal plasma described above depend strongly on the electron / ion density. We conclude that it does seem pretty, likely to observe such a temperature gradient. Tab. 6.2 and 6.3 show the typical plasma parameters in this calculations.

Temperature gradient

In our measurement, the ADR was horizontally connected to the section of TPE-RX (Fig. 3.1). We observed X-rays from inner to outer edges through the center of the torus. We further attempted to obtain the radial distribution of electron temperature along the minor radius, by assuming that higher temperature plasma components are in the center. In the past, the electron temperature profile in TPE-RX was assumed to

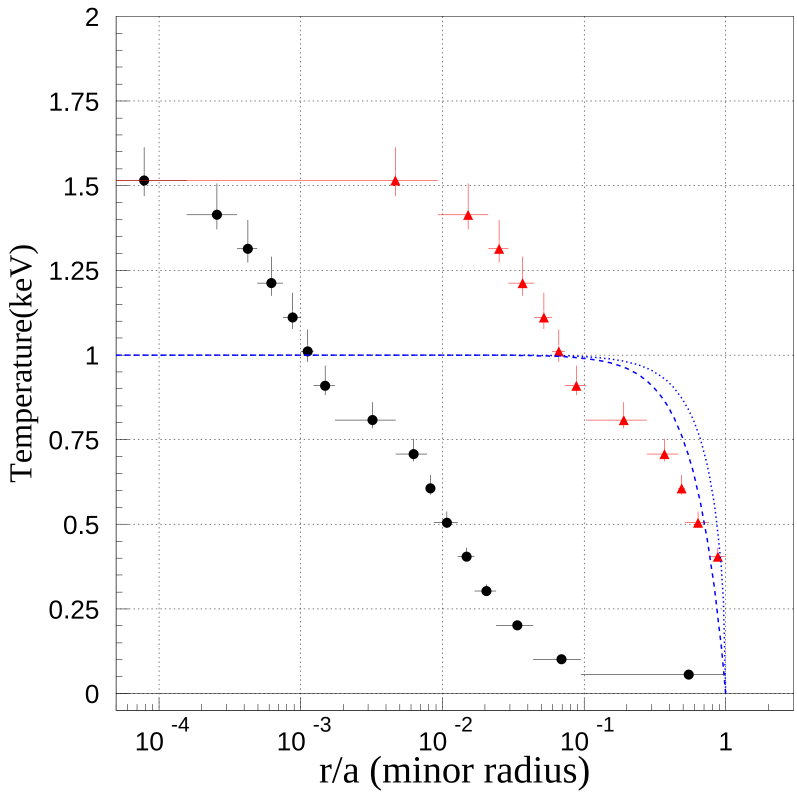

Figure 6.1: Expected radial ditribution obtained by the measured spectrum. Black circles are obtained by including all thermal components, while thermal components except four lowest components are red triangles.

be $T_0(1-(\frac{r}{a})^p)$, and the density profile $n_0(1-(\frac{r}{a})^q)$, where T_0 and n_0 are the electron temperature and the electron density at the center, respectively [2, 35]. These polynomial formula are frequently used to obtain plasma parameters, the poloidal beta β_p and the energy confinement time.

Fig. 6.1 shows the radial distribution of the plasma temperature, normalized to the minor radius. We first examined the spectral fitting obtained at flat top phase in the first measurement (see also Sec. 5.2), in which total 16 thermal plasma models + 1 power-law + 4 gaussian models were fitted. In this fit, 15 out of 16 electron temepratures were linked at even intervals of temperature residual, while 1 thermal model were varied independently. We used the detector response which was the same as in Fig. 5.4. Then, emission measure —$\int n_e n_i dV$ of each model was scaled by assuming $\int n_e n_i dV \propto r$. The polinomial formulae, $T_0(1-(\frac{r}{a})^2)$ (blue dashed lines) and $T_0(1-(\frac{r}{a})^2)^{0.5}$ (blue dotted lines) are overploted for comparison. We note that the radial distribution of the density n_e n_i is flattened in this figure, therefore a larger volume would be involved in outer radius when polinomial destribution to the density is assumed. We also plot the distribution when the four lowest temperature components were omitted. In both distributions, we obtained sharp profiles in comparison with the polunomial formulae described above.

Chapter 7

Conclusion

We summarize our investibation and conclusion below.

1. We have developed the instrumental system of the TES calorimeter including the portable ADR system for ground experiments.

2. We have directly connected the ADR system to TPE-RX with vacuum duct, and succeeded to detect the X-ray signals.

3. The DC level of the TES calorimeter signal output has been fluctuated by the induction current for the plasma current during the plasma generation.

4. The energy resolution of the TES calorimeter has been degraded by a factor of eight of ~ 50 eV. We suggest that there are two reasons, (1) noise increase caused by the induction current, (2) pulse height decreases to 1/2 in comparison with at TMU.

5. In the spectral analysis, the obtained spectrum in lower than 0.6 keV band has been dominated by the scattering or reflection at the surface of the stenless vessel.

6. Fe/D $= 1 - 6 \times 10^{-5}$ has been obtained, which suggests that less than 1 μg migrated into the plasma from the stenless vessel in the time duration 35–70 ms per 1 shot.

7. Total radiation loss has been estimated to be < 5 kW, which corresponds to < 0.3 % of the input power in the time duration 35–70 ms.

8. The thermal equipartition time scale for TPE-RX is longer than the observed time scale, and it is conservative to explain that at least three different temperature components ranging $T = 200$–900 eV are required to the spectral fitting analysis.

we found that the high energy-resolution wide-band X-ray spectroscopy is extremely useful in diagnostics of impurities and physical state of the fusion plasma, although the resolution was limited due to the non-ideal operating point of the TES calorimeter (§ 3.5) and the noise increase during the plasma operation. If the sensor is operated in the optimal operating point, the time constant should be shortened by about a half, which is also effective against the pile-up and the low frequency noise $f \lesssim 5$ kHz dominant in the present noise power spectrum. We have upgraded the magnetic shielding of all the measurement system in March 2005, and the improvement of the noise environment is confirmed. The substrate of the incident X-ray window was also changed into Parylene-N, which has certainly increased low energy X-ray signals.

Appendix A

Log of plasma shots

We listed the parameters of plasma shots. Each parameters are,

- N(TES) : The number ID of the detected waveform for the TES calorimeter.
- time : Time of the detected waveform since 2000-01-01-00:00:00 in unit of second.
- C1 : The detected number of signals in 20-80 ms in full energy band in the plasma shot.
- C2 : The detected number of signals in 35-70 ms in 0.2-4.0 keV band in the plasma shot.
- C3 : The detected number of signals in 35-70 ms in 0.2-4.0 keV band after pile-up or fake event rejections in the plasma shot.
- N(TPE-RX) : The plasma shot number ID of TPE-RX.
- Ip_{MAX} : The maximum plasma current in the plasma shot in unit of kA.
- t_{p} : The time duration of the plasma shot.

Table A.1: Parameters of plasma shot – the first measurement

N (TES)	date	time	C1	C2	C3	N (TPE)	Ip_{MAX} (kA)	t_{p} (ms)
124	2004-08-16T15:30:42	145985442.000	2	2	2	39603	216.13	86.9941
125	2004-08-16T15:44:39	145986279.000	62	37	22	39604	219.67	88.594
126	2004-08-16T15:55:01	145986901.000	46	25	17	39605	221.27	87.9541
127	2004-08-16T16:00:20	145987220.000	33	19	17	39606	222.71	89.234
128	2004-08-16T16:00:20	145987220.000	0	0	0	39607	221.48	88.914
129	2004-08-16T16:10:58	145987858.000	37	22	17	39608	218.59	89.234
130	2004-08-16T16:16:16	145988176.000	32	21	19	39609	219.21	88.914
131	2004-08-16T16:21:33	145988493.000	50	32	15	39610	220.26	89.234
132	2004-08-16T16:26:49	145988809.000	44	28	23	39611	221.08	88.594
133	2004-08-16T16:32:07	145989127.000	42	22	15	39612	220.18	88.594
134	2004-08-16T16:37:24	145989444.000	39	20	18	39613	218.96	89.554
135	2004-08-16T16:48:01	145990081.000	27	16	12	39615	221.11	88.914
136	2004-08-16T16:53:19	145990399.000	30	20	18	39616	219.02	89.234
137	2004-08-16T16:58:36	145990716.000	57	24	21	39617	220.56	89.554
138	2004-08-16T17:03:52	145991032.000	26	13	11	39618	221.64	88.914
139	2004-08-16T17:09:10	145991350.000	29	20	18	39619	223.08	86.6741
140	2004-08-16T17:14:28	145991668.000	33	21	14	39620	220.13	89.554
141	2004-08-16T17:19:45	145991985.000	33	25	15	39621	220	88.2741
142	2004-08-16T17:19:45	145991985.000	0	0	0	39622	219.15	78.0347
143	2004-08-16T17:30:19	145992619.000	36	24	20	39623	221.8	84.7543
144	2004-08-16T17:35:37	145992937.000	39	25	21	39624	220.42	86.6741
145	2004-08-16T17:40:53	145993253.000	29	16	12	39625	220.17	89.234
146	2004-08-16T17:40:53	145993253.000	0	0	0	39626	223.12	87.9541
147	2004-08-16T17:40:53	145993253.000	0	0	0	39627	221.34	88.914
148	2004-08-16T17:56:46	145994206.000	55	33	19	39628	219.57	89.554
149	2004-08-16T18:02:03	145994523.000	43	26	17	39629	218.36	88.914
150	2004-08-16T18:07:21	145994841.000	0	0	0	39630	220.16	89.234
151	2004-08-16T18:12:39	145995159.000	42	22	19	39631	219.84	88.914
152	2004-08-16T18:17:56	145995476.000	114	18	16	39632	220.91	77.7147
153	2004-08-16T18:23:14	145995794.000	44	24	19	39633	222.56	88.594
154	2004-08-16T18:23:14	145995794.000	0	0	0	39634	219.19	87.9541
155	2004-08-16T18:33:50	145996430.000	35	20	18	39635	223.48	88.594
156	2004-08-16T18:39:07	145996747.000	34	23	20	39636	219.82	88.914
157	2004-08-16T18:44:25	145997065.000	36	24	19	39637	220.62	86.3542
158	2004-08-16T18:49:45	145997385.000	30	16	12	39638	219.8	89.554
159	2004-08-16T18:55:02	145997702.000	34	23	20	39639	220.77	89.234
160	2004-08-16T19:00:20	145998020.000	43	21	16	39640	219.4	90.1939

Table A.2: A.1 – continued

N (TES)	date	time	C1	C2	C3	N (TPE)	Ip_{MAX} (kA)	t_{p} (ms)
161	2004-08-16T19:00:20	145998020.000	0	0	0	39641	222.96	88.914
162	2004-08-16T19:10:55	145998655.000	46	23	18	39642	220.98	88.594
163	2004-08-16T19:16:11	145998971.000	30	23	23	39643	221.45	87.9541
164	2004-08-16T19:21:29	145999289.000	138	15	8	39644	218.75	72.275
165	2004-08-16T19:21:29	145999289.000	0	0	0	39645	218.17	89.234
166	2004-08-16T19:21:29	145999289.000	0	0	0	39646	219.43	88.914
167	2004-08-16T19:21:29	145999289.000	0	0	0	39647	220.85	88.914
168	2004-08-16T19:42:38	146000558.000	46	20	13	39648	220.73	87.9541
169	2004-08-16T19:47:56	146000876.000	33	24	21	39649	220.06	88.914
170	2004-08-16T19:53:13	146001193.000	30	18	14	39650	219.63	89.234
171	2004-08-16T19:58:30	146001510.000	51	28	21	39651	220.42	88.594
172	2004-08-16T20:03:46	146001826.000	117	18	17	39652	222.65	78.3547
173	2004-08-16T20:03:46	146001826.000	0	0	0	39653	221.91	87.6341
174	2004-08-16T20:03:46	146001826.000	0	0	0	39654	219.38	89.554
175	2004-08-16T20:19:40	146002780.000	40	21	18	39655	219.29	88.914
176	2004-08-16T20:24:57	146003097.000	110	22	14	39656	220.42	78.0347
177	2004-08-16T20:24:57	146003097.000	0	0	0	39657	220.04	87.6341
178	2004-08-16T20:35:29	146003729.000	38	20	17	39658	220.74	89.234
179	2004-08-16T20:40:46	146004046.000	39	23	17	39659	221.87	90.5139
180	2004-08-16T20:40:46	146004046.000	0	0	0	39660	218.56	86.3542
181	2004-08-17T13:32:42	146064762.000	1	1	1	39661	218.89	88.594
182	2004-08-17T13:43:56	146065436.000	41	25	19	39662	219.76	89.554
183	2004-08-17T13:49:17	146065757.000	40	27	24	39663	220.54	88.594
184	2004-08-17T13:54:34	146066074.000	26	22	18	39664	221.07	88.914
185	2004-08-17T13:59:54	146066394.000	46	30	27	39665	219.43	88.2741
186	2004-08-17T14:05:15	146066715.000	46	27	17	39666	219.43	88.914
187	2004-08-17T14:10:31	146067031.000	44	25	20	39667	220.5	88.2741
188	2004-08-17T14:15:51	146067351.000	28	22	22	39668	222.72	87.9541
189	2004-08-17T14:21:12	146067672.000	78	27	24	39669	221.28	79.6346
190	2004-08-17T14:26:33	146067993.000	35	26	22	39670	219.81	88.914
191	2004-08-17T14:31:52	146068312.000	127	20	13	39671	221.67	78.0347
192	2004-08-17T14:37:09	146068629.000	72	24	17	39672	219.42	80.9145
193	2004-08-17T14:42:29	146068949.000	39	22	17	39673	221.06	88.2741
194	2004-08-17T14:47:47	146069267.000	49	29	20	39674	219.27	89.874
195	2004-08-17T14:53:06	146069586.000	32	22	18	39675	219.66	89.554
196	2004-08-17T14:58:26	146069906.000	34	21	17	39676	221.05	89.554
197	2004-08-17T15:03:44	146070224.000	34	19	15	39677	219.82	88.914
198	2004-08-17T15:09:00	146070540.000	41	28	28	39678	218.44	88.594
199	2004-08-17T15:14:18	146070858.000	99	19	18	39679	219.71	78.9946
200	2004-08-17T15:19:35	146071175.000	30	19	16	39680	219.49	88.914

Table A.3: A.1 – continued

N (TES)	date	time	C1	C2	C3	N (TPE)	Ip_{MAX} (kA)	t_{p} (ms)
201	2004-08-17T15:24:55	146071495.000	33	21	15	39681	219.45	88.914
202	2004-08-17T15:36:54	146072214.000	33	21	19	39682	216.87	89.554
203	2004-08-17T15:42:11	146072531.000	73	27	22	39683	219.83	79.6346
204	2004-08-17T15:47:28	146072848.000	50	26	21	39684	218.24	88.594
205	2004-08-17T15:52:45	146073165.000	38	24	19	39685	219.66	89.874
206	2004-08-17T15:58:02	146073482.000	74	34	27	39686	221.92	80.5945
207	2004-08-17T16:03:23	146073803.000	67	46	23	39687	218.44	88.594
208	2004-08-17T16:08:43	146074123.000	43	24	17	39688	220.57	85.0742
209	2004-08-17T16:14:00	146074440.000	39	23	22	39689	219.77	88.914
210	2004-08-17T16:19:16	146074756.000	39	24	18	39690	219.67	89.554
211	2004-08-17T16:24:34	146075074.000	36	19	19	39691	220.21	88.2741
212	2004-08-17T16:35:49	146075749.000	30	13	13	39692	220.53	84.4343
213	2004-08-17T16:41:11	146076071.000	45	21	20	39693	220.1	87.3141
214	2004-08-17T16:46:27	146076387.000	42	16	15	39694	221.5	87.6341
215	2004-08-17T16:51:43	146076703.000	46	20	13	39695	218.93	88.594
216	2004-08-17T16:57:01	146077021.000	46	29	26	39696	220.96	88.594
217	2004-08-17T17:02:18	146077338.000	125	26	20	39697	222.01	76.7548
218	2004-08-17T17:07:38	146077658.000	163	20	10	39698	220.77	78.3547
219	2004-08-17T17:12:56	146077976.000	128	25	19	39699	219	78.0347
220	2004-08-17T17:18:13	146078293.000	119	12	9	39700	221.43	78.6746
221	2004-08-17T17:23:30	146078610.000	32	21	18	39701	220.41	89.554
222	2004-08-17T17:28:47	146078927.000	42	31	25	39702	220.85	85.7142
223	2004-08-17T17:34:05	146079245.000	66	22	18	39703	218.93	80.2745
224	2004-08-17T17:39:22	146079562.000	46	21	19	39704	220.24	85.0742
225	2004-08-17T17:44:39	146079879.000	33	16	12	39705	221.15	88.2741
226	2004-08-17T17:49:57	146080197.000	45	30	21	39706	219.7	90.1939
227	2004-08-17T17:55:14	146080514.000	43	23	19	39707	219.43	89.554
228	2004-08-17T18:00:31	146080831.000	128	21	18	39708	221.98	75.1549
229	2004-08-17T18:05:48	146081148.000	40	24	15	39709	218.44	88.2741
230	2004-08-17T18:11:06	146081466.000	35	21	17	39710	220.55	88.594
231	2004-08-17T18:16:23	146081783.000	35	18	18	39711	221.05	90.5139
232	2004-08-17T18:21:40	146082100.000	40	24	21	39712	218.94	86.6741
233	2004-08-17T18:26:57	146082417.000	30	21	16	39713	222.34	89.554
234	2004-08-17T18:32:15	146082735.000	32	22	21	39714	219.69	87.9541
235	2004-08-17T18:37:32	146083052.000	119	21	19	39715	221.53	77.3947
236	2004-08-17T18:42:48	146083368.000	36	21	13	39716	219.41	89.874
237	2004-08-17T18:48:06	146083686.000	43	27	22	39717	221.23	89.554
238	2004-08-17T18:53:23	146084003.000	30	21	19	39718	219.5	87.3141
239	2004-08-17T18:58:41	146084321.000	111	33	24	39719	221.29	78.9946
240	2004-08-17T19:03:57	146084637.000	36	14	14	39720	216.5	88.914

Table A.4: A.1 – continued

N (TES)	date	time	C1	C2	C3	N (TPE)	Ip_{MAX} (kA)	t_{p} (ms)
241	2004-08-17T19:14:33	146085273.000	158	14	14	39722	218.08	73.8749
242	2004-08-17T19:19:53	146085593.000	28	17	13	39723	220.76	90.5139
243	2004-08-17T19:25:10	146085910.000	99	19	15	39724	219.29	77.7147
244	2004-08-17T19:30:31	146086231.000	111	21	15	39725	220.02	78.0347
245	2004-08-17T19:35:51	146086551.000	43	27	16	39726	218.48	88.914
246	2004-08-17T19:41:11	146086871.000	76	17	16	39727	220.52	78.9946
247	2004-08-17T19:46:27	146087187.000	33	16	16	39728	218.99	89.554
248	2004-08-17T19:51:48	146087508.000	106	20	16	39729	220.07	77.3947
249	2004-08-17T19:57:09	146087829.000	39	28	18	39730	220	89.234
250	2004-08-17T20:02:25	146088145.000	82	21	17	39731	219.98	79.3146
251	2004-08-17T20:07:42	146088462.000	0	0	0	39732	212.28	60.7557
252	2004-08-17T20:13:02	146088782.000	61	18	17	39733	216.66	79.6346
253	2004-08-17T20:23:38	146089418.000	27	17	12	39735	219.62	89.874
254	2004-08-17T20:28:55	146089735.000	34	23	16	39736	221.36	90.5139
255	2004-08-18T11:33:39	146144019.000	9	9	9	39737	218.94	88.594
256	2004-08-18T11:45:20	146144720.000	50	28	18	39738	219.66	89.234
257	2004-08-18T11:50:37	146145037.000	52	33	17	39739	0	0
258	2004-08-18T11:55:54	146145354.000	43	25	17	39740	221.73	87.6341
259	2004-08-18T12:01:13	146145673.000	37	18	14	39741	222.73	88.914
260	2004-08-18T12:06:32	146145992.000	47	30	20	39742	222.24	87.9541
261	2004-08-18T12:11:49	146146309.000	35	20	18	39743	222.74	88.914
262	2004-08-18T12:17:05	146146625.000	42	26	22	39744	220.72	87.9541
263	2004-08-18T12:27:43	146147263.000	47	30	26	39746	222.45	88.914
264	2004-08-18T12:33:03	146147583.000	41	24	14	39747	221.73	88.2741
265	2004-08-18T12:38:23	146147903.000	144	13	11	39748	222.82	78.9946
266	2004-08-18T12:43:39	146148219.000	52	30	18	39749	222.11	88.594
267	2004-08-18T12:48:59	146148539.000	32	17	9	39750	221.34	88.594
268	2004-08-18T12:54:20	146148860.000	27	19	18	39751	220.94	89.874
269	2004-08-18T12:59:36	146149176.000	39	23	19	39752	220.3	89.554
270	2004-08-18T13:04:52	146149492.000	48	31	21	39753	221.04	89.554
271	2004-08-18T13:10:12	146149812.000	28	19	16	39754	221.07	87.3141
272	2004-08-18T13:15:29	146150129.000	43	24	15	39755	218.75	87.9541
273	2004-08-18T13:20:45	146150445.000	53	25	22	39756	220.56	90.5139
274	2004-08-18T13:26:02	146150762.000	33	17	11	39757	222.9	87.9541
275	2004-08-18T13:31:19	146151079.000	148	22	16	39758	222.1	78.3547
276	2004-08-18T13:36:36	146151396.000	36	21	19	39759	222.61	89.234
277	2004-08-18T13:41:53	146151713.000	31	21	16	39760	222.91	88.914
278	2004-08-18T13:47:11	146152031.000	50	33	21	39761	221.75	87.9541
279	2004-08-18T13:52:27	146152347.000	247	15	15	39762	220.73	74.5149
280	2004-08-18T13:57:44	146152664.000	48	34	26	39763	219.66	87.6341

Table A.5: A.1 – continued

N (TES)	date	time	C1	C2	C3	N (TPE)	Ip_{MAX} (kA)	t_{p} (ms)
281	2004-08-18T14:03:01	146152981.000	39	21	18	39764	224.04	88.594
282	2004-08-18T14:08:17	146153297.000	48	25	18	39765	222.58	86.6741
283	2004-08-18T14:13:34	146153614.000	38	26	17	39766	222.83	87.6341
284	2004-08-18T14:18:51	146153931.000	38	20	17	39767	222.07	88.594
285	2004-08-18T14:24:11	146154251.000	39	25	21	39768	221.89	88.594
286	2004-08-18T14:29:28	146154568.000	39	24	20	39769	224.09	89.234
287	2004-08-18T14:34:44	146154884.000	48	24	13	39770	220.45	89.234
288	2004-08-18T14:40:02	146155202.000	41	25	16	39771	223.14	89.234
289	2004-08-18T14:45:19	146155519.000	40	22	12	39772	223.92	87.9541
290	2004-08-18T14:50:36	146155836.000	45	27	17	39773	222.72	88.594
291	2004-08-18T14:55:52	146156152.000	37	21	16	39774	221.27	88.594
292	2004-08-18T15:01:08	146156468.000	45	28	18	39775	221.45	89.234
293	2004-08-18T15:06:22	146156782.000	36	22	15	39776	221.3	88.914
294	2004-08-18T15:11:39	146157099.000	31	16	13	39777	223.91	89.234
295	2004-08-18T15:16:55	146157415.000	90	24	14	39778	221.98	80.5945
296	2004-08-18T15:22:11	146157731.000	33	17	16	39779	222.34	88.2741
297	2004-08-18T15:27:28	146158048.000	30	18	16	39780	220.58	87.9541
298	2004-08-18T15:32:45	146158365.000	47	23	20	39781	222.84	88.2741
299	2004-08-18T15:38:01	146158681.000	33	19	12	39782	221.28	88.2741
300	2004-08-18T15:43:17	146158997.000	39	24	21	39783	218.58	87.9541
301	2004-08-18T15:48:33	146159313.000	37	25	23	39784	221.86	88.2741
302	2004-08-18T15:53:50	146159630.000	41	19	17	39785	222.24	88.594
303	2004-08-18T15:59:07	146159947.000	33	21	18	39786	224.16	87.9541
304	2004-08-18T16:09:41	146160581.000	81	11	11	39788	221.79	72.275
305	2004-08-18T16:14:57	146160897.000	56	26	18	39789	224.14	89.234
306	2004-08-18T16:20:14	146161214.000	49	27	19	39790	223.04	88.594
307	2004-08-18T16:25:31	146161531.000	37	22	14	39791	222.82	87.9541
308	2004-08-18T16:30:48	146161848.000	43	27	18	39792	222.64	89.554
309	2004-08-18T16:36:05	146162165.000	35	21	19	39793	223.09	88.914
310	2004-08-18T16:41:22	146162482.000	43	30	21	39794	223.54	88.594
311	2004-08-18T16:46:38	146162798.000	36	23	14	39795	222.23	88.594
312	2004-08-18T16:51:55	146163115.000	34	22	18	39796	222.55	87.9541
313	2004-08-18T16:57:11	146163431.000	33	20	15	39797	222.61	88.594
314	2004-08-18T17:02:27	146163747.000	53	33	25	39798	221.77	88.914
315	2004-08-18T17:07:44	146164064.000	36	23	17	39799	222.17	87.9541
316	2004-08-18T17:13:01	146164381.000	156	20	15	39800	224.46	77.7147
317	2004-08-18T17:18:17	146164697.000	54	37	31	39801	223.87	88.594
318	2004-08-18T17:23:34	146165014.000	40	24	17	39802	222.73	88.2741
319	2004-08-18T17:28:52	146165332.000	39	22	21	39803	221.4	88.594
320	2004-08-18T17:34:07	146165647.000	31	14	10	39804	221.67	86.0342

Table A.6: A.1 – continued

N (TES)	date	time	C1	C2	C3	N (TPE)	Ip_{MAX} (kA)	t_{p} (ms)
321	2004-08-18T17:39:23	146165963.000	35	26	22	39805	220.88	88.2741
322	2004-08-18T17:44:40	146166280.000	38	20	12	39806	221.66	88.2741
323	2004-08-18T17:49:56	146166596.000	32	18	16	39807	220.35	88.594
324	2004-08-18T17:55:16	146166916.000	30	23	19	39808	220.86	88.2741
325	2004-08-18T18:00:32	146167232.000	29	20	20	39809	221.05	88.2741
326	2004-08-18T18:05:50	146167550.000	42	29	17	39810	223.38	86.9941
327	2004-08-18T18:11:05	146167865.000	37	20	16	39811	221.86	87.9541
328	2004-08-18T18:16:22	146168182.000	25	15	13	39812	223.08	88.914
329	2004-08-18T18:21:38	146168498.000	40	22	20	39813	221.64	89.234
330	2004-08-18T18:26:55	146168815.000	41	19	13	39814	220.23	88.594
331	2004-08-18T18:32:12	146169132.000	36	22	16	39815	223.52	88.2741
332	2004-08-18T18:37:29	146169449.000	129	19	19	39816	226.03	77.3947
333	2004-08-18T18:42:45	146169765.000	50	30	19	39817	222.36	88.914
334	2004-08-18T18:48:01	146170081.000	46	24	19	39818	223.53	88.914
335	2004-08-18T18:53:18	146170398.000	44	27	20	39819	220.34	88.914
336	2004-08-18T18:58:34	146170714.000	39	22	18	39820	220.48	88.594
337	2004-08-18T19:03:50	146171030.000	24	14	10	39821	220.47	88.2741
338	2004-08-18T19:09:07	146171347.000	46	24	15	39822	221.66	86.6741
339	2004-08-18T19:14:22	146171662.000	37	25	21	39823	221.48	88.594
340	2004-08-18T19:19:40	146171980.000	49	29	23	39824	222.86	88.914
341	2004-08-18T19:24:56	146172296.000	40	25	18	39825	220.43	88.914
342	2004-08-18T19:24:56	146172296.000	0	0	0	39826	219.48	88.2741
343	2004-08-18T19:35:30	146172930.000	45	26	20	39827	221.64	88.2741
344	2004-08-18T19:40:46	146173246.000	51	29	20	39828	220.06	88.594
345	2004-08-18T19:46:02	146173562.000	48	29	22	39829	222.39	88.914
346	2004-08-18T19:51:16	146173876.000	53	29	19	39830	222.77	88.594
347	2004-08-18T19:56:32	146174192.000	99	14	14	39831	223.41	77.3947
348	2004-08-18T20:01:48	146174508.000	47	29	17	39832	221.88	88.2741
349	2004-08-18T20:07:04	146174824.000	32	22	19	39833	220.55	87.6341
350	2004-08-18T20:12:24	146175144.000	31	19	18	39834	222.44	88.594
351	2004-08-18T20:17:44	146175464.000	42	25	14	39835	221.64	88.914
352	2004-08-18T20:23:03	146175783.000	52	25	16	39836	223.23	89.234
353	2004-08-18T20:23:03	146175783.000	0	0	0	39838	221.1	88.914
354	2004-08-18T20:38:53	146176733.000	37	19	15	39839	223.27	88.594

Table A.7: Parameters of plasma shot – the second measurement

N (TES)	date	time	C1	C2	C3	N (TPE)	Ip_{MAX} (kA)	t_{p} (ms)
2001	2005-03-07T16:03:29	163526609.000	2	2	2	41793	219.061	88.5935
2002	2005-03-07T16:17:35	163527455.000	2	2	2	41794	222.217	87.4735
2003	2005-03-07T16:28:23	163528103.000	70	44	19	41795	221.147	87.4735
2004	2005-03-07T16:36:48	163528608.000	38	25	16	41796	219.093	88.7534
2005	2005-03-07T16:42:38	163528958.000	37	20	16	41797	218.741	86.6736
2006	2005-03-07T16:48:27	163529307.000	22	11	11	41798	218.647	87.6335
2007	2005-03-07T16:54:15	163529655.000	32	17	13	41799	219.692	86.0336
2008	2005-03-07T17:00:22	163530022.000	0	0	0	41800	220.595	86.0336
2009	2005-03-07T17:05:51	163530351.000	27	20	18	41801	220.088	86.6736
2010	2005-03-07T17:20:06	163531206.000	30	18	16	41802	218.574	86.8336
2011	2005-03-07T17:25:57	163531557.000	35	20	16	41803	218.3	86.9936
2012	2005-03-07T17:31:42	163531902.000	37	18	14	41804	221.217	87.1535
2013	2005-03-07T17:37:32	163532252.000	37	22	16	41805	219.146	85.7136
2014	2005-03-07T17:43:21	163532601.000	23	15	14	41806	220.21	86.0336
2015	2005-03-07T17:49:10	163532950.000	25	13	13	41807	220.273	85.8736
2016	2005-03-07T17:54:59	163533299.000	20	13	11	41808	219.284	86.9936
2017	2005-03-07T18:00:48	163533648.000	22	12	10	41809	218.115	85.5537
2018	2005-03-07T18:06:37	163533997.000	41	25	11	41810	221.783	87.1535
2019	2005-03-07T18:12:27	163534347.000	29	11	10	41811	218.133	86.8336
2020	2005-03-07T18:18:17	163534697.000	23	13	11	41812	220.088	85.7136
2021	2005-03-07T18:24:07	163535047.000	23	16	13	41813	219.682	85.7136
2022	2005-03-07T18:29:56	163535396.000	24	15	15	41814	219.943	86.3536
2023	2005-03-07T18:35:42	163535742.000	20	15	13	41815	219.845	86.0336
2024	2005-03-07T18:41:31	163536091.000	22	13	13	41816	218.938	86.1936
2025	2005-03-07T18:47:21	163536441.000	26	18	16	41817	219.518	86.1936
2026	2005-03-07T18:53:11	163536791.000	28	17	17	41818	221.294	87.4735
2027	2005-03-07T18:58:59	163537139.000	28	16	12	41819	218.367	87.1535
2028	2005-03-07T19:04:44	163537484.000	22	16	11	41820	217.617	86.8336
2029	2005-03-07T19:16:20	163538180.000	19	14	13	41822	219.58	86.9936
2030	2005-03-07T19:22:10	163538530.000	25	18	15	41823	218.741	87.6335
2031	2005-03-07T19:27:58	163538878.000	25	14	10	41824	217.9	86.1936
2032	2005-03-07T19:33:48	163539228.000	17	11	11	41825	218.439	87.6335
2033	2005-03-07T19:39:36	163539576.000	24	16	13	41826	218.861	83.1538
2034	2005-03-07T19:45:23	163539923.000	24	15	11	41827	218.249	85.0737
2035	2005-03-07T19:51:12	163540272.000	29	19	15	41828	217.605	82.9938
2036	2005-03-07T19:57:01	163540621.000	19	12	12	41829	218.687	86.9936
2037	2005-03-07T20:02:51	163540971.000	20	13	11	41830	218.569	86.0336
2038	2005-03-07T20:08:38	163541318.000	26	16	15	41831	216.714	85.5537
2039	2005-03-07T20:14:27	163541667.000	23	19	15	41832	217.487	86.0336
2040	2005-03-07T20:20:13	163542013.000	24	12	7	41833	217.891	87.9535

Table A.8: A.7 – continued

N (TES)	date	time	C1	C2	C3	N (TPE)	Ip_{MAX} (kA)	t_{p} (ms)
2041	2005-03-07T20:26:02	163542362.000	21	16	14	41834	216.599	84.2737
2042	2005-03-07T20:31:51	163542711.000	21	15	11	41835	221.149	84.5937
2043	2005-03-07T20:37:40	163543060.000	27	19	16	41836	217.93	86.3536
2044	2005-03-07T20:43:25	163543405.000	20	13	12	41837	218.495	86.6736
2045	2005-03-07T20:49:14	163543754.000	34	16	12	41838	219.669	83.7938
2046	2005-03-07T20:55:03	163544103.000	23	13	9	41839	220.232	86.9936
2047	2005-03-07T21:00:51	163544451.000	23	12	12	41840	220.985	79.3141
2048	2005-03-08T15:21:59	163610519.000	2	2	2	41841	221.29	86.0336
2049	2005-03-08T15:34:42	163611282.000	0	0	0	41842	0	0
2050	2005-03-08T15:41:20	163611680.000	20	15	11	41843	222.097	86.1936
2051	2005-03-08T15:47:57	163612077.000	18	9	7	41844	220.565	87.1535
2052	2005-03-08T15:54:36	163612476.000	36	24	11	41845	220.701	86.0336
2053	2005-03-08T16:00:23	163612823.000	22	15	13	41846	219.837	87.4735
2054	2005-03-08T16:06:13	163613173.000	21	13	11	41847	220.851	85.5537
2055	2005-03-08T16:12:02	163613522.000	19	14	11	41848	219.828	86.5136
2056	2005-03-08T16:17:50	163613870.000	30	15	11	41849	220.588	85.5537
2057	2005-03-08T16:23:39	163614219.000	20	15	9	41850	220.748	86.1936
2058	2005-03-08T16:29:27	163614567.000	16	7	5	41851	0	0
2059	2005-03-08T16:35:16	163614916.000	24	15	8	41852	0	0
2060	2005-03-08T16:44:34	163615474.000	16	10	6	41853	221.509	85.3937
2061	2005-03-08T16:50:23	163615823.000	15	10	10	41854	219.059	84.9137
2062	2005-03-08T16:56:11	163616171.000	25	11	10	41855	219.233	82.9938
2063	2005-03-08T17:01:59	163616519.000	18	11	5	41856	219.52	87.6335
2064	2005-03-08T17:07:46	163616866.000	19	14	14	41857	219.711	85.5537
2065	2005-03-08T17:19:23	163617563.000	16	11	7	41859	221.729	86.0336
2066	2005-03-08T17:25:12	163617912.000	100	15	11	41860	221.492	77.8742
2067	2005-03-08T17:31:00	163618260.000	29	17	7	41861	217.596	88.2735
2068	2005-03-08T17:36:49	163618609.000	27	22	13	41862	219.412	86.6736
2069	2005-03-08T17:45:55	163619155.000	24	13	11	41863	220.284	85.7136
2070	2005-03-08T17:55:45	163619745.000	17	12	9	41864	219.957	86.6736
2071	2005-03-08T18:52:18	163623138.000	1	1	1	41865	220.809	84.5937
2072	2005-03-08T19:26:38	163625198.000	0	0	0	41866	221.352	86.0336
2073	2005-03-08T19:33:08	163625588.000	0	0	0	41867	221.547	84.4337
2074	2005-03-08T20:15:00	163628100.000	0	0	0	41868	218.964	85.3937
2075	2005-03-08T20:33:38	163629218.000	1	1	1	41869	224.733	85.0737
2076	2005-03-08T21:09:50	163631390.000	0	0	0	41870	223.793	83.3138
2077	2005-03-09T14:40:31	163694431.000	1102	434	4	41871	2.08783	50.036
2078	2005-03-09T15:02:51	163695771.000	0	0	0	41872	225.473	84.2737
2079	2005-03-09T15:17:56	163696676.000	0	0	0	41873	223.497	82.9938
2080	2005-03-09T15:23:28	163697008.000	0	0	0	41874	222.691	83.3138

Table A.9: A.7 – continued

N (TES)	date	time	C1	C2	C3	N (TPE)	Ip_{MAX} (kA)	t_{p} (ms)
2081	2005-03-09T15:29:05	163697345.000	63	3	3	41875	222.143	72.9145
2082	2005-03-09T15:34:41	163697681.000	0	0	0	41876	220.845	82.5139
2083	2005-03-09T15:40:16	163698016.000	2	2	2	41877	220.791	83.3138
2084	2005-03-09T15:45:52	163698352.000	0	0	0	41878	218.588	81.2339
2085	2005-03-09T16:06:09	163699569.000	0	0	0	41879	223.163	84.2737
2086	2005-03-09T16:12:49	163699969.000	22	15	15	41880	221.546	83.3138
2087	2005-03-09T16:18:26	163700306.000	12	6	4	41881	218.828	81.3939
2088	2005-03-09T16:24:01	163700641.000	71	6	6	41882	222.785	72.7545
2089	2005-03-09T16:29:38	163700978.000	23	14	10	41883	221.859	82.6739
2090	2005-03-09T16:35:15	163701315.000	68	7	7	41884	220.496	74.3544
2091	2005-03-09T16:40:50	163701650.000	21	13	9	41885	220.742	83.1538
2092	2005-03-09T16:46:27	163701987.000	21	14	11	41886	221.374	83.1538
2093	2005-03-09T16:51:59	163702319.000	70	10	10	41887	219.573	72.4345
2094	2005-03-09T16:57:36	163702656.000	54	6	6	41888	221.719	77.2342
2095	2005-03-09T17:03:12	163702992.000	81	15	5	41889	219.822	70.5147
2096	2005-03-09T17:08:49	163703329.000	69	5	5	41890	221.308	73.7144
2097	2005-03-09T17:14:26	163703666.000	17	12	12	41891	221.958	82.3539
2098	2005-03-09T17:20:02	163704002.000	24	14	14	41892	219.859	81.7139
2099	2005-03-09T17:25:36	163704336.000	12	8	8	41893	220.271	82.5139
2100	2005-03-09T17:31:12	163704672.000	0	0	0	41894	219.452	72.1146
2101	2005-03-09T17:36:48	163705008.000	26	16	9	41895	222.815	82.5139
2102	2005-03-09T17:42:24	163705344.000	67	14	14	41896	220.439	75.4743
2103	2005-03-09T17:48:00	163705680.000	75	7	7	41897	218.639	74.5144
2104	2005-03-09T17:53:35	163706015.000	11	8	6	41898	219.95	82.3539
2105	2005-03-09T17:53:35	163706015.000	0	0	0	41899	221.322	82.3539
2106	2005-03-09T18:04:49	163706689.000	19	10	10	41900	218.924	83.3138
2107	2005-03-09T18:10:25	163707025.000	73	16	12	41901	219.574	70.9946
2108	2005-03-09T18:16:03	163707363.000	18	9	9	41902	220.847	83.3138
2109	2005-03-09T18:21:38	163707698.000	16	9	7	41903	219.827	80.754
2110	2005-03-09T18:27:12	163708032.000	21	11	11	41904	220.548	83.4738
2111	2005-03-09T18:32:47	163708367.000	70	20	6	41905	219.1	70.0347
2112	2005-03-09T18:38:22	163708702.000	18	9	8	41906	222.004	82.9938
2113	2005-03-09T18:43:57	163709037.000	68	11	11	41907	222.33	77.5542
2114	2005-03-09T18:49:32	163709372.000	18	14	10	41908	220.436	83.3138
2115	2005-03-09T18:55:05	163709705.000	16	12	12	41909	222.646	81.2339
2116	2005-03-09T19:00:41	163710041.000	21	14	9	41910	219.459	82.5139
2117	2005-03-09T19:06:17	163710377.000	72	11	9	41911	221.537	72.4345
2118	2005-03-09T19:11:51	163710711.000	18	15	13	41912	221.416	83.7938
2119	2005-03-09T19:17:26	163711046.000	82	32	10	41913	220.551	69.2347
2120	2005-03-09T19:23:02	163711382.000	30	22	18	41914	220.111	83.6338

Table A.10: A.7 – continued

N (TES)	date	time	C1	C2	C3	N (TPE)	Ip_{MAX} (kA)	t_{p} (ms)
2121	2005-03-09T19:28:53	163711733.000	18	11	11	41915	218.679	87.4735
2122	2005-03-09T19:34:44	163712084.000	21	16	13	41916	219.763	87.4735
2123	2005-03-09T19:40:19	163712419.000	64	5	5	41917	221.229	72.4345
2124	2005-03-09T19:45:59	163712759.000	25	17	12	41918	221.512	82.9938
2125	2005-03-09T19:51:34	163713094.000	79	14	9	41919	222.954	75.1544
2126	2005-03-09T19:57:07	163713427.000	20	12	12	41920	221.055	82.0339
2127	2005-03-09T20:02:43	163713763.000	19	10	7	41921	221.562	80.914
2128	2005-03-09T20:08:18	163714098.000	16	10	6	41922	222.505	84.2737
2129	2005-03-09T20:13:55	163714435.000	22	13	8	41923	221.878	83.9538
2130	2005-03-09T20:19:30	163714770.000	17	8	8	41924	219.647	83.3138
2131	2005-03-09T20:25:05	163715105.000	16	13	13	41925	223.375	83.9538
2132	2005-03-09T20:30:42	163715442.000	72	23	4	41926	220.574	69.8747
2133	2005-03-09T20:36:18	163715778.000	18	15	10	41927	221.763	84.2737
2134	2005-03-09T20:41:53	163716113.000	16	11	8	41928	221.631	82.9938
2135	2005-03-09T20:47:29	163716449.000	68	6	6	41929	220.635	72.7545
2136	2005-03-09T20:53:04	163716784.000	72	14	12	41930	220.167	74.1944
2137	2005-03-09T20:53:04	163716784.000	0	0	0	41930	220.167	74.1944
2138	2005-03-09T20:53:04	163716784.000	0	0	0	41930	220.167	74.1944
2139	2005-03-09T20:53:04	163716784.000	0	0	0	41930	220.167	74.1944
2140	2005-03-09T20:53:04	163716784.000	0	0	0	41931	220.557	77.3942
2141	2005-03-09T20:53:04	163716784.000	0	0	0	41932	221.81	72.9145
2142	2005-03-09T20:53:04	163716784.000	0	0	0	41933	223.646	70.3547
2143	2005-03-09T20:53:04	163716784.000	0	0	0	41934	223.548	71.3146
2144	2005-03-09T20:53:04	163716784.000	0	0	0	41935	220.094	69.5547
2145	2005-03-09T20:53:04	163716784.000	0	0	0	41936	219.098	83.6338
2146	2005-03-09T20:53:04	163716784.000	0	0	0	41937	218.946	71.9546
2147	2005-03-09T20:53:04	163716784.000	0	0	0	41938	219.084	74.6744
2197	2005-03-11T14:13:13	163865593.000	1	1	1	41988	221.702	83.3138
2198	2005-03-11T14:24:17	163866257.000	0	0	0	41989	222.964	71.4746
2199	2005-03-11T14:39:06	163867146.000	0	0	0	41990	223.158	84.1138
2200	2005-03-11T14:42:36	163867356.000	86	7	6	41991	222.974	73.8744
2201	2005-03-11T14:48:08	163867688.000	91	10	8	41992	222.377	72.9145
2202	2005-03-11T14:53:45	163868025.000	17	11	10	41993	221.553	82.8338
2203	2005-03-11T14:59:21	163868361.000	98	14	14	41994	220.426	73.3945
2204	2005-03-11T15:04:57	163868697.000	18	14	11	41995	220.229	85.5537
2205	2005-03-11T15:10:32	163869032.000	13	8	5	41996	220.806	82.3539
2206	2005-03-11T15:16:08	163869368.000	88	13	13	41997	218.758	74.1944
2207	2005-03-11T15:21:45	163869705.000	20	11	9	41998	220.465	83.4738
2208	2005-03-11T15:27:18	163870038.000	18	11	10	41999	222.085	84.1138
2209	2005-03-11T15:32:51	163870371.000	17	9	9	42000	221.358	84.9137
2210	2005-03-11T15:38:24	163870704.000	17	16	16	42001	219.794	83.7938

Table A.11: A.7 – continued

N (TES)	date	time	C1	C2	C3	N (TPE)	Ip_{MAX} (kA)	t_{p} (ms)
2211	2005-03-11T15:43:56	163871036.000	0	0	0	42002	220.729	69.8747
2212	2005-03-11T15:49:30	163871370.000	92	6	4	42003	221.475	74.3544
2213	2005-03-11T15:55:06	163871706.000	103	14	12	42004	222.056	75.7943
2214	2005-03-11T16:00:40	163872040.000	0	0	0	42005	220.104	72.5945
2215	2005-03-11T16:06:16	163872376.000	0	0	0	42006	217.394	72.4345
2216	2005-03-11T16:11:52	163872712.000	87	16	13	42007	219.158	77.5542
2217	2005-03-11T16:17:28	163873048.000	91	9	9	42008	220.284	74.5144
2218	2005-03-11T16:23:00	163873380.000	90	7	6	42009	221.268	75.3143
2219	2005-03-11T16:28:37	163873717.000	94	13	9	42010	221.896	75.3143
2220	2005-03-11T16:34:13	163874053.000	92	9	9	42011	222.159	75.3143
2221	2005-03-11T16:39:46	163874386.000	95	4	4	42012	219.286	75.1544
2222	2005-03-11T16:45:21	163874721.000	0	0	0	42013	219.088	68.4348
2223	2005-03-11T16:50:58	163875058.000	10	8	8	42014	219.482	80.914
2224	2005-03-11T16:56:30	163875390.000	106	17	13	42015	218.801	76.2743
2225	2005-03-11T17:02:05	163875725.000	20	15	9	42016	220.365	84.1138
2226	2005-03-11T17:07:38	163876058.000	97	11	9	42017	220.556	73.8744
2227	2005-03-11T17:13:14	163876394.000	0	0	0	42018	221.729	66.8349
2228	2005-03-11T17:18:48	163876728.000	15	9	9	42019	219.245	84.5937
2229	2005-03-11T17:24:24	163877064.000	0	0	0	42020	222.418	72.5945
2230	2005-03-11T17:30:01	163877401.000	84	9	9	42021	218.093	74.6744
2231	2005-03-11T17:35:38	163877738.000	0	0	0	42022	217.639	67.4749
2232	2005-03-11T17:41:14	163878074.000	0	0	0	42023	220.6	68.9148
2233	2005-03-11T17:46:50	163878410.000	0	0	0	42024	217.034	66.6749
2234	2005-03-11T17:52:26	163878746.000	0	0	0	42025	219.444	72.2745
2235	2005-03-11T17:58:04	163879084.000	0	0	0	42026	219.041	69.7147
2236	2005-03-11T18:03:40	163879420.000	0	0	0	42027	209.039	50.036
2237	2005-03-11T18:09:15	163879755.000	87	5	5	42028	219.481	76.1143
2238	2005-03-11T18:14:51	163880091.000	15	13	13	42029	218.158	83.4738
2256	2005-03-12T14:04:29	163951469.000	1	1	1	42048	218.664	87.1535
2257	2005-03-12T14:16:10	163952170.000	0	0	0	42049	217.7	86.3536
2258	2005-03-12T14:21:59	163952519.000	20	13	13	42050	219.783	86.8336
2259	2005-03-12T14:27:47	163952867.000	17	10	8	42051	221.308	82.5139
2260	2005-03-12T14:33:35	163953215.000	16	11	8	42052	220.016	86.5136
2261	2005-03-12T14:39:25	163953565.000	18	13	13	42053	221.951	85.2337
2262	2005-03-12T14:45:11	163953911.000	14	12	10	42054	217.832	84.7537
2263	2005-03-12T14:51:01	163954261.000	12	8	8	42055	219.576	83.7938
2264	2005-03-12T14:56:49	163954609.000	15	11	9	42056	220.045	83.4738
2265	2005-03-12T15:02:38	163954958.000	20	13	12	42057	220.406	85.7136
2266	2005-03-12T15:08:27	163955307.000	15	4	4	42058	221.514	84.4337
2267	2005-03-12T15:14:15	163955655.000	118	14	10	42059	222.271	77.8742
2268	2005-03-12T15:20:03	163956003.000	140	13	11	42060	220.622	76.5943
2269	2005-03-12T15:25:51	163956351.000	138	15	12	42061	218.943	76.9142
2270	2005-03-12T15:31:40	163956700.000	10	8	8	42062	218.114	87.7935

Table A.12: A.7 – continued

N (TES)	date	time	C1	C2	C3	N (TPE)	Ip_{MAX} (kA)	t_{p} (ms)
2271	2005-03-12T15:37:30	163957050.000	14	11	10	42063	218.469	84.5937
2272	2005-03-12T15:37:30	163957050.000	0	0	0	42064	219.054	73.0745
2273	2005-03-12T15:49:07	163957747.000	18	10	9	42065	218.42	84.4337
2274	2005-03-12T15:54:55	163958095.000	13	11	7	42066	220.747	87.3135
2275	2005-03-12T16:00:43	163958443.000	111	9	9	42067	219.582	76.1143
2276	2005-03-12T16:06:33	163958793.000	13	7	7	42068	217.438	87.4735
2277	2005-03-12T16:12:22	163959142.000	15	8	4	42069	218.627	85.0737
2278	2005-03-12T16:18:09	163959489.000	123	8	8	42070	218.624	74.6744
2279	2005-03-12T16:23:57	163959837.000	15	8	8	42071	217.924	82.6739
2280	2005-03-12T16:29:46	163960186.000	101	5	5	42072	218.16	77.5542
2281	2005-03-12T16:35:35	163960535.000	22	16	16	42073	217.741	84.5937
2282	2005-03-12T16:35:35	163960535.000	0	0	0	42074	214.162	67.6349
2283	2005-03-12T16:47:12	163961232.000	141	11	10	42075	218.488	76.1143
2284	2005-03-12T16:53:01	163961581.000	13	10	6	42076	217.246	85.7136
2285	2005-03-12T16:58:49	163961929.000	14	10	6	42077	219.789	84.4337
2286	2005-03-12T17:04:38	163962278.000	14	7	6	42078	217.968	84.1138
2287	2005-03-12T17:10:27	163962627.000	133	8	8	42079	218.145	74.3544
2288	2005-03-12T17:16:16	163962976.000	133	5	3	42080	216.457	75.4743
2289	2005-03-12T17:22:05	163963325.000	7	5	5	42081	218.913	85.8736
2290	2005-03-12T17:27:49	163963669.000	19	16	12	42082	219.251	85.7136
2291	2005-03-12T17:33:39	163964019.000	136	9	9	42083	219.412	75.1544
2292	2005-03-12T17:39:24	163964364.000	20	16	14	42084	220.647	85.2337
2293	2005-03-12T17:45:14	163964714.000	18	16	10	42085	217.862	83.9538
2294	2005-03-12T17:51:00	163965060.000	13	9	9	42086	216.191	84.9137
2295	2005-03-12T17:51:00	163965060.000	0	0	0	42087	217.579	72.4345
2296	2005-03-12T17:51:00	163965060.000	0	0	0	42088	210.483	69.0748
2297	2005-03-12T18:08:24	163966104.000	16	13	12	42089	214.233	84.4337
2298	2005-03-12T18:14:13	163966453.000	117	10	10	42090	217.87	76.5943
2299	2005-03-12T18:20:02	163966802.000	14	9	8	42091	215.507	83.1538
2300	2005-03-12T18:25:51	163967151.000	18	12	11	42092	217.514	84.2737
2301	2005-03-12T18:31:40	163967500.000	19	13	13	42093	216.361	82.0339
2302	2005-03-12T18:37:30	163967850.000	20	15	15	42094	220.599	83.9538
2303	2005-03-12T18:43:19	163968199.000	123	6	6	42095	216.943	76.9142
2304	2005-03-12T18:49:04	163968544.000	133	7	7	42096	218.182	73.8744
2305	2005-03-12T18:54:52	163968892.000	24	15	11	42097	217.299	84.7537
2306	2005-03-12T18:54:52	163968892.000	0	0	0	42098	217.184	67.4749
2307	2005-03-12T19:06:28	163969588.000	12	8	8	42099	215.836	85.0737
2308	2005-03-12T19:06:28	163969588.000	0	0	0	42100	216.236	62.3552
2309	2005-03-12T19:18:06	163970286.000	146	9	7	42101	218.319	75.3143
2310	2005-03-12T19:23:55	163970635.000	19	7	6	42102	216.879	85.5537

Table A.13: A.7 – continued

N (TES)	date	time	C1	C2	C3	N (TPE)	Ip_{MAX} (kA)	t_{p} (ms)
2311	2005-03-12T19:29:44	163970984.000	13	11	11	42103	219.568	83.1538
2312	2005-03-12T19:35:31	163971331.000	16	12	9	42104	218.485	87.1535
2313	2005-03-12T19:41:21	163971681.000	10	7	7	42105	216.155	84.1138
2314	2005-03-12T19:47:11	163972031.000	17	11	10	42106	218.128	84.7537
2315	2005-03-12T19:47:11	163972031.000	0	0	0	42107	218.373	71.6346
2316	2005-03-12T19:58:48	163972728.000	93	7	5	42108	214.438	75.7943
2317	2005-03-12T20:04:34	163973074.000	12	10	10	42109	217.386	86.3536
2318	2005-03-12T20:10:22	163973422.000	139	8	7	42110	215.317	76.4343
2319	2005-03-12T20:10:22	163973422.000	0	0	0	42111	211.553	63.4751
2320	2005-03-12T20:21:59	163974119.000	8	7	7	42112	217.746	82.3539
2321	2005-03-12T20:27:48	163974468.000	125	12	9	42113	216.932	74.1944
2322	2005-03-12T20:27:48	163974468.000	0	0	0	42114	209.846	67.7948
2323	2005-03-12T20:39:23	163975163.000	7	4	4	42115	217.62	83.6338
2324	2005-03-12T20:45:11	163975511.000	101	10	10	42116	210.691	75.3143
2325	2005-03-12T20:51:00	163975860.000	6	6	6	42117	218.591	79.634
2326	2005-03-12T20:51:00	163975860.000	0	0	0	42118	213.854	69.2347
2327	2005-03-12T21:02:37	163976557.000	15	9	9	42119	215.658	83.6338
2328	2005-03-14T13:57:40	164123860.000	32	16	15	42120	221.015	86.8336
2329	2005-03-14T14:08:41	164124521.000	22	14	11	42121	219.861	87.1535
2330	2005-03-14T14:14:29	164124869.000	20	13	12	42122	217.746	82.8338
2331	2005-03-14T14:20:18	164125218.000	365	9	7	42123	220.763	75.6343
2332	2005-03-14T14:26:07	164125567.000	18	11	8	42124	216.677	85.8736
2333	2005-03-14T14:31:56	164125916.000	20	16	10	42125	219.326	84.7537
2334	2005-03-14T14:37:46	164126266.000	271	4	3	42126	220.159	76.2743
2335	2005-03-14T14:43:33	164126613.000	11	8	8	42127	220.583	86.3536
2336	2005-03-14T14:49:21	164126961.000	23	14	9	42128	220.363	86.0336
2337	2005-03-14T14:55:09	164127309.000	21	12	10	42129	219.195	86.5136
2338	2005-03-14T15:00:59	164127659.000	18	11	10	42130	218.555	84.1138
2339	2005-03-14T15:06:48	164128008.000	21	14	13	42131	219.365	86.0336
2340	2005-03-14T15:12:37	164128357.000	13	9	7	42132	219.469	86.8336
2341	2005-03-14T15:18:26	164128706.000	256	11	9	42133	219.122	75.9543
2342	2005-03-14T15:18:26	164128706.000	0	0	0	42134	220.589	73.3945
2343	2005-03-14T15:30:00	164129400.000	15	9	8	42135	219.68	82.8338
2344	2005-03-14T15:35:49	164129749.000	164	14	14	42136	218.291	77.8742
2345	2005-03-14T15:41:38	164130098.000	18	12	11	42137	220.425	84.5937
2346	2005-03-14T15:47:26	164130446.000	25	18	13	42138	220.8	85.2337
2347	2005-03-14T15:53:14	164130794.000	22	14	14	42139	219.429	84.5937
2348	2005-03-14T15:59:00	164131140.000	19	15	14	42140	220.075	82.6739
2349	2005-03-14T15:59:00	164131140.000	0	0	0	42141	216.71	74.8344
2350	2005-03-14T16:10:36	164131836.000	14	8	6	42142	219.091	87.7935

Table A.14: A.7 – continued

N (TES)	date	time	C1	C2	C3	N (TPE)	Ip_{MAX} (kA)	t_{p} (ms)
2351	2005-03-14T16:16:22	164132182.000	10	7	7	42143	217.318	86.9936
2352	2005-03-14T16:16:22	164132182.000	0	0	0	42144	215.778	67.6349
2353	2005-03-14T16:27:59	164132879.000	249	15	10	42145	219.248	77.3942
2354	2005-03-14T16:27:59	164132879.000	0	0	0	42146	219.046	74.3544
2355	2005-03-14T16:39:33	164133573.000	93	15	11	42147	219.732	78.3541
2356	2005-03-14T16:45:21	164133921.000	10	6	6	42148	218.861	84.4337
2357	2005-03-14T16:51:09	164134269.000	19	11	9	42149	221.134	88.2735
2358	2005-03-14T16:56:58	164134618.000	13	11	11	42150	219.126	84.4337
2359	2005-03-14T16:56:58	164134618.000	0	0	0	42151	219.47	73.2345
2360	2005-03-14T16:56:58	164134618.000	0	0	0	42152	221.056	74.8344
2361	2005-03-14T17:14:24	164135664.000	22	15	11	42153	220.092	84.7537
2362	2005-03-14T17:20:13	164136013.000	18	11	11	42154	218.316	83.9538
2363	2005-03-14T17:20:13	164136013.000	0	0	0	42155	219.2	71.7946
2364	2005-03-14T17:20:13	164136013.000	0	0	0	42156	218.749	74.1944
2365	2005-03-14T17:20:13	164136013.000	0	0	0	42157	210.928	66.6749
2366	2005-03-14T17:43:29	164137409.000	16	7	6	42158	221.113	83.9538
2367	2005-03-14T17:49:18	164137758.000	385	12	12	42159	219.287	75.6343
2368	2005-03-14T17:55:04	164138104.000	11	4	4	42160	216.723	87.7935
2369	2005-03-14T18:00:53	164138453.000	420	9	7	42161	217.657	76.5943
2370	2005-03-14T18:00:53	164138453.000	0	0	0	42162	217.857	74.6744
2371	2005-03-14T18:12:32	164139152.000	10	6	6	42163	216.202	85.2337
2372	2005-03-14T18:18:21	164139501.000	12	8	8	42164	217.347	85.0737
2373	2005-03-14T18:24:09	164139849.000	15	10	10	42165	219.562	82.3539
2374	2005-03-14T18:24:09	164139849.000	0	0	0	42166	218.767	72.1146
2375	2005-03-14T18:24:09	164139849.000	0	0	0	42167	215.654	67.1549
2376	2005-03-14T18:41:33	164140893.000	7	6	6	42168	219.371	85.0737
2377	2005-03-14T18:41:33	164140893.000	0	0	0	42169	210.092	69.3947
2378	2005-03-14T18:41:33	164140893.000	0	0	0	42170	218.325	74.9944
2379	2005-03-14T18:58:57	164141937.000	24	14	7	42171	217.2	87.3135
2380	2005-03-14T19:04:46	164142286.000	11	8	4	42172	217.004	83.9538
2381	2005-03-14T19:10:35	164142635.000	18	15	15	42173	218.364	82.3539
2382	2005-03-14T19:10:35	164142635.000	0	0	0	42174	213.699	67.4749
2383	2005-03-14T19:22:13	164143333.000	13	7	6	42175	216.798	86.3536
2384	2005-03-14T19:28:01	164143681.000	10	9	7	42176	215.85	82.1939
2385	2005-03-14T19:28:01	164143681.000	0	0	0	42177	217.109	73.7144
2386	2005-03-14T19:39:34	164144374.000	17	11	7	42178	217.306	86.0336
2387	2005-03-14T19:45:23	164144723.000	23	16	14	42179	216.603	87.7935
2388	2005-03-14T19:45:23	164144723.000	0	0	0	42180	211.902	68.2748
2389	2005-03-14T19:56:59	164145419.000	0	0	0	42181	217.219	87.6335
2390	2005-03-14T20:02:46	164145766.000	0	0	0	42182	215.234	67.3149

Table A.15: A.7 – continued

N (TES)	date	time	C1	C2	C3	N (TPE)	Ip_{MAX} (kA)	t_{p} (ms)
2391	2005-03-14T20:08:34	164146114.000	0	0	0	42183	210.469	65.395
2392	2005-03-14T20:14:23	164146463.000	0	0	0	42184	216.211	70.3547
2393	2005-03-14T20:20:11	164146811.000	0	0	0	42185	214.825	67.9548
2394	2005-03-14T20:26:00	164147160.000	0	0	0	42186	214.261	68.2748
2395	2005-03-14T20:31:47	164147507.000	166	12	12	42187	216.842	74.8344
2396	2005-03-14T20:37:36	164147856.000	15	6	6	42188	218.275	84.5937
2397	2005-03-14T20:43:27	164148207.000	10	7	7	42189	217.922	82.5139
2398	2005-03-14T20:43:27	164148207.000	0	0	0	42190	217.212	70.8346
2399	2005-03-14T20:43:27	164148207.000	0	0	0	42191	207.153	67.4749
2400	2005-03-14T20:43:27	164148207.000	0	0	0	42192	220.423	83.6338
2401	2005-03-14T20:43:27	164148207.000	0	0	0	42193	220.574	75.1544

Bibliography

[1] K. A. Arnauld. XSPEC. In G. Jacoby. and J. Barnes, editors, *Astronomical Data Analysis Software and Systems V*, volume 101 of *ASP Conf. SERIES*, page 17, 1996.

[2] A. Canton, Y. Hirano, P. Innocente, H. Koguchi, and R. Lrenzini. Electron density behaviour in the TPE-RX reversed field pinch experiment and comparison with the particle transport model of the RFX experiment. *Rev. Sci. Instrum*, 46:23–38, November 2004.

[3] L. Carraro et al. The ultra-soft x-ray multilayer mirror-based duochromator for the reverse field experiment reversed field pinch experiment. *Rev. Sci. Instrum*, 68:1043+, 1996.

[4] L. Carraro et al. Reconstruction of the radiation emitted by the intrinsic impurities in the RFX reversed field pinch. *Plasma Physics and Controlled Fusion*, 42:731+, 2000.

[5] L. Carraro and M. Valisa. RFX x-ray pulse height analysis system. *Rev. Sci. Instrum*, 61:2801+, 1990.

[6] R. Cen and J. P. Ostriker. Where Are the Baryons? *Astrophys. J.*, 514:1–6, March 1999.

[7] B. E Chapman et al. High confinement plasmas in the Madison Symmetric Torus reversed-field pinch. *Physics of Plasmas*, 9:2061, May 2002.

[8] R. Davé, R. Cen, J. P. Ostriker, G. L. Bryan, L. Hernquist, N. Katz, D. H. Weinberg, M. L. Norman, and B. O'Shea. Baryons in the Warm-Hot Intergalactic Medium. *Astrophys. J.*, 552:473–483, May 2001.

[9] G. Bernstein, S. Labov, D. Landis, N. Madden, I. Millet, E. Silver, P. Richards. Automated temperature regulation system for adiabatic demagnetization refrigerators. *Cryogenics*, 31:99–101, 1991.

[10] A. Hoshino et al. Evaluation of the IR-UV Blocking Filters for ADR with a TES Microcalorimeter. *Nuc. Inst. Meth. A*, 2006. in press.

[11] A. Hoshino et al. Improved PID method of temperature control for adiabatic demagnetization refrigerators. *Nuc. Inst. Meth. A*, 2006. in press.

[12] K.D. Irwin. *Phonon-Mediated Particle Detection Using Superconducting Tungsten Transition-Edge Sensors*. PhD thesis, Stanford Univ., 1995.

[13] K.D. Irwin et al. A self-biasing cryogenic particle detector utilizing electrothermal feedback and a SQUID readout. *IEEE. Trans. Appl. Supercond.*, 5:2690, 1995.

[14] Y. Ishisaki et al. Present performance of a single pixel Ti/Au bilayer TES calorimeter. volume 4851 of *Proc. SPIE*, pages 831–841, 2003.

[15] Y. Ishisaki et al. Development of a microcalorimeter array for the Diffuse Intergalactic Oxygen Surveyor (DIOS) mission . volume 5501 of *Proc. SPIE*, pages 123–134, 2004.

[16] R. L. Kelley, M. D. Audley, K. R. Boyce, S. R. Breon, R. Fujimoto, K. C. Gendreau, S. S. Holt, Y. Ishisaki, D. McCammon, T. Mihara, K. Mitsuda, S. H. Moseley, D. B. Mott, F. S. Porter, C. K. Stahle, and A. E. Szymkowiak. ASTRO-E high-resolution x-ray spectrometer. In *Proc. SPIE, EUV, X-Ray, and Gamma-Ray Instrumentation for Astronomy X, Oswald H. Siegmund; Kathryn A. Flanagan; Eds.*, volume 3765, pages 114–127, October 1999.

[17] H. Koguchi et al. Measurement of Plasma Radiation Fraction and Impurity Line Spectra in the Reversed Field Pinch Device, TPE-RX. *Jpn. J. Appl. Phys.*, 43:1159–1163, 2004.

[18] A. T. Lee, P. L. Richards, S. W. Nam, B. Cabrera, and K. D. Irwin. A superconducting bolometer with strong electrothermal feedback. *J. Appl. Phys. Letter*, 69:1801–1803, 1996.

[19] K. Masai. X-ray emission spectra from ionizing plasmas. *Astrophysics and Space Science*, 98:367–395, January 1984.

[20] D. McCammon et al. A High Spectral Resolution Observation of the Soft X-Ray Diffuse Background with Thermal Detectors. *Astrophys. J.*, 576:188–203, September 2002.

[21] R. Mewe et al. Calculated X-radiation from optically thin plasmas. V. *Astron. Astrophys. Suppl.*, 62:197–254, November 1985.

[22] K. Mitsuda. The soft x-ray spectrometer (SXS) on NeXT. volume 5488 of *Proc. SPIE*, 2004b.

[23] U. Morita et al. Analyses on the operating point dependence of the energy resolution with a Ti/Au TES microcalorimeter. *Nuclear Instruments and Methods in Physics Research A*, 520:277–280, March 2004.

[24] U. Morita et al. Evaluation of 256 Pixel TES Microcalorimeter Arrays with Electrodeposited Bi Absorbers. *Nuc. Inst. Meth. A*, 2006. in press.

[25] S. H. Moseley, J. C. Mather, and D. McCammon. Thermal detectors as x-ray spectrometers. *J. Appl. Phys.*, 56:1257, 1984.

[26] K. Ogawa et al. Experimental and computational studies of reversed-field pinch on TPE-1R(M). In *International Atomic Energy Agency*, volume 1 of *Proc. 9th International Confinement on Plasma Physics and Controlled Nuclear Fusion Research*, pages 575+, 1983.

[27] K. Shinozaki et al. Soft X-ray Measurement of the TPE-RX Reversed Field Pinch Plasma using High Spectral Resolution TES Microcalorimeter. In Takako Kato, editor, *ITC-14 Proceedings*, volume 7 of *JPFR SERIES*, 2005.

[28] K. Shinozaki et al. Demonstration of the Improved PID Method for the Accurate Temperature Control of ADRs. *Nuc. Inst. Meth. A*, 2006. in press.

[29] K. Shinozaki et al. First Application of a TES Microcalorimeter to a Thermonuclear Fusion Plasma Experiment. *Nuc. Inst. Meth. A*, 2006. in press.

[30] D. Steffensrud et al. Efficiency of short heat exchangers for helium vapor cooling. *Review of Scientific Instruments*, 62:214–216, 1991.

[31] A.E. Szymkowiak et al. Signal Processing for Microcalorimeters. *J. Low Temp. Phys.*, 93:281, 1993.

[32] Y. Takei et al. Performance of a bridge-type TES microcalorimeter, excess noise characteristics and dependence of sensitivity on current. *Nuc. Inst. Meth. A*, 523:134–146, May 2004.

[33] M. Tinkham. *Introduction to Superconductivity.* New York through Japan UNI Agency Inc., 1975.

[34] J. K. Ullom et al. Optimization od Transition-Edge calorimeter Performance. *Nuc. Inst. Meth. A*, 2006. in press.

[35] Y. Yagi. First measurement of confinement properties in TPE-RX reversed field pinch. *Nuc. Fusion*, 40:1933–1942, 2000.

[36] Y. Yagi et al. Design concept and confinement prediction of TPE-RX reversed-field pinch device. *Fusion Eng. Des.*, 45:409–419, 1999.

[37] Y. Yagi, Y. Maejima, Y. Hirano, T. Shimada, I. Hirota, S. Sekine, H. Sakakita, and H. Koguchi. Characteristics of global confinement properties in TPE-series reversed-field pinch devices. *Nuc. Fusion*, 43:1787–1800, 2003.

[38] K. Yoshikawa, K. Dolag, Y. Suto, S. Sasaki, N. Y. Yamasaki, T. Ohashi, K. Mitsuda, Y. Tawara, R. Fujimoto, T. Furusho, A. Furuzawa, M. Ishida, Y. Ishisaki, and Y. Takei. Locating the Warm–Hot Intergalactic Medium in the Simulated Local Universe. *Publ. Astron. Soc. Japan*, 56:939–957, December 2004.

[39] K. Yoshikawa, N. Y. Yamasaki, Y. Suto, T. Ohashi, K. Mitsuda, Y. Tawara, and A. Furuzawa. Detectability of the Warm/Hot Intergalactic Medium through Emission Lines of O VII and O VIII. *Publ. Astron. Soc. Japan*, 55:879–890, October 2003.

Acknowledgements

First of all, I am deeply greatful to my boss, Prof. T. Ohashi for his continuous support, leading and hearty encouragement throughout the five years (six years including undergraduate). I would also greatly appreciate Prof. M. Ishida. His lucid guidance on astrophysics and science helped me all of my study as well as this D-thesis. I also greatly appreciate Dr. Y. Ishisaki for his powerful support on data analysis and experiments, in particular the plasma experiments in AIST under the ultimate hard schedule.

I would like to thank Prof. K. Mitsuda (having a plan of the plasma measurement), Dr. N. Y. Yamasaki (technical advice). I also thank members of fusion plasma group in AIST, Y. Yagi, H. Koguchi, Y. Hirano and H. Sakakita for their technical support under hard schedules. Furthermore, I am deeply grateful to Dr. T. Mihara, the designer of the ADR system and technical adviser of experiments.

I am obliged to all of past and present members of Ohashi group in the Tokyo Metropolitan University, in particular, A. Hayakawa, U. Morita and K. Sato for happy research days, and A. Hoshino for experiments as a measurement partner.

Finally, I contribute the thesis to my parents and brothers.